Studies on Hydrogen-Bonded Metal Complexes Containing Heterocyclic Base Ligands:
4(3*H*)-Pteridinone and 2-(2'-Pyridyl)-4(3*H*)-Pyrimidinone Derivatives

Minoru Mitsumi

DOCTOR OF PHILOSOPHY

Department of Functional Molecular Science
School of Mathematical and Physical Science
The Graduate University for Advanced Studies

1996

Contents

General Introduction

The exploration of new solid-state materials which exhibit unique electrical, magnetic, and optical properties is the most important subject in cross-disciplinary area that involves chemists, physicists, and material scientists.

Hydrogen-bond (H-bond) has been extensively studied from the viewpoint of the molecular recognition studies associated with biological activity[1] and the crystal engineering of the solid.[2] Excellent reviews describing the application of H-bond for these researches have appeared.[3] However, there remains unsolved problems particularly related proton and electron (charge) transfer (PET) phenomena in the solid state. In connection with the proton transfer (PT) phenomena, there are investigation associated with the thermochromism. *N*-Salicylideneaniline derivatives have been known to exhibit thermochromism, which is ascribable to a change in π-electron configuration induced by PT.[4] Reetz et al. reported that the H-bonded 4,4'-bipyridinium salt of squaric acid which undergoes a thermally induced reversible single-crystal–single-crystal phase change associated with PT and a concomitant change in color.[5] On the other hand, the phase-transition of the picric acid complexes with some anilines and the quinhydrone charge-transfer (CT) complex are attributable to the PET phenomena. The phase-transition of the picric acid complexes with some anilines had been studied by Hertel et al.,[6] Kofler et al.,[7] Saito and Matsunaga,[8] Bernstein et al.,[9] and Tanaka et al..[10] These phase-transitions are ascribable to the simultaneous CT and PT phenomena. The quinhydrone CT complex which composed of *p*-benzohydroquinone as a donor molecule and *p*-benzoquinone as an acceptor molecule was found to exhibit a new phase-transition associated with electron and proton transfer under hydrostatic pressure by Mitani et al..[11] Nakasuji et al. reported that the phase-transition found for the quinhydrone CT complex under hydrostatic pressure can be assigned to the cooperative PET phenomena from stepwise considerations as shown in Figure 1.[12] Thus, the PET state might be produced by single ET

1
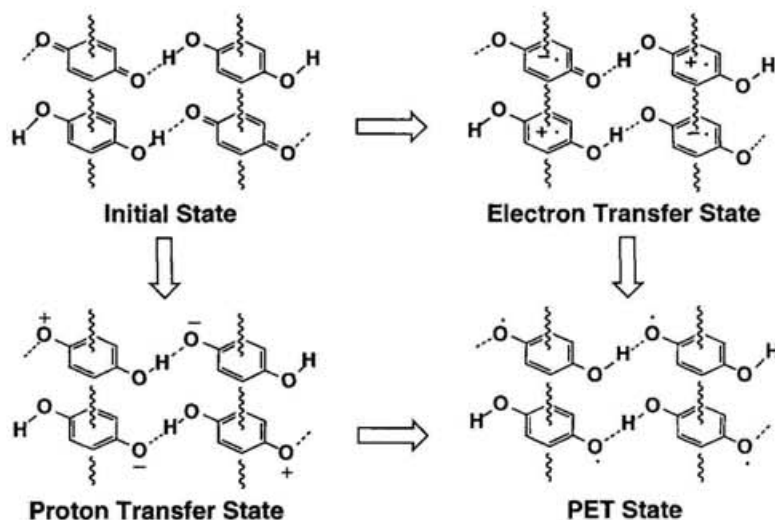
Figure 1. Schematic representation of proton–electron transfer (PET) phenomena in quinhydrone.

associated with single PT, or single PT associated with single ET and can be characterized as a molecular assembly of H-bonded neutral radicals.

The solid-state physical properties expected for the HBCT system is described as follows (Figure 2).[13] If the partial ionic state is realized near the ET state, the molecular metal is obtained, while if the alignment of the neighboring spins which result in a net magnetic moment occurs at the PET state, this leads to bulk magnetic behavior. The highly conductive materials exhibit an intermolecular CT band in the IR region and these absorption band overlaps with the absorption band of D–H stretching vibration which has the most highest energy in the vibrational energy region. In the HBCT system, if the D–H stretching vibration in H-bond couples with the conductive electron, such a system is expected to exhibit characteristic conductive behavior depending on the coupling between the D–H stretching vibration and the conductive electron.[14] Therefore, the HBCT system is expected to exhibit the unique solid-state properties which varies depending upon the kind and strength of proton and electron cooperation because each state is different from the usual electronic state. Furthermore, the HBCT system is expected to show the dynamic solid-state physical properties in response to the external field

2

since the proton and electron cooperation could be controlled by the external field such as heat, light and pressure.
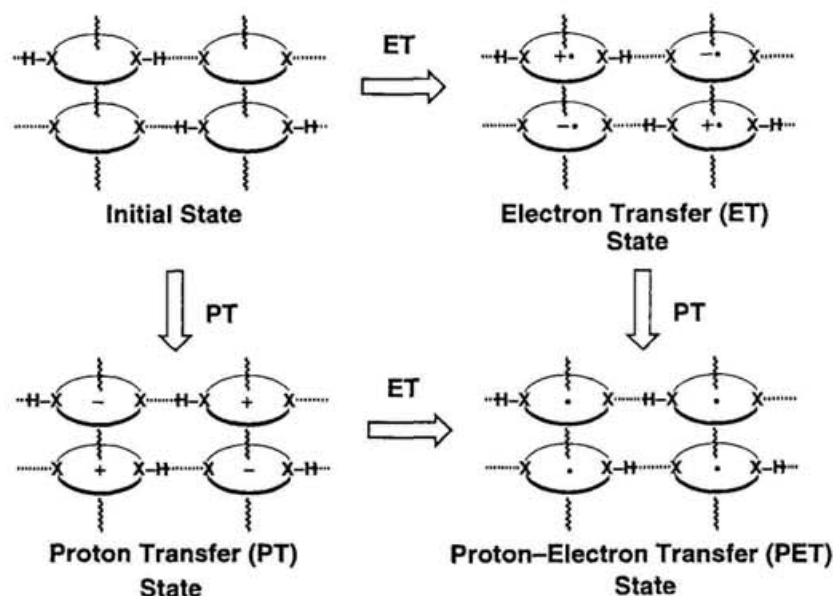
Figure 2. Schematic representation of proton–electron transfer (PET) phenomena.

In principle, CT interaction of organic molecules can be related to the redox properties of the metal atoms and/or stacking interaction between the metal complexes. Therefore, the HBCT system can be extended to a metal complex. The model for the HBCT system utilizing a metal complex is schematically illustrated in Figure 3. This model
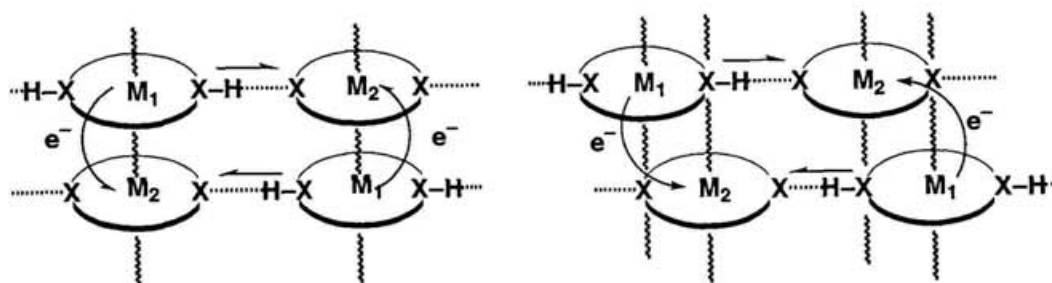

Figure 3. Schematic representation of HBCT system based on metal complex.

3

represents the molecular assembly which contains the intermolecular interaction: in horizontal, H-bonded interaction and in vertical, stacking interaction (π–π, π–d, d–d interactions) capable of intermolecular electron delocalization. The goal of this research is exploration of new molecular assemblies with unique solid state properties originated the PET phenomena. As the basic research for the study of the PET system, it is necessary to construct a new metal complexes having the intermolecular H-bond and CT interaction. Our research efforts have been directed toward the construction of such a metal complex.

There have been computational studies concerned with the effect of excess π-electrons on the proton in the H-bond between π-conjugated molecules. Hasegawa et al. reported that the potential energy curve of the proton in the H-bond changes from asymmetric to symmetric with the increase of excess charges (lack of electron on the proton donor atom and excess on the acceptor atom).[15] On the other hand, Steenken reported from the redox titration studies that the pK_a or pK_b value of the nucleobases drastically changes depending on electron loss or gain.[16] In this study, the heterocyclic bases were selected as the ligand since the effect of π-electrons on the proton in the H-bond is expected. As the basic research for the study of the PET system, the author studied (1) the synthesis and crystallization of H-bonded metal complexes and (2) exploration of new planar mixed-valence dicopper(II,I) complexes.

In Chapter 1, the 4(3H)-pteridinone derivatives, lumazine (HLM) and pterin (HPR), which have the ability to chelate to metal atoms and H-bonding sites of NH···O and NH···N types were chosen for ligand to obtain H-bonded metal complexes. The crystallization of metal–pteridine

HLM   HPR
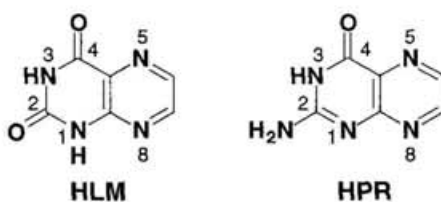
complexes, [Cu(LM)$_2$(H$_2$O)$_2$] (**1**), [Cu(PR)$_2$(H$_2$O)$_2$] (**2**), [Cu(PR)$_2$(H$_2$O)$_2$]·2H$_2$O (**3**), and [Zn(PR)$_2$(H$_2$O)$_2$] ·2H$_2$O (**4**), could be prepared successfully utilizing a diffusion procedure of the deprotonated

ligands and metal source in water. The X-ray crystal structure analyses show that these complexes have the three-dimensional H-bonded networks and the stacking structures between the pteridine skeletons. However, these complexes do not exhibit intramolecular metal–pteridine CT interaction or intermolecular CT interaction. In order to obtain the information on the vibrational states of the proton, the temperature-dependence and pressure-dependence of the IR spectra were measured. However, the temperature dependence and pressure dependence of IR spectra of the complex **1** in the regions of a CO band and a D–H band do not show the spectral change which is attributable to the proton transfer.

In Chapter 2, the author's attention has been given to the intervalence transfer (IT) interaction of the mixed-valence complex in order to introduce the CT interaction into the metal complex. A new family of mixed-valence dicopper(II,I) complexes **1–4** were successfully prepared from a mixture of $Cu(PF_6)_2$ and $[Cu(MeCN)_4]PF_6$ using dinucleating tridentate ligand, HL1–HL4. X-ray crystal structure analyses show that

$[\{Cu(L1)\}_2]PF_6$ (**1**) $[\{Cu(L2)\}_2]PF_6$ (**2**) $[\{Cu(L3)\}_2]PF_6 \cdot DMF$ (**3**) $[\{Cu(L4)\}_2]PF_6 \cdot 0.5MeOH$ (**4**)

HL1[a] R = H

HL2[a] R = Me

HL3[b] R = H

HL4[b] R = Me

[a]known compound
[b]unknown compound
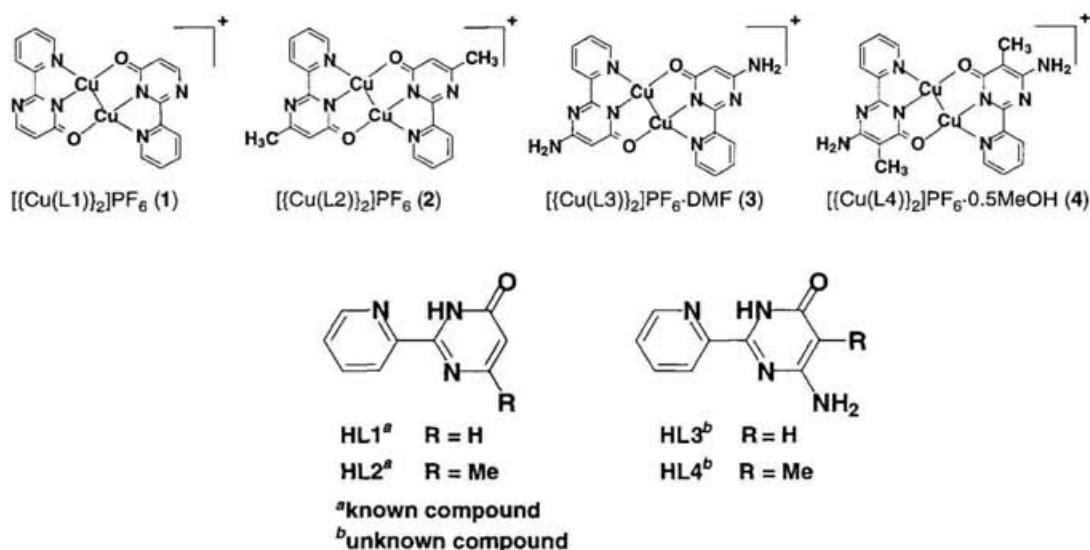
the dicopper complex cations of **1** and **3** are essentially planar structure, while that of **4** is non-planar due to the dimerization. The Cu–Cu distances of these complexes are ca. 2.40 Å, which is short enough to suggest the possibility of some overlap of metal orbitals. The complex cations of **3** are stacked in infinite columns parallel to the *a*-axis and weakly dimerized with the alternated distances of 3.06 and 3.18 Å,

5

respectively. The columns are connected with intermolecular N–H···N H-bonds. The dimer units of **4** form an infinite stack in the direction of the *a*-axis. ZINDO calculations of **1** and **3** indicate that the SOMO's of **1** and **3** are mainly composed of Cu $d_{x^2-y^2}$–Cu $d_{x^2-y^2}$ σ^* combination and the bond orders of Cu–Cu in them are 0.35, which suggests the presence of the copper–copper bond. The complexes **1–4** exhibit a variety of magnetic properties in agreement with that these complexes are mixed-valence dicopper(II,I) complex. Electronic spectra of **1–4** exhibit an absorption in the solid state (in the region 734–754 nm) and in DMF solution (in the region 790–854 nm, ε_{max} ca. 1200–2300 $M^{-1}cm^{-1}$) which are assigned to an IT transition within the Cu_2^{3+} unit. Solution X-Band EPR spectra of complexes **1–4** show seven copper hyperfine lines, consistent with interaction of odd electron both copper centers ($I = 3/2$). In frozen glass, all complexes exhibit axial spectra with four-line copper hyperfine imposed on the $g_\parallel$ signal, which suggests that the unpaired electron is localized in a single copper site. From these results, all complexes are classified into Class II type mixed-valence dicopper(II,I) complex. XPS spectra of all complexes show two Cu $2p_{3/2}$ peaks which are assigned to Cu(I) and Cu(II) oxidation state and the satellite structure characteristic of Cu(II). These results argue that all complexes are mixed-valence dicopper(II,I) complex and do not have delocalized ground state on the XPS time scale (ca. 10^{-17} s).

6

Chapter 1: Metal–Pteridine Complexes Having Three-Dimensional Hydrogen-Bonded Networks

1. 1 Introduction

In order to study basic chemistry of hydrogen-bonded charge-transfer (HBCT) systems, it is necessary to construct the molecular assembly of metal complexes in which a ligand is connected by intermolecular hydrogen-bond (H-bonds). As described in general introduction, the heterocyclic base is suited for the ligand since the effect of π-electron on the proton in the H-bond is expected. The most extensively studied metal–heterocyclic base complexes are metal–nucleobase complexes.[17] Since nuclobases have a number of bonding site and usually coordinated to metal ions monodentately, it is generally difficult to predict that which site will be the binding site for the metal complex. Therefore, the author has utilized the 4(3*H*)-pteridinone derivatives, such as lumazine (HLM) and pterin (HPR), which have the ability to chelate to metal atoms and H-bonding sites of NH···O and NH···N types in the solid state as a basic skeleton of the ligands.

HLM   **HPR**
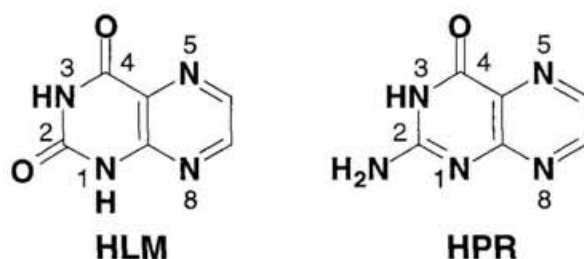
Pteridine–metal complexes have recently been studied to mimic both the metal environment and reactivity of metal sites of enzymes and some of these have been characterized by X-ray crystallography.[18,19] In this chapter, the author describes preparation, crystal structure, and IR spectra of metal-pteridine complexes, $[Cu(LM)_2(H_2O)_2]$ (**1**), $[Cu(PR)_2(H_2O)_2]$ (**2**), $[Cu(PR)_2(H_2O)_2]\cdot 2H_2O$ (**3**), and $[Zn(PR)_2(H_2O)_2]\cdot 2H_2O$ (**4**), which have three-dimensional H-bonded networks and stacking interactions.

1. 2 Experimental Section

1. 2. 1 Measurements

IR spectra were recorded as KBr pellets on a Perkin-Elmer 1600 Series FT-IR spectrophotometer and are reported in wave numbers (cm^{-1}). UV–visible–Near-IR spectra were recorded on a SHIMADZU UV–3100PC UV–vis–NIR scanning spectrophotometer. Elemental analyses (carbon, hydrogen and nitrogen) were obtained from the Chemical Material Center at Institute for Molecular Science. Temperature dependence and pressure dependence of IR spectra were taken on a Nicolet FTIR 800 spectrometer. IR spectra under high pressures were obtained using a gasketed diamond-anvil high pressure cell[20] with an aperture of 0.50 mm . Pressures were monitored by the shift of the ruby R_1 fluorescence line using the linear pressure scale (0.365 Åkbar^{-1}).[21]

1. 2. 2 Materials

Unless noted otherwise, all starting materials were obtained from commercial suppliers and used without further purification. HLM and HPR were synthesized according to literature methods.[23]

1. 2. 3 Preparations.

The desired complexes are expected to have low solubility due to multi-intermolecular H-bonding interactions, which prevent the formation of single crystals by recrystallization procedures. Therefore, in order to prepare single crystals of the complexes **1–4**, we utilized a diffusion procedure of the deprotonated ligands and metal source in water. The synthesis of **1** is typical. Vivid green crystals of **1** were obtained at room temperature by diffusion in an H-shaped tube (ca. 12 mL) containing an aqueous solution of Cu(ClO$_4$)$_2$·6H$_2$O (0.050 mmol, 0.5 mL), an aqueous solution (0.5 mL) of HLM (0.10 mmol) and NaOH (0.11 mmol), and water (11 mL) (yield 28%): IR (KBr, cm^{-1}) 3109 (s), 3061 (m), 3037 (br), 2966 (m), 2909 (m), 2812 (m), 2720 (m), 1654 (s), 1608 (vs), 1569 (vs), 1540 (s), 1510 (s), 1458 (m), 1417(s), 1395(s), 1312(s), 1296 (s), 1233(s), 1210 (m), 1166 (m), 1070 (m) 824 (m); UV/vis [in solid state (KBr

pellet), λ_{max}, nm] 247, 355, 372, 438 (sh), 641 (br). Anal. Calcd for $C_{12}H_{10}CuN_8O_6$: C, 33.85; H, 2.37; N, 26.32. Found: C, 33.45; H, 2.55; N 26.29.

Single crystals of **2–4** were obtained by similar procedures. Diffusion condition for **2** and **3**: an aqueous solution (0.5 mL) of HPR (0.060 mmol) and NaOH (0.066 mmol), an aqueous solution of $Cu(ClO_4)_2 \cdot 6H_2O$ (0.030 mmol, 0.5 mL), and water (11 mL). A few deep yellowish green crystals of **2** and only one deep green crystal of **3** were obtained from the powder deposited in the same batch. The complex **3** has water of crystallization. The data for **2** is as follows: IR (KBr, cm^{-1}) 3406 (s), 3310 (s), 3215 (s), 3116 (w), 1633 (s), 1603 (vs), 1548 (s), 1515 (m), 1466 (s), 1456 (s), 1391 (m), 1361 (s), 1335 (m), 1214 (m), 1171 (m), 1101 (m), 1077 (m), 828 (m); UV/vis [in solid state (KBr pellet), λ_{max}, nm] 265, 311 (sh), 388, 415 (sh), 620 (br).

Diffusion condition for **4**: an aqueous solution (0.5 mL) of HPR (0.075 mmol) and NaOH (0.083 mmol), an aqueous solution of $Zn(NO_3)_2 \cdot 6H_2O$ (0.038 mmol, 0.5 mL), and water (11 mL). Light greenish yellow crystals were obtained (yield 46%): IR (KBr, cm^{-1}) 3432 (s), 3400 (br), 3330 (br), 3297 (br), 3218 (sh), 3145 (s), 1636 (s), 1599 (vs), 1542 (s), 1525 (s), 1463 (s), 1390 (m), 1362 (s), 1332 (m), 1208 (s), 1110 (m), 1078 (m), 830 (m); UV/vis [in solid state (KBr pellet), λ_{max}, nm] 245 (sh), 268, 395, 420 (sh). Anal. Calcd for $C_{12}H_{16}N_{10}O_6Zn$: C, 31.22; H, 3.49; N, 30.34. Found: C, 31.22; H, 3.43; N, 30.87.

1. 2. 4 Crystallographic Studies.

Intensity data were collected at 296 K on Rigaku AFC5R or AFC7R diffractometer with graphite-monochromated Mo Kα radiation and the ω–2θ scan technique. Accurate cell dimensions and crystal orientation matrices were determined by least-squares refinement of 25 (**1**), 18 (**2**), 25 (**3**) and 24 (**4**) reflections in the ranges $22.28 < 2\theta < 29.67^\circ$ (**1**), $20.62 < 2\theta < 36.65^\circ$ (**2**), $22.65 < 2\theta < 24.84^\circ$ (**3**), and $27.65 < 2\theta < 29.86^\circ$ (**4**). The crystallographic data and structure refinement for the complexes **1–4** are summarized in Table 1.

Totals of 4118 (**1**), 2389 (**2**), 2069 (**3**) and 2631 (**4**) reflections were collected to a maximum 2θ value of 60.0° for **1**, **2**, and **4** and of 55.0° for **3**; 2059 (**1**), 2235 (**2**), 1929 (**3**), and 2460 (**4**) of them were unique, and from these,

9

1747 (**1**), 1495 (**2**), 1513 (**3**), and 2089 (**4**) were assumed as observed ($I >$ $3\sigma(I)$). For all four structures the data were corrected for Lorentz, polarization, and absorption effects. No decay correction were applied.

The structures of **1–4** were solved by heavy-atom Patterson methods for **1**[30a] and **4**[30a] and by direct method for **2**[30b] and **3**[30c] expanded using Fourier techniques. All non-hydrogen atoms were refined anisotropically. Hydrogen atoms were located on a ΔF map and refined isotropically. The maximum and minimum peaks on the final difference Fourier map corresponded to 0.36 and –0.28 e Å^{-3} for **1**, 0.33 and –0.32 e Å^{-3} for **2**, 0.25 and –0.26 e Å^{-3} for **3**, and 0.54 and –0.76 e Å^{-3} for **4**, respectively. All calculations were performed using the teXsan[31] crystallographic software package. The fractional atomic coordinates and equivalent isotropic displacement parameters for the complexes **1–4** are listed in Tables 2–5.

Table 1. Crystal Data and Structure Determination

	1	2	3	4
formula	$C_{12}H_{10}CuN_8O_6$	$C_{12}H_{12}CuN_{10}O_4$	$C_{12}H_{16}CuN_{10}O_6$	$C_{12}H_{16}N_{10}O_6Zn$
fw	425.81	423.84	459.86	461.70
color	vivid green	deep yellowish green	deep green	light greenish yellow
form	prismatic	prismatic	prismatic	prismatic
cryst dimens, mm	0.10 x 0.15 x 0.20	0.10 x 0.10 x 0.20	0.20 x 0.20 x 0.05	0.10 x 0.15 x 0.30
a, Å	6.419(1)	7.176(2)	7.812(2)	7.604(1)
b, Å	11.437(3)	13.177(3)	8.598(3)	8.563(2)
c, Å	5.112(1)	8.124(2)	6.863(2)	7.028(2)
α, deg	94.07(2)		108.32(2)	108.69(2)
β, deg	107.07(2)	107.12(2)	95.56(2)	96.22(2)
γ, deg	81.00(2)		74.84(2)	77.02(1)
V, Å^3	354.2(2)	734.2(4)	422.3(2)	422.1(2)
Z	1	2	1	1
crystal system	triclinic	monoclinic	triclinic	triclinic
space group	$P\bar{1}$	$P2_1/n$	$P\bar{1}$	$P\bar{1}$
ρ_{calc}, g cm^{-1}	1.996	1.917	1.808	1.816
ρ_{obs}, g cm^{-1}	1.967			1.845
diffractomrter	Rigaku AFC5R	Rigaku AFC7R	Rigaku AFC5R	Rigaku AFC5R
radiation (λ, Å)	0.71069 (graphite monochromated)	0.71069 (graphite monochromated)	0.71069 (graphite monochromated)	0.71069 (graphite monochromated)
temp, K	296	296	296	296
scan technique	ω–2θ	ω–2θ	ω–2θ	ω–2θ
2θ_{max}, deg	60.0	60.0	55.0	60.0
scan width, deg	0.94 + 0.50 tan θ	1.78 + 0.35 tan θ	0.89 + 0.30 tan θ	1.37 + 0.50 tan θ
range of hkl	$-4 \le h \le 9$ $-15 \le k \le 16$ $-7 \le l \le 6$	$0 \le h \le 10$ $0 \le k \le 18$ $-11 \le l \le 10$	$0 \le h \le 9$ $-10 \le k \le 11$ $-8 \le l \le 8$	$0 \le h \le 10$ $-11 \le k \le 12$ $-9 \le l \le 9$
$F(000)$	215.00	430.00	235.00	236.00
μ(Mo Kα), cm^{-1}	16.01	15.40	13.54	15.16
no. of reflcns collcd	4118	2389	2069	2631
no. of unique data	2059	2235	1929	2460
no. of obsd reflcns	1747 ($I > 3\sigma(I)$)	1495 ($I > 3\sigma(I)$)	1513 ($I > 3\sigma(I)$)	2089 ($I > 3\sigma(I)$)
no. of variables	144	149	165	165
Rav/no. of variables	12.13	10.03	9.17	12.66
R^a	0.030	0.032	0.031	0.038
$R_w{}^b$	0.034	0.038	0.023	0.054
S, goodness of fit^c	1.44	1.32	1.58	2.02
final max/min $\Delta\rho$, e Å^{-3}	0.36/-0.28	0.33/-0.32	0.25/-0.26	0.54/-0.76

[a] $R = \Sigma ||F_o| - |F_c||/\Sigma|F_o|$. [b] $R_w = \{(\Sigma w(|F_o| - |F_c|)^2/\Sigma w|F_o|^2)\}^{1/2}$. [c] $S = \{\Sigma w(|F_o| - |F_c|)^2/(N_o - N_v)\}^{1/2}$, with $w = 4F_o^2/\sigma^2(F_o^2)$.

11

Table 2. Fractional Atomic Coordinates and Equivalent Isotropic Displacement Parameters (Å) for $[Cu(LM)_2(H_2O)_2]$ (**1**)

atom	x	y	z	$B_{eq},^a$ Å^2
Cu(1)	0	0	0	1.471(7)
O(2)	0.5810(3)	0.3762(1)	−0.2084(4)	2.59(4)
O(3)	−0.2418(3)	0.0599(2)	−0.3207(4)	2.31(4)
O(4)	0.2540(3)	0.0518(1)	−0.2001(3)	1.90(3)
N(1)	0.3379(3)	0.3872(2)	0.0389(4)	2.00(4)
N(3)	0.4249(3)	0.2106(1)	−0.2079(4)	1.79(4)
N(5)	0.0223(3)	0.1690(1)	0.1386(3)	1.53(3)
N(8)	0.0824(3)	0.4045(2)	0.2885(4)	2.05(4)
C(2)	0.4534(4)	0.3260(2)	−0.1314(4)	1.84(4)
C(4)	0.2851(3)	0.1559(2)	−0.1271(4)	1.57(4)
C(6)	−0.0857(4)	0.2327(2)	0.2985(4)	1.78(4)
C(7)	−0.0545(4)	0.3501(2)	0.3702(5)	2.05(4)
C(9)	0.1923(3)	0.3386(2)	0.1301(4)	1.65(4)
C(10)	0.1624(3)	0.2220(2)	0.0530(4)	1.50(4)
H(1)	0.358(5)	0.462(3)	0.102(6)	4.2(7)
H(6)	−0.178(4)	0.201(2)	0.361(5)	1.9(5)
H(7)	−0.135(4)	0.388(2)	0.471(5)	2.9(6)
H(31)	−0.336(5)	0.094(3)	−0.310(6)	2.9(7)
H(32)	−0.265(4)	0.025(2)	−0.448(6)	2.2(6)

$^a B_{eq} = (8/3\pi^2)(U_{11}(aa^*)^2 + U_{22}(bb^*)^2 + U_{33}(cc^*)^2 + 2U_{12}aa^*bb^*\cos\gamma + 2U_{13}aa^*cc^*\cos\beta + 2U_{23}bb^*cc^*\cos\alpha)$

Table 3. Fractional Atomic Coordinates and Equivalent Isotropic Displacement Parameters (Å) for $[Cu(PR)_2(H_2O)_2]$ (**2**)

atom	x	y	z	$B_{eq},^a$ Å^2
Cu(1)	0	0	0	1.909(8)
O(1)	0.3061(4)	0.0802(2)	−0.0532(3)	3.11(5)
O(4)	0.1418(3)	−0.1147(1)	0.1406(2)	2.03(3)
N(1)	0.3422(3)	−0.0210(1)	0.6412(2)	1.72(4)
N(2)	0.4856(4)	−0.1764(2)	0.7022(3)	2.27(5)
N(3)	0.3111(3)	−0.1509(2)	0.4205(2)	1.71(4)
N(5)	0.0623(3)	0.0738(1)	0.2214(2)	1.55(4)
N(8)	0.1931(3)	0.1371(2)	0.5656(3)	1.92(4)
C(2)	0.3761(3)	−0.1127(2)	0.5846(3)	1.57(4)
C(4)	0.2101(3)	−0.0886(2)	0.3005(3)	1.51(4)
C(6)	0.0233(4)	0.1662(2)	0.2657(3)	1.84(5)

C(7)	0.0911(4)	0.1961(2)	0.4392(3)	2.01(5)
C(9)	0.2359(3)	0.0427(2)	0.5192(3)	1.44(4)
C(10)	0.1688(3)	0.0129(2)	0.3469(3)	1.37(4)
H(6)	−0.045(4)	0.209(2)	0.185(4)	2.3(6)
H(7)	0.072(4)	0.264(2)	0.469(4)	2.4(6)
H(11)	0.259(7)	0.125(4)	−0.135(6)	8(1)
H(12)	0.334(6)	0.033(3)	−0.091(6)	5(1)
H(21)	0.516(4)	−0.233(2)	0.674(4)	2.0(6)
H(22)	0.535(5)	−0.156(3)	0.798(4)	3.2(7)

$^a B_{eq} = (8/3\pi^2)(U_{11}(aa^*)^2 + U_{22}(bb^*)^2 + U_{33}(cc^*)^2 + 2U_{12}aa^*bb^*\cos\gamma + 2U_{13}aa^*cc^*\cos\beta + 2U_{23}bb^*cc^*\cos\alpha)$

Table 4. Fractional Atomic Coordinates and Equivalent Isotropic Displacement Parameters (Å) for $[Cu(PR)_2(H_2O)_2]\cdot2H_2O$ (**3**)

| atom	x	y	z	$B_{eq},^a$ Å^2
Cu(1)	0	0	0	2.03(1)
O(1)	0.1956(4)	0.1535(3)	0.2299(4)	3.23(6)
O(3)	0.5512(3)	−0.0314(3)	0.2328(4)	3.41(6)
O(4)	−0.1944(2)	0.1426(2)	0.1881(3)	2.17(4)
N(1)	−0.3391(3)	0.6102(3)	0.1041(3)	1.92(5)
N(2)	−0.5019(4)	0.6937(3)	0.3963(4)	2.61(6)
N(3)	−0.3555(3)	0.4159(3)	0.2931(3)	1.88(5)
N(5)	−0.0645(3)	0.1884(3)	−0.1316(3)	1.82(5)
N(8)	−0.1680(3)	0.5080(3)	−0.1935(3)	2.04(5)
C(2)	−0.3943(3)	0.5705(3)	0.2579(4)	1.79(6)
C(4)	−0.2453(3)	0.2902(3)	0.1645(4)	1.73(6)
C(4a)	−0.1781(3)	0.3196(3)	−0.0054(4)	1.59(5)
C(6)	−0.0083(4)	0.2153(3)	−0.2907(4)	2.08(6)
C(7)	−0.0624(4)	0.3751(4)	−0.3193(4)	2.19(6)
C(8a)	−0.2303(3)	0.4807(3)	−0.0313(4)	1.72(5)
H(6)	0.063(4)	0.126(3)	−0.385(4)	2.9(7)
H(7)	−0.024(4)	0.393(3)	−0.431(4)	2.9(7)
H(11)	0.195(5)	0.234(5)	0.208(6)	6(1)
H(12)	0.285(5)	0.098(5)	0.230(6)	5(1)
H(21)	−0.526(4)	0.674(4)	0.490(4)	2.5(8)
H(22)	−0.505(4)	0.801(4)	0.407(5)	4.3(8)
H(31)	0.599(5)	−0.125(4)	0.181(5)	5(1)
H(32)	0.616(4)	0.016(4)	0.213(5)	3.3(9)

$^a B_{eq} = (8/3\pi^2)(U_{11}(aa^*)^2 + U_{22}(bb^*)^2 + U_{33}(cc^*)^2 + 2U_{12}aa^*bb^*\cos\gamma + 2U_{13}aa^*cc^*\cos\beta + 2U_{23}bb^*cc^*\cos\alpha)$

Table 5. Fractional Atomic Coordinates and Equivalent Isotropic Displacement Parameters (Å) for [Zn(PR)$_2$(H$_2$O)$_2$]·2H$_2$O (**4**)

atom	x	y	z	B_{eq},^{a} Å^2
Zn(1)	0	0	0	1.68(1)
O(1)	0.1898(3)	0.1404(3)	0.1955(4)	2.63(5)
O(3)	0.4597(3)	0.0277(3)	−0.2335(4)	2.79(5)
O(4)	−0.2028(3)	0.1500(2)	0.1879(3)	1.95(4)
N(1)	−0.3416(3)	0.6174(3)	0.1140(4)	1.69(4)
N(2)	−0.4933(4)	0.6961(3)	0.4069(4)	2.38(5)
N(3)	−0.3552(3)	0.4210(3)	0.2955(4)	1.72(4)
N(5)	−0.0815(3)	0.2016(3)	−0.1333(4)	1.62(4)
N(8)	−0.1811(3)	0.5234(3)	−0.1807(4)	1.84(5)
C(2)	−0.3934(4)	0.5760(3)	0.2670(4)	1.63(5)
C(4)	−0.2510(4)	0.2964(3)	0.1668(4)	1.50(5)
C(6)	−0.0290(4)	0.2323(4)	−0.2912(4)	1.91(5)
C(7)	−0.0826(4)	0.3943(4)	−0.3110(4)	1.96(6)
C(9)	−0.2397(4)	0.4912(3)	−0.0219(4)	1.44(5)
C(10)	−0.1883(3)	0.3281(3)	−0.0045(4)	1.42(5)
H(6)	0.050(5)	0.147(4)	−0.385(5)	2.1(7)
H(7)	−0.047(5)	0.410(5)	−0.437(6)	3.3(8)
H(11)	0.197(6)	0.234(5)	0.191(6)	3.5(9)
H(12)	0.305(6)	0.082(6)	0.229(7)	4(1)
H(21)	−0.524(6)	0.667(5)	0.501(7)	4(1)
H(22)	−0.515(5)	0.800(5)	0.410(6)	3.3(9)
H(31)	0.390(6)	−0.028(6)	−0.226(7)	4(1)
H(32)	0.431(6)	0.120(6)	−0.178(7)	4(1)

^{a} $B_{eq} = (8/3\pi^2)(U_{11}(aa^*)^2 + U_{22}(bb^*)^2 + U_{33}(cc^*)^2 + 2U_{12}aa^*bb^*\cos\gamma + 2U_{13}aa^*cc^*\cos\beta + 2U_{23}bb^*cc^*\cos\alpha)$

14

1. 3 Results and Discussion

1. 3. 1 Molecular Structures.

The molecular structures of **1**–**4** are shown in Figure 1–4.   These complexes possess an inversion center. Bond distances and angles for **1**–**4** are given in Tables 6–9.

In the complex **1**, the copper(II) ion exhibits an elongated octahedral coordination (Figure 1).   The basal plane consists of two N(5) atoms of LM ligands and two water molecules, and the two axial sites are occupied by two O(4) atoms of LM.
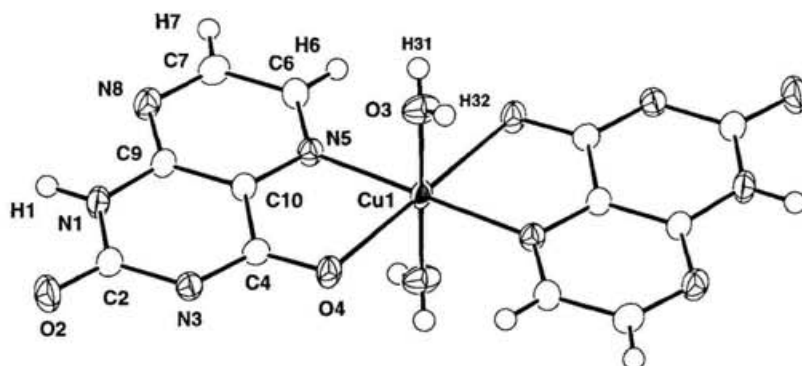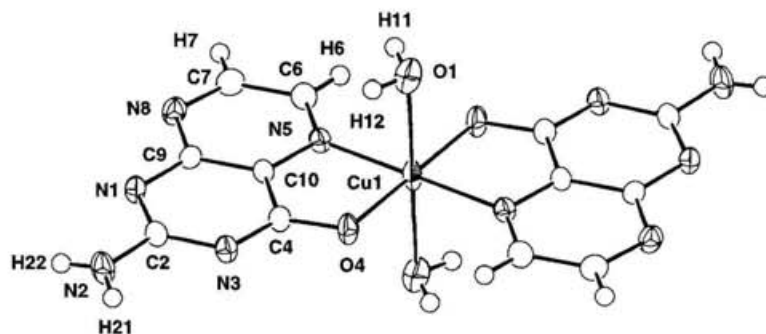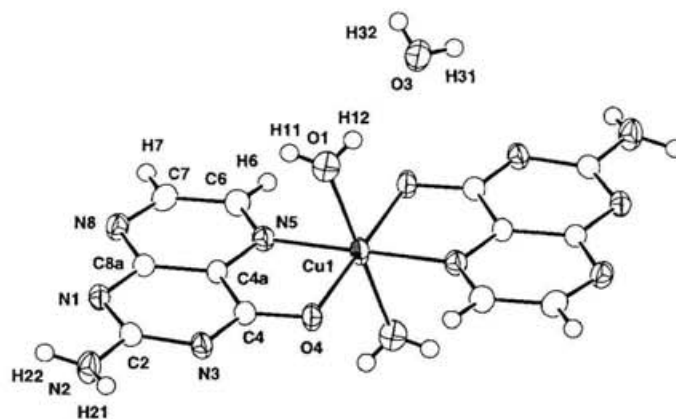

Figure 1. ORETP diagram of **1**, showing the labeling scheme and 50 % thermal ellipsoids.

Table 6. Bond Lengths (Å) and Angles (deg) for [Cu(LM)$_2$(H$_2$O)$_2$] (**1**)

	Distances		
Cu(1)–O(3)	1.975(2)	N(3)–C(4)	1.341(3)
Cu(1)–O(4)	2.329(2)	N(5)–C(6)	1.330(3)
Cu(1)–N(5)	2.022(2)	N(5)–C(10)	1.344(3)
O(2)–C(2)	1.235(3)	N(8)–C(7)	1.326(3)
O(4)–C(4)	1.250(2)	N(8)–C(9)	1.343(3)
N(1)–C(2)	1.388(3)	C(4)–C(10)	1.477(3)
N(1)–C(9)	1.362(3)	C(6)–C(7)	1.396(3)
N(3)–C(2)	1.375(3)	C(9)–C(10)	1.390(3)
O(3)–H(31)	0.68(3)	C(6)–H(6)	0.88(2)
O(3)–H(32)	0.73(3)	C(7)–H(7)	0.88(3)
N(1)–H(1)	0.90(3)		
	Angles		
O(3)–Cu(1)–O(3')	180.0	C(7)–N(8)–C(9)	115.4(2)
O(3)–Cu(1)–O(4)	89.74(7)	O(2)–C(2)–N(1)	119.2(2)
O(3)–Cu(1)–O(4')	90.26(7)	O(2)–C(2)–N(3)	121.5(2)
O(3)–Cu(1)–N(5)	89.00(7)	N(1)–C(2)–N(3)	119.3(2)

15

O(3)–Cu(1)–N(5')	91.00(7)	O(4)–C(4)–N(3)	122.5(2)
O(4)–Cu(1)–O(4')	180.0	O(4)–C(4)–C(10)	119.1(2)
O(4)–Cu(1)–N(5)	78.05(6)	N(3)–C(4)–C(10)	118.5(2)
O(4)–Cu(1)–N(5')	101.95(6)	N(5)–C(6)–C(7)	120.6(2)
N(5)–Cu(1)–N(5')	180.0	N(8)–C(7)–C(6)	123.3(2)
Cu(1)–O(4)–C(4)	108.5(1)	N(1)–C(9)–N(8)	119.3(2)
C(2)–N(1)–C(9)	122.7(2)	N(1)–C(9)–C(10)	118.2(2)
C(2)–N(3)–C(4)	121.8(2)	N(8)–C(9)–C(10)	122.5(2)
Cu(1)–N(5)–C(6)	128.0(1)	N(5)–C(10)–C(4)	119.7(2)
Cu(1)–N(5)–C(10)	114.7(1)	N(5)–C(10)–C(9)	120.9(2)
C(6)–N(5)–C(10)	117.3(2)	C(4)–C(10)–C(9)	119.4(2)
Cu(1)–O(3)–H(31)	123(3)	N(5)–C(6)–H(6)	120(2)
Cu(1)–O(3)–H(32)	120(2)	C(7)–C(6)–H(6)	119(2)
H(31)–O(3)–H(32)	110(3)	N(8)–C(7)–H(7)	121(2)
C(2)–N(1)–H(1)	122(2)	H(7)–C(7)–C(6)	116(2)
C(9)–N(1)–H(1)	115(2)		

In the complex **2**, the coordination sphere of copper(II) ion has an elongated octahedral coordination geometry defined by two N(5) atoms and two O(4) atoms of PR ligands lying in the equatorial plane and by two water molecules at apexes (Figure 2).
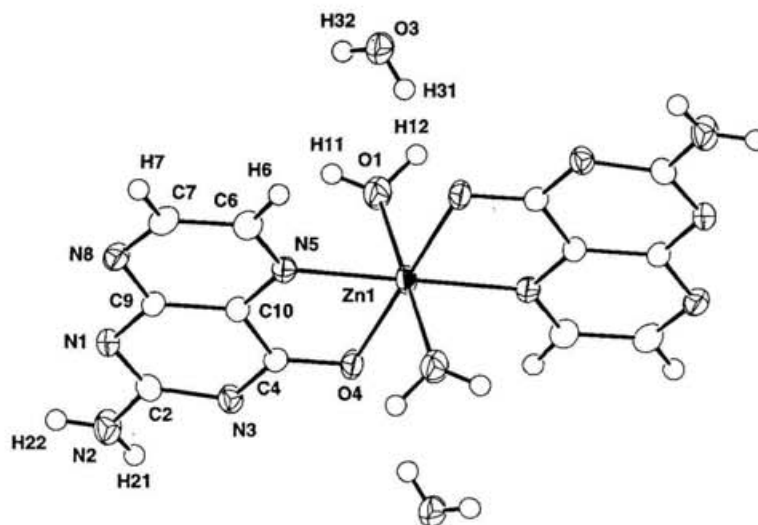

Figure 2. ORETP diagram of **2**, showing the labeling scheme and 50 % thermal ellipsoids.

Table 7. Bond Lengths (Å) and Angles (deg) for $[Cu(PR)_2(H_2O)_2]$ (**2**)

	Distances		
Cu(1)–O(1)	2.586(3)	N(3)–C(4)	1.317(3)
Cu(1)–O(4)	1.985(2)	N(5)–C(6)	1.323(3)
Cu(1)–N(5)	1.976(2)	N(5)–C(10)	1.345(3)
O(4)–C(4)	1.293(3)	N(8)–C(7)	1.323(3)
N(1)–C(2)	1.341(3)	N(8)–C(9)	1.362(3)
N(1)–C(9)	1.350(3)	C(4)–C(10)	1.443(3)
N(2)–C(2)	1.339(3)	C(6)–C(7)	1.406(4)
N(3)–C(2)	1.372(3)	C(9)–C(10)	1.396(3)
O(1)–H(11)	0.88(5)	N(2)–H(22)	0.80(3)

16

O(1)–H(12)	0.75(4)	C(6)–H(6)	0.89(3)
N(2)–H(21)	0.83(3)	C(7)–H(7)	0.94(3)

Angles

O(1)–Cu(1)–O(1')	180.0	C(7)–N(8)–C(9)	116.1(2)
O(1)–Cu(1)–O(4)	95.18(8)	N(1)–C(2)–N(2)	116.6(2)
O(1)–Cu(1)–O(4')	84.82(8)	N(1)–C(2)–N(3)	128.3(2)
O(1)–Cu(1)–N(5)	88.58(8)	N(2)–C(2)–N(3)	115.0(2)
O(1)–Cu(1)–N(5')	91.42(8)	O(4)–C(4)–N(3)	122.7(2)
O(4)–Cu(1)–O(4')	180.0	O(4)–C(4)–C(10)	117.5(2)
O(4)–Cu(1)–N(5)	84.86(7)	N(3)–C(4)–C(10)	119.7(2)
O(4)–Cu(1)–N(5')	95.14(7)	N(5)–C(6)–C(7)	119.5(2)
N(5)–Cu(1)–N(5')	180.0	N(8)–C(7)–C(6)	124.3(2)
Cu(1)–O(4)–C(4)	110.7(1)	N(1)–C(9)–N(8)	119.3(2)
C(2)–N(1)–C(9)	115.4(2)	N(1)–C(9)–C(10)	121.0(2)
C(2)–N(3)–C(4)	116.5(2)	N(8)–C(9)–C(10)	119.7(2)
Cu(1)–N(5)–C(6)	133.7(2)	N(5)–C(10)–C(4)	118.0(2)
Cu(1)–N(5)–C(10)	108.8(2)	N(5)–C(10)–C(9)	122.9(2)
C(6)–N(5)–C(10)	117.5(2)	C(4)–C(10)–C(9)	119.0(2)
Cu(1)–O(1)–H(11)	104(3)	H(21)–N(2)–H(22)	120(3)
Cu(1)–O(1)–H(12)	94(3)	N(5)–C(6)–H(6)	120(2)
H(11)–O(1)–H(12)	110(4)	C(7)–C(6)–H(6)	120(2)
C(2)–N(2)–H(21)	121(2)	N(8)–C(7)–H(7)	117(2)
C(2)–N(2)–H(22)	119(2)	C(6)–C(7)–H(7)	119(2)

In contrast to **2**, the complex **3** has water of crystallization. The coordination sphere of copper(II) ion in **3** has an elongated octahedral coordination geometry defined by two N(5) atoms and two O(4) atoms of PR ligands lying in the equatorial plane and by two water molecules at apexes (Figure 3). The dihedral angle between the plane formed by O(4), Cu(1), and N(5) atoms and the ligand PR plane is 13.04° and the Cu(1) atom deviates by 0.354 Å from the mean plane of the ligand PR.

Figure 3. ORETP diagram of **3**, showing the labeling scheme and 50 % thermal ellipsoids.

17

Table 8. Bond Lengths (Å) and Angles (deg) for [Cu(PR)$_2$(H$_2$O)$_2$] ·2H$_2$O (**3**)

	Distances		
Cu(1)–O(1)	2.417(3)	Cu(1)–O(4)	1.972(2)
Cu(1)–N(5)	2.025(2)	O(4)–C(4)	1.284(3)
N(1)–C(2)	1.345(3)	N(1)–C(8a)	1.354(3)
N(2)–C(2)	1.337(3)	N(3)–C(2)	1.376(3)
N(3)–C(4)	1.323(3)	N(5)–C(4a)	1.349(3)
N(5)–C(6)	1.321(3)	N(8)–C(7)	1.325(3)
N(8)–C(8a)	1.364(3)	C(4)–C(4a)	1.439(3)
C(4a)–C(8a)	1.401(3)	C(6)–C(7)	1.398(4)
O(1)–H(11)	0.75(4)	O(1)–H(12)	0.74(4)
O(3)–H(31)	0.78(3)	O(3)–H(32)	0.77(3)
N(2)–H(21)	0.77(3)	N(2)–H(22)	0.89(3)
C(6)–H(6)	0.92(3)	C(7)–H(7)	0.92(2)
	Angles		
O(1)–Cu(1)–O(1)	180.0	O(1)–Cu(1)–O(4)	87.63(9)
O(1)–Cu(1)–O(4)	92.37(9)	O(1)–Cu(1)–N(5)	87.67(9)
O(1)–Cu(1)–N(5)	92.33(9)	O(1)–Cu(1)–O(4)	92.37(9)
O(1)–Cu(1)–O(4)	87.63(9)	O(1)–Cu(1)–N(5)	92.33(9)
O(1)–Cu(1)–N(5)	87.67(9)	O(4)–Cu(1)–O(4)	180.0
O(4)–Cu(1)–N(5)	84.24(8)	O(4)–Cu(1)–N(5)	95.76(8)
O(4)–Cu(1)–N(5)	95.76(8)	O(4)–Cu(1)–N(5)	84.24(8)
N(5)–Cu(1)–N(5)	180.0	Cu(1)–O(4)–C(4)	110.6(2)
C(2)–N(1)–C(8a)	115.1(2)	C(2)–N(3)–C(4)	116.7(2)
Cu(1)–N(5)–C(4a)	107.3(2)	Cu(1)–N(5)–C(6)	135.4(2)
C(4a)–N(5)–C(6)	116.9(2)	C(7)–N(8)–C(8a)	116.0(2)
N(1)–C(2)–N(2)	117.6(2)	N(1)–C(2)–N(3)	128.3(2)
N(2)–C(2)–N(3)	114.0(2)	O(4)–C(4)–N(3)	121.9(2)
O(4)–C(4)–C(4a)	118.8(2)	N(3)–C(4)–C(4a)	119.3(2)
N(5)–C(4a)–C(4)	117.4(2)	N(5)–C(4a)–C(8a)	123.1(2)
C(4)–C(4a)–C(8a)	119.5(2)	N(5)–C(6)–C(7)	120.2(2)
N(8)–C(7)–C(6)	124.3(3)	N(1)–C(8a)–N(8)	119.6(2)
N(1)–C(8a)–C(4a)	121.0(2)	N(8)–C(8a)–C(4a)	119.4(2)
Cu(1)–O(1)–H(11)	111(2)	Cu(1)–O(1)–H(12)	110(3)
H(11)–O(1)–H(12)	113(3)	H(31)–O(3)–H(32)	101(3)
C(2)–N(2)–H(21)	118(2)	C(2)–N(2)–H(22)	118(1)
H(21)–N(2)–H(22)	118(2)	N(5)–C(6)–H(6)	119(1)
C(7)–C(6)–H(6)	120(1)	N(8)–C(7)–H(7)	115(1)
C(6)–C(7)–H(7)	119(1)		

In the complex **4**, the zinc(II) ion is octahedrally surrounded by two water molecules and by two PR ligands bidentately coordinating through O(4) and N(5) atoms (Figure 4). The ZnN$_2$O$_4$ octahedron is markedly distorted. The Zn(II) ion deviates by 0.443 Å from the mean plane of the ligand PR and the dihedral angle between the plane formed by O(4), Zn(1), and N(5) atoms and the ligand PR plane is 15.29 °.

Figure 4. ORETP diagram of **4**, showing the labeling scheme and 50 % thermal ellipsoids.

Table 9. Bond Lengths (Å) and Angles (deg) for [Zn(PR)$_2$(H$_2$O)$_2$] ·2H$_2$O (**4**)

Distances			
Zn(1)–O(1)	2.169(2)	N(3)–C(4)	1.320(3)
Zn(1)–O(4)	2.059(2)	N(5)–C(6)	1.338(4)
Zn(1)–N(5)	2.162(2)	N(5)–C(10)	1.338(3)
O(4)–C(4)	1.277(3)	N(8)–C(7)	1.323(4)
N(1)–C(2)	1.355(4)	N(8)–C(9)	1.372(4)
N(1)–C(9)	1.343(3)	C(4)–C(10)	1.464(4)
N(2)–C(2)	1.328(4)	C(6)–C(7)	1.403(4)
N(3)–C(2)	1.368(3)	C(9)–C(10)	1.404(4)
O(1)–H(11)	0.83(4)	N(2)–H(21)	0.85(5)
O(1)–H(12)	0.95(5)	N(2)–H(22)	0.86(4)
O(3)–H(31)	0.80(5)	C(6)–H(6)	0.95(4)
O(3)–H(32)	0.75(4)	C(7)–H(7)	1.02(4)
Angles			
O(1)–Zn(1)–O(1')	180.0	C(7)–N(8)–C(9)	116.4(2)
O(1)–Zn(1)–O(4)	88.94(9)	N(1)–C(2)–N(2)	118.2(3)
O(1)–Zn(1)–O(4')	91.06(9)	N(1)–C(2)–N(3)	127.2(2)
O(1)–Zn(1)–N(5)	88.46(9)	N(2)–C(2)–N(3)	114.6(3)
O(1)–Zn(1)–N(5')	91.54(9)	O(4)–C(4)–N(3)	122.0(2)
O(4)–Zn(1)–O(4')	180.0	O(4)–C(4)–C(10)	119.3(2)
O(4)–Zn(1)–N(5)	80.36(8)	N(3)–C(4)–C(10)	118.7(2)
O(4)–Zn(1)–N(5')	99.64(8)	N(5)–C(6)–C(7)	119.3(3)
N(5)–Zn(1)–N(5')	180.0	N(8)–C(7)–C(6)	124.4(3)
Zn(1)–O(4)–C(4)	112.3(2)	N(1)–C(9)–N(8)	118.9(2)
C(2)–N(1)–C(9)	115.5(2)	N(1)–C(9)–C(10)	122.1(2)
C(2)–N(3)–C(4)	118.2(2)	N(8)–C(9)–C(10)	118.9(2)
Zn(1)–N(5)–C(6)	134.4(2)	N(5)–C(10)–C(4)	118.4(2)
Zn(1)–N(5)–C(10)	107.3(2)	N(5)–C(10)–C(9)	123.4(2)
C(6)-N(5)–C(10)	117.4(2)	C(4)–C(10)–C(9)	118.2(2)
Zn(1)–O(1)–H(11)	121(3)	H(21)–N(2)–H(22)	121(4)
Zn(1)–O(1)–H(12)	120(3)	N(5)–C(6)–H(6)	120(2)
H(11)–O(1)–H(12)	110(4)	C(7)–C(6)–H(6)	120(2)
H(31)–O(3)–H(32)	114(5)	N(8)–C(7)–H(7)	119(2)

19

C(2)–N(2)–H(21)	116(3)		C(6)–C(7)–H(7)	117(2)
C(2)–N(2)–H(22)	122(3)			

1. 3. 2 Crystal Structures: Hydrogen-Bonding and Pteridine Stacking.

Packing diagrams and stereoview of the complex **1** are presented in Figures 5–9. H-bonding distances and angles of **1** are listed in Table 10.[33] The molecular units of **1** are linked into a two-dimensional molecular sheet parallel to the *ac* plane via H-bonds between LM and coordinated water molecule (*a* direction: O(3)–H(31)···N(3)[b], *c* direction: O(3)–H(32)···O(4)[c]) (Figures 5 and 6). The molecular sheets are further linked to each other via double H-bonds between LM's (N(1)–H(1)···O(2)[a]) in the [110] direction to form a three-dimensional H-bonded network (Figure 7).   In the sheet, the pyrimidine and pyrazine rings of the LM ligands are stacked uniformly along the *c*-axis with a small overlap.   The mean stacking distance is 3.27 Å (Figure 9).
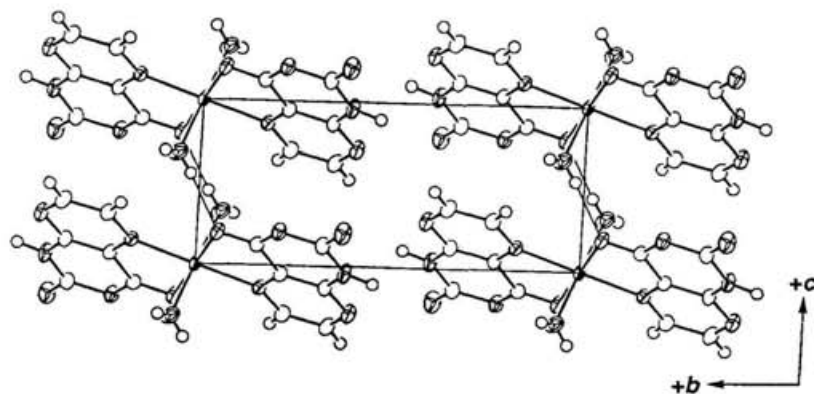
**Figure 5.** Packing diagram projected down to the *a*-axis for **1**.
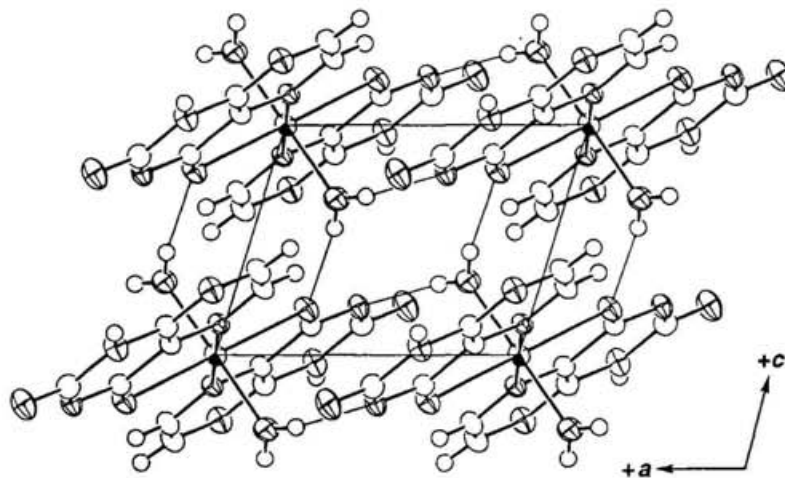
Figure 6. Packing diagram projected down to the *b*-axis for **1**.

20
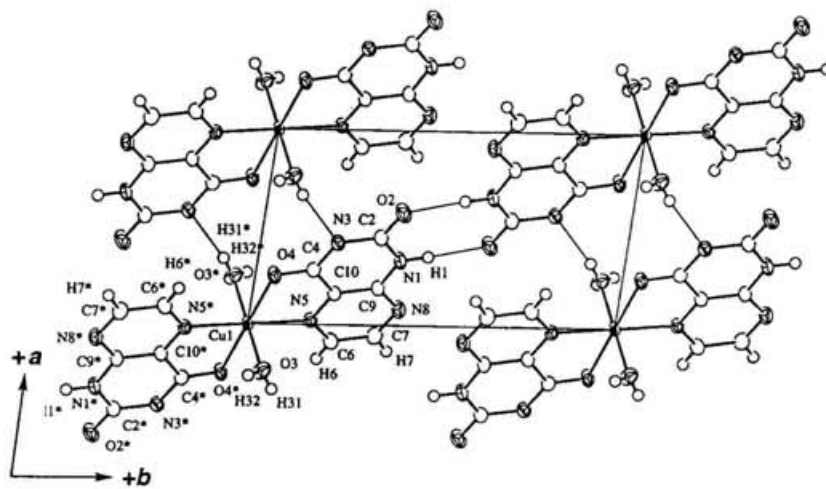
Figure 7. Packing diagram projected down to the *c*-axis for **1**.
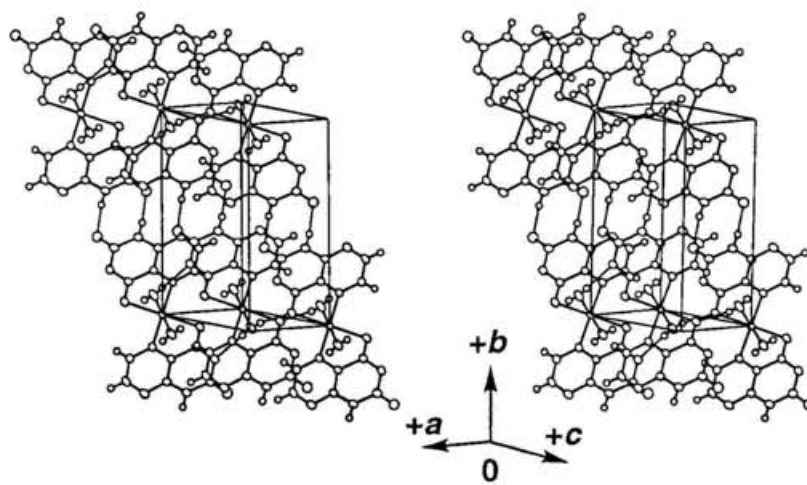
Figure 8. Stereoscopic view of packing of **1**.
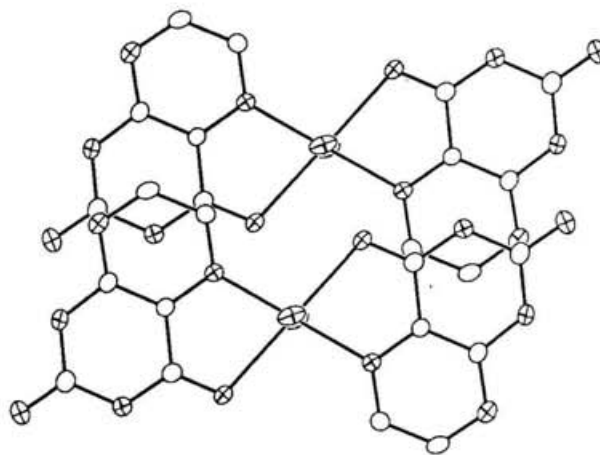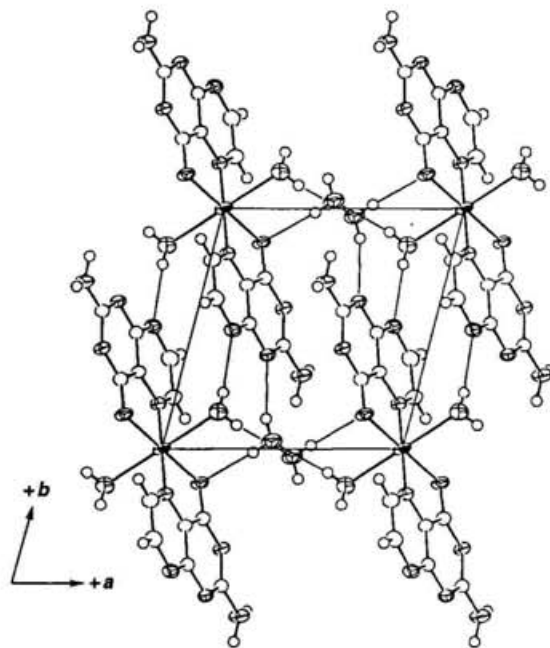

Figure 9. Stacking structure of **1**.

Table 10. H-Bonding Distances and Angles for Complex **1**

D–H···A	D–H Å	H···A Å	D···A Å	D–H···A angle, deg
[Cu(LM)$_2$(H$_2$O)$_2$] (**1**)				
N(1)–H(1)···O(2)^a	0.90(3)	1.96(3)	2.861(2)	173(3)
O(3)–H(31)···N(3)^b	0.68(3)	2.03(3)	2.703(3)	168(3)
O(3)–H(32)···O(4)^c	0.73(3)	1.96(3)	2.667(2)	164(3)

Symmetry operations: ^{a} $1 - x$, $1 - y$, $-z$; ^{b} $-1 + x$, y, z; ^{c} $-x$, $-y$, $-1 - z$.

Packing diagrams and stereoview of the complex **2** are presented in Figures 10–14. H-bonding distances and angles of **2** are listed in Table 11.[33] The molecular units of **2** are linked into a two-dimensional molecular sheet parallel to the *ac* plane via H-bonds between PR and axial water molecule (*c* direction: O(1)–H(11)···N(8)^c and O(1)–H(12)···N(1)^d, [101] direction: N(2)–H(22)···O(1)^b) (Figures 10 and 11). The molecular sheets are connected each other via H-bonds between the molecules related to the screw axis parallel to the *b*-axis (Figure 12), N(2)–H(21)···O(4)^a, to form a three-dimensional H-bonded network. There are two types of PR stacking along the *a*-axis with the alternated distances of 3.39 and 3.27 Å, respectively (Figure 14).
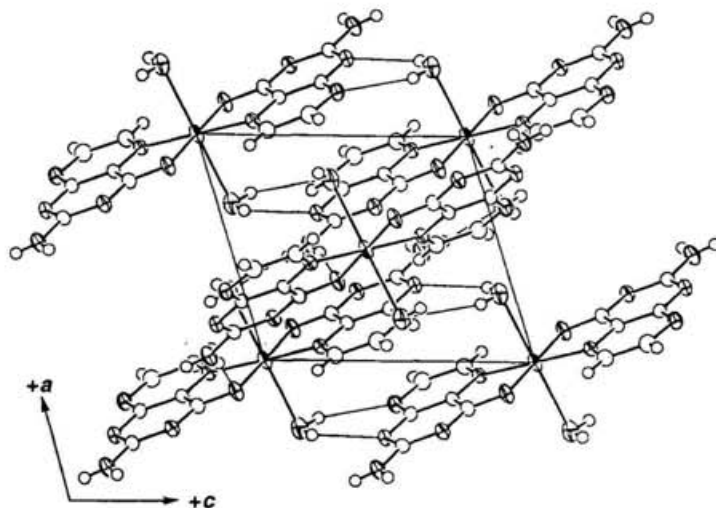
Figure 10. Packing diagram projected down to the *b*-axis for **2**.

22
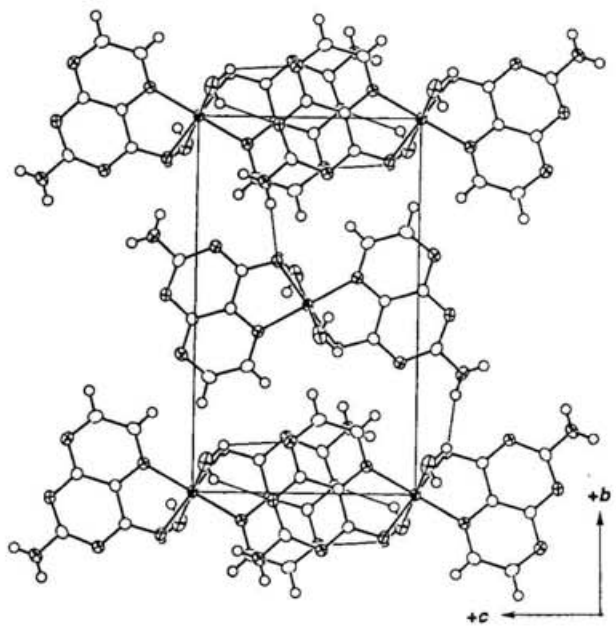
Figure 11. Packing diagram projected down to the *a*-axis for **2**.
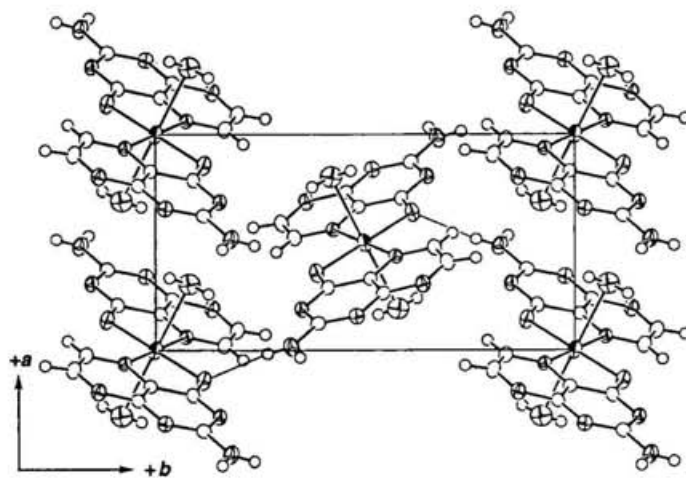
Figure 12. Packing diagram projected down to the *c*-axis for **2**.
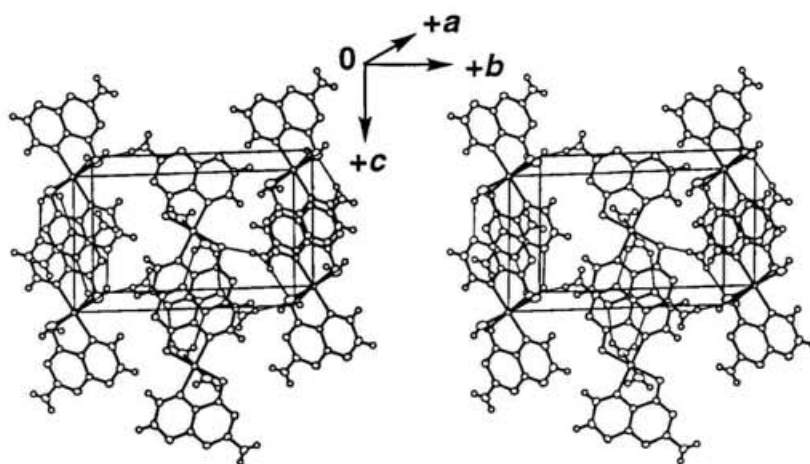
Figure 13. Stereoscopic view of packing of **2**.
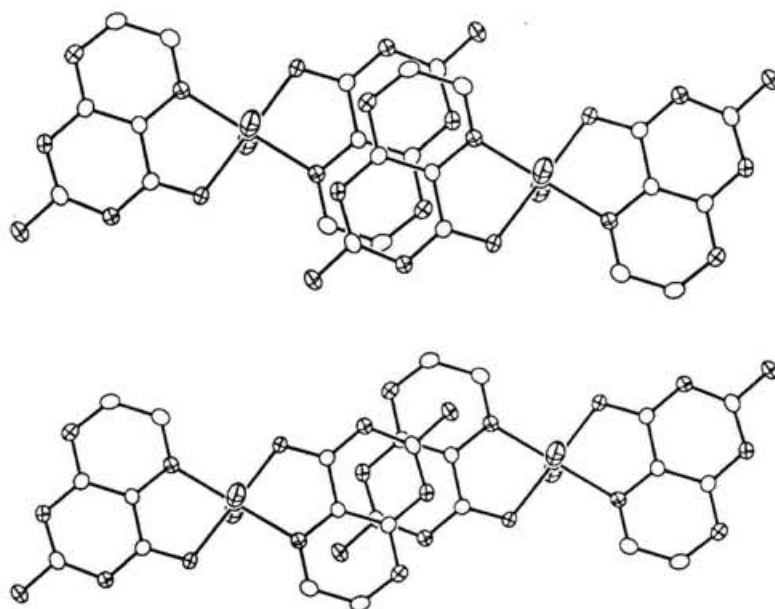
Figure 14. Stacking structure of **2**.

Table 11. H-Bonding Distances and Angles for Complex **2**

D–H···A	D–H Å	H···A Å	D···A Å	D–H···A angle, deg
	$[Cu(PR)_2(H_2O)_2]$ (**2**)			
N(2)–H(21)···O(4)^a	0.83(3)	2.25(3)	3.068(3)	170(3)

N(2)–H(22)···O(1)[b]	0.80(3)	2.28(3)	3.076(3)	172(3)
O(1)–H(11)···N(8)[c]	0.88(5)	2.34(5)	3.055(3)	138(4)
O(1)–H(12)···N(1)[d]	0.75(4)	2.30(4)	2.896(3)	137(4)

Symmetry operations: [a] $1/2 + x$, $-1/2 - y$, $1/2 + z$; [b] $1 - x$, $-y$, $1 - z$; [c] x, y, $-1 + z$; [d] x, y, $-1 + z$.

Packing diagrams and stereoview of the complex **3** are presented in Figures 15–19. H-bonding distances and angles of **3** are listed in Table 12.[33] In **3**, the noncoordinated water molecules are involved in a three-dimensional H-bonded network. The molecular units of **3** are linked into a two-dimensional molecular sheet parallel to the *ab* plane via H-bonds among PR, coordinated and noncoordinated water molecules (*a* direction: O(1)–H(12)···O(3)[d] and O(3)–H(32)···O(4),[f] *b* direction: O(1)–H(11)···N(8),[c] N(2)–H(22)···O(3),[b] and O(3)–H(31)···N(1)[e]) (Figures 15 and 16). The molecular sheets are further linked to each other through double H-bonds of N(2)–H(21)···N(3)[a] between molecular units related by a center of inversion in position [0.5, 0.5, 0.5] to form a three-dimensional H-bonded network (Figure 18). In the sheet, there are two types of PR stacking along the *a*-axis with the alternated distances of 3.24 and 3.21 Å, respectively (Figure 19).

Figure 15. Packing diagram projected down to the *c*-axis for **3**.
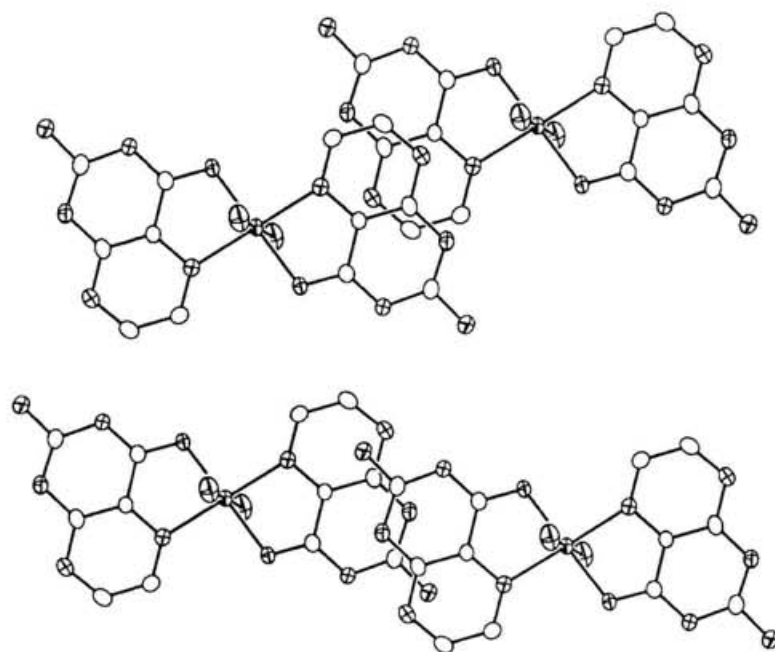
25
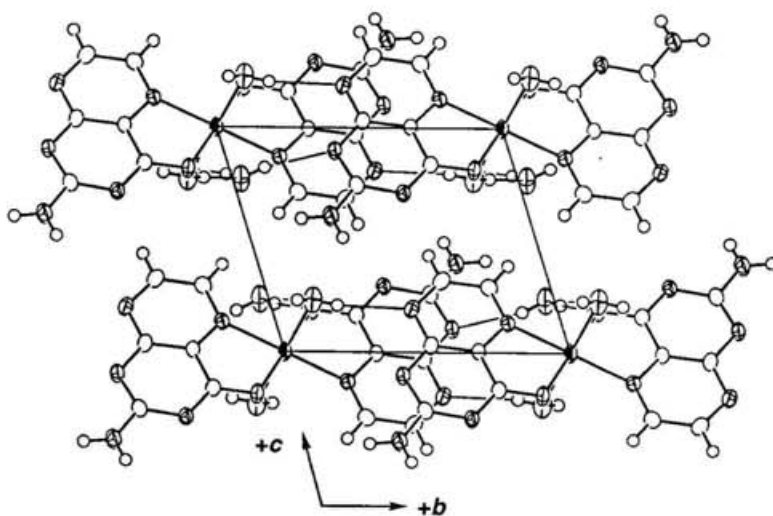
Figure 16. Packing diagram projected down to the *a*-axis for **3**.
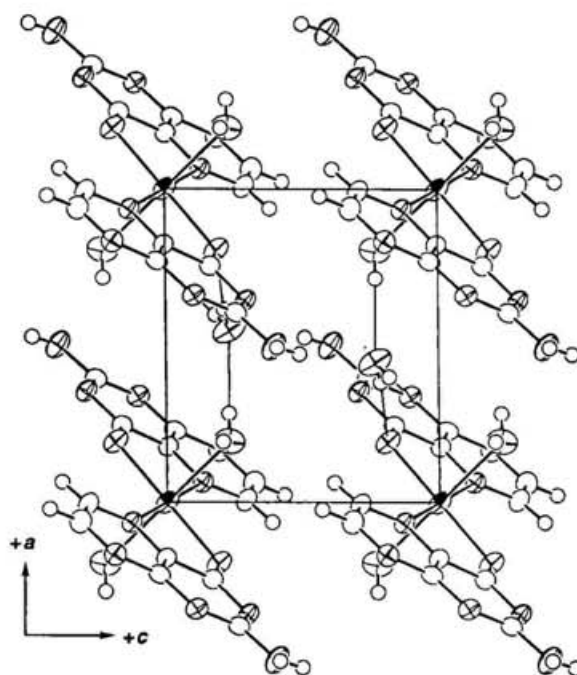
Figure 17. Packing diagram projected down to the *b*-axis for **3**.
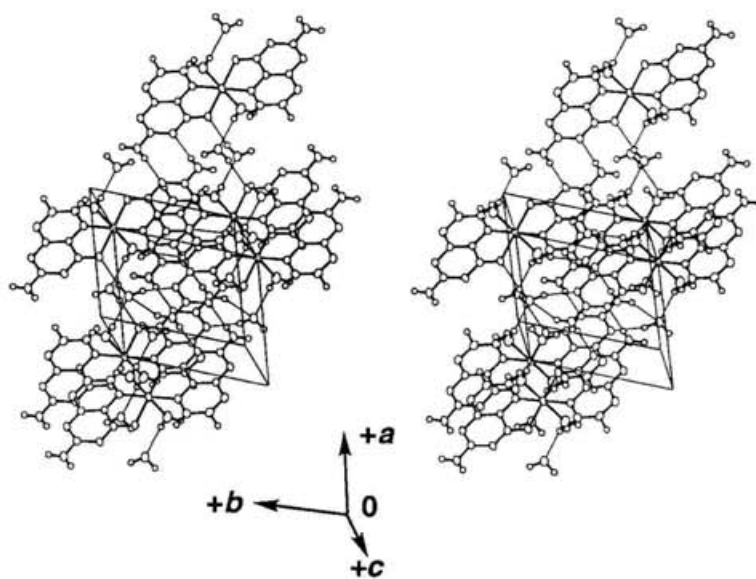
Figure 18. Stereoscopic view of packing of **3**.

Figure 19. Stacking structure of **3**.

Table 12. H-Bonding Distances and Angles for Complex **3**

D–H···A	D–H Å	H···A Å	D···A Å	D–H···A angle, deg
N(2)–H(21)···N(3)[a]	0.77(3)	2.24(3)	2.991(3)	165(3)
N(2)–H(22)···O(3)[b]	0.89(3)	2.29(3)	3.047(4)	143(3)
O(1)–H(11)···N(8)[c]	0.75(4)	2.20(4)	2.949(3)	170(4)
O(1)–H(12)···O(3)[d]	0.74(4)	2.09(4)	2.819(4)	173(4)
O(3)–H(31)···N(1)[e]	0.78(3)	2.10(3)	2.839(3)	159(3)
O(3)–H(32)···O(4)[f]	0.77(3)	2.11(3)	2.871(3)	174(3)

Symmetry operations: [a]$-1-x, 1-y, 1-z$; [b]$-1+x, 1+y, z$., [c]$-x, 1-y, -z$; [d]x, y, z; [e]$1+x, -1+y, z$; [f]$1+x, y, z$;

Packing diagrams and stereoview of the complex **4** are presented in Figures 20–24. H-bonding distances and angles of **4** are listed in Table 13.[33] In **4**, the noncoordinated water molecules are involved in a three-dimensional H-bonded network. The molecular units are linked into a two-dimensional molecular sheet parallel to the *ab* plane via H-bonds between PR and coordinated water molecule (O(1)–H(11)···N(8)[d]), between PR and noncoordinated water molecule (O(3)–H(31)···O(4)[f], O(3)–H(32)···N(1)[g], and N(2)–H(22)···O(3)[b]), and between coordinated and noncoordinated water molecules (O(1)–H(12)···O(3)[e]) (Figures 20 and 21). The molecular sheets are further linked to each other through double H-bonds of N(2)–H(21)···N(3)[a] between molecular units related by a center of inversion in position [0.5, 0.5, 0.5] to form a three-dimensional H-bonded network (Figure 23). In addition, the hydrogen atom H(22) of amino group is also involved intermolecular H-bond, N(2)–H(22)···O(3)[c], with the oxygen atom of uncoordinated water molecule, thus leading to a bifurcated H-bond around H(22). This complex also contains two types of PR stacking along the *a*-axis with the alternated distances of 3.21 and 3.16 Å, respectively (Figure 24).
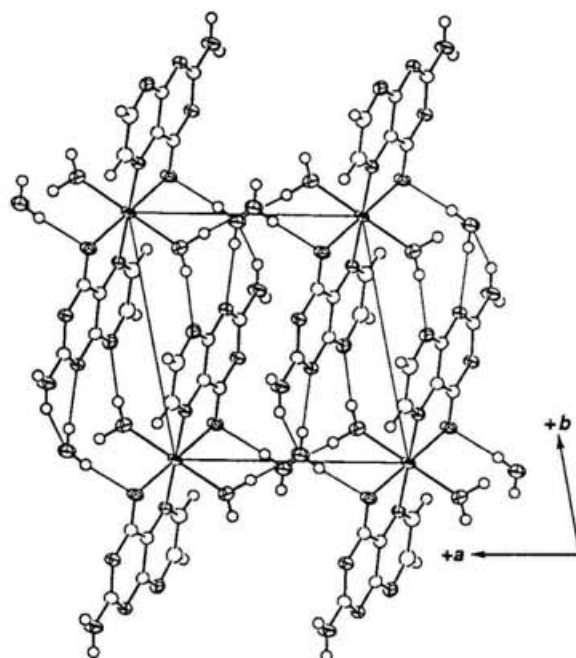
28

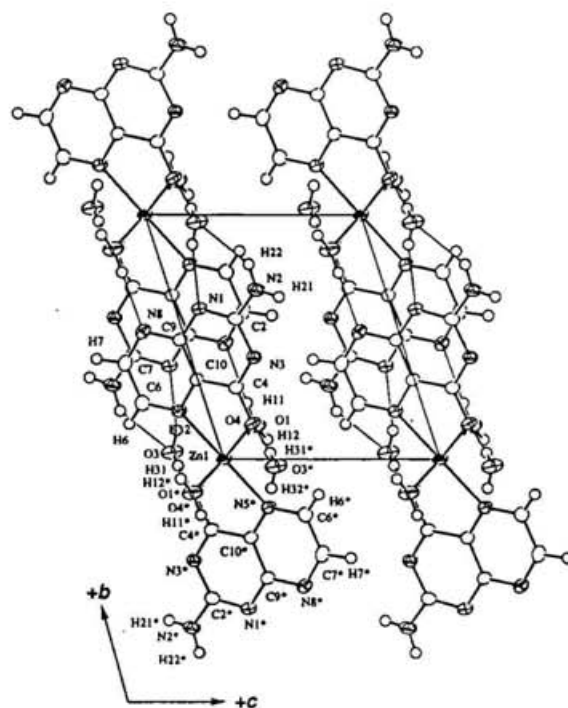**Figure 20.** Packing diagram projected down to the *c*-axis for **4**.
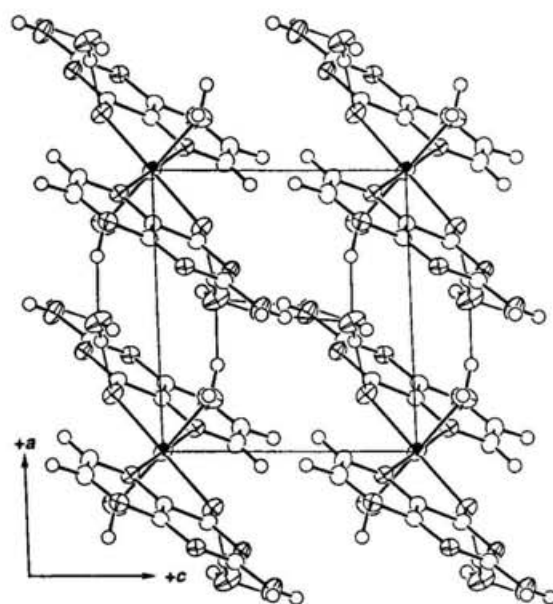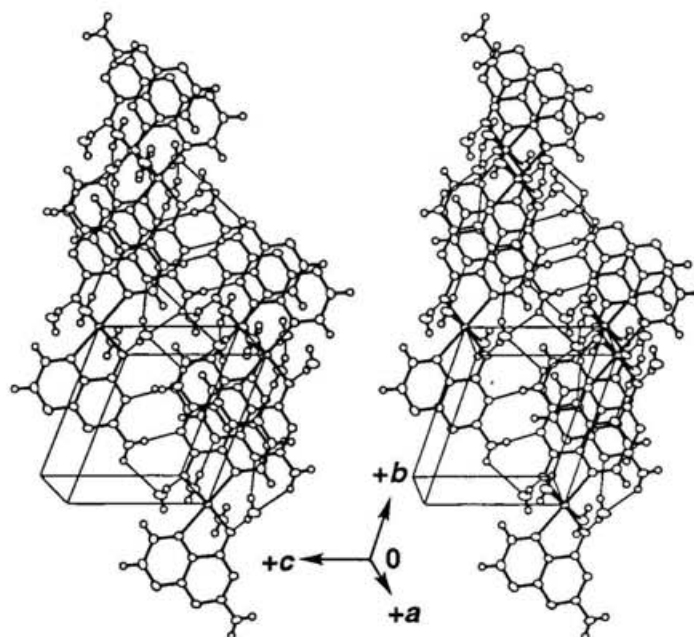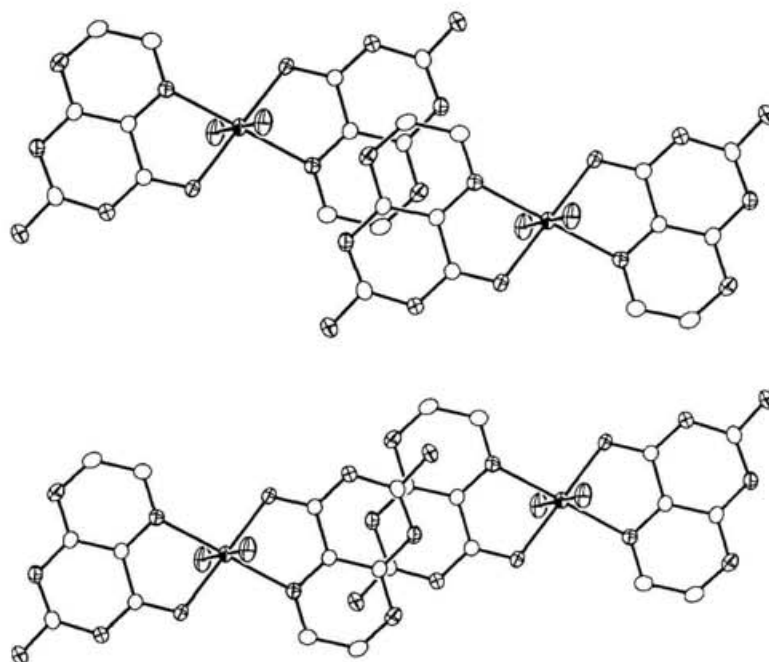

Figure 21. Packing diagram projected down to the *a*-axis for **4**.

Figure 22. Packing diagram projected down to the *b*-axis for **4**.

Figure 23. Stereoscopic view of packing of **4**.

Figure 24. Stacking structure of **4**.

Table 13. H-Bonding Distances and Angles for Complex **4**

D–H···A	D–H Å	H···A Å	D···A Å	D–H···A angle, deg
N(2)–H(21)···N(3)[a]	0.85(5)	2.18(5)	3.015(4)	169(4)
N(2)–H(22)···O(3)[b]	0.86(4)	2.34(4)	3.055(4)	141(4)
N(2)–H(22)···O(3)[c]	0.86(4)	2.63(4)	3.117(4)	117(3)
O(1)–H(11)···N(8)[d]	0.83(4)	2.07(4)	2.900(3)	173(4)
O(1)–H(12)···O(3)[e]	0.95(5)	1.83(5)	2.760(3)	166(4)
O(3)–H(31)···O(4)[f]	0.80(5)	2.03(5)	2.831(3)	175(4)
O(3)–H(32)···N(1)[g]	0.75(4)	2.11(5)	2.837(3)	162(5)

Symmetry operations: [a] $-1-x$, $1-y$, $1-z$; [b] $-x$, $1-y$, $-z$; [c] $-1+x$, $1+y$, $1+z$; [d] $-x$, $1-y$, $-z$; [e] $1-x$, $-y$, $-z$; [f] $-x$, $-y$, $-z$; [g] $-x$, $1-y$, $-z$.

1. 3. 3 IR spectra. The IR spectra of the complexes **1**, **2**, and **4** show substantial shifts to lower frequencies in the region 1750–1550 cm^{-1} compared with the free ligands, which are typical of deprotonation of their neighboring protonated endocyclic nitrogens. Such shifts are nearly identical with the reported values.[18c,19]

31

In general, the shrinkage of the crystal lattice with an increase in pressure or a decrease in temperature causes an increase of the intermolecular interaction. If the π-electron configurational change induced by a proton transfer from proton donor atom to proton acceptor atom in the H-bond occurs by such the external fields, there is the possibility of occurrence of intermolecular CT interaction or metal–ligand CT interaction. Take into account the acidity of proton donor site, it is considered that the mobility of an amide proton is higher than that of an amino proton. In order to obtain the information on the vibrational states of the proton, the temperature dependence and pressure dependence of the IR spectra for the complex **1** which has the H-bonded amide proton were measured.
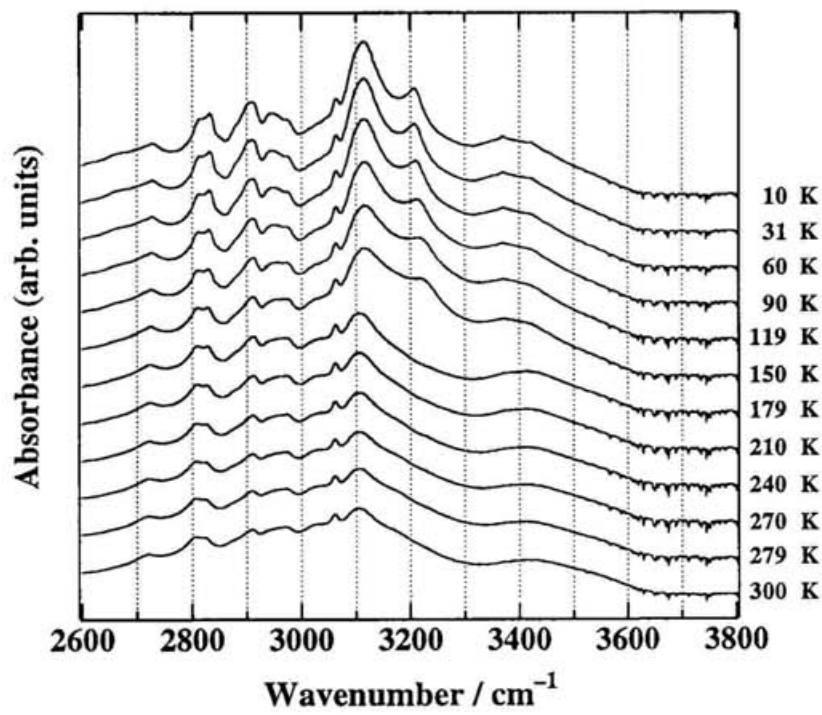
The temperature dependence of the IR spectra for **1** in the temperature range of 10–300 K is shown in Figures 25–27. Nakamoto,[36a] Novak,[36b] and Lautié[36c] have used graphical presentations to show the correlation between N–H, O–H stretching frequencies and the corresponding N$\cdots$O and O$\cdots$O interatomic distances of H-bonded groups (Figure 30). The O(3)–H(31), O(3)–H(32) and N(1)–H(1) stretching frequencies of **1** estimated from the X-ray data using these correlations are 3120, 3110 and 3080 cm^{-1} (Figure 26). A broad band near 3420 cm^{-1} is attributable to absorption of water contained in the KBr pellet because this band is absent in the nujol mull spectrum (Figure 28). The spectra in the region 1400–1800 cm^{-1} show little spectral change on lowering the temperature (Figure 26). The spectra in the region 2600–3800 cm^{-1} also do not change until 179 K (Figure 27). At 150 K, a new absorption band appears at 3220 cm^{-1}. Below this temperature, the intensity of IR spectrum is increase with a decrease in temperature. On lowering the temperature, the two bands near 3100 and 3200 cm^{-1} slightly shift to higher and lower frequency, respectively. However, the peak profile does not change essentially. Thus, the results of the IR spectra also suggest that the thermally induced proton transfer process would not occur in the complex **1**.

The absorption measurements for the complex **1** under hydrostatic pressure were performed by use of a diamond-anvil high pressure cell and the results are shown in Figures 28 and 29. In the frequency region of 2500–3500 cm^{-1}, the spectra are essentially unchanged with an increase in the pressure except the decrease in absorbance and slight lower energy shift of a band at 3097 cm^{-1}. The bands in the region of 1400–1800 cm^{-1} slightly shift to higher frequencies

32

with an increase in the pressure. Generally, an increase in pressure can cause a variety of changes in the vibrational spectra of solids, the most usual being a general increase in the frequencies of fundamental molecular bands.[37] It arises because compression increases the forces of repulsion between neighboring molecules and between atoms and groups within individual molecules and so steepens the curvatures of the potential wells that govern the vibrations. In the case of ν(D-H) stretching bands of H-bonded groups of the type D–H$\cdots$A, the ν(D-H) stretching bands often undergo large shifts to lower frequencies with increasing pressure. Such behavior has been explained by suggesting that when the D$\cdots$A distance is reduced by compression, the electrostatic attraction between the proton and the A atom increases, thus lengthening the D–H bond and reducing its restoring force and stretching frequency. However, no noticeable change of the spectrum which is attributable to pressure-induced proton transfer was observed for the complex 1 with increasing pressure up to 25.5 kbar (1 kbar = ca. 986.920 atom).
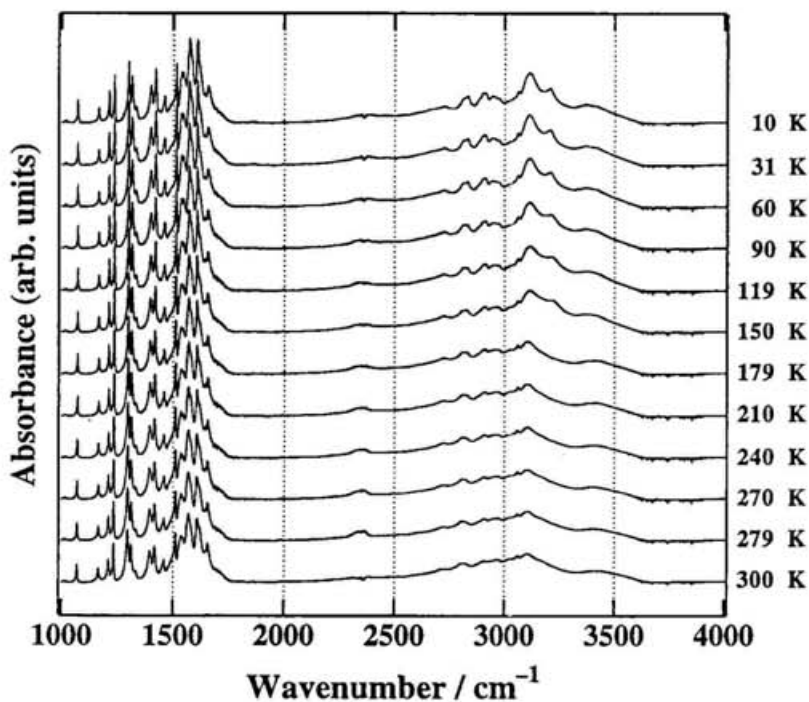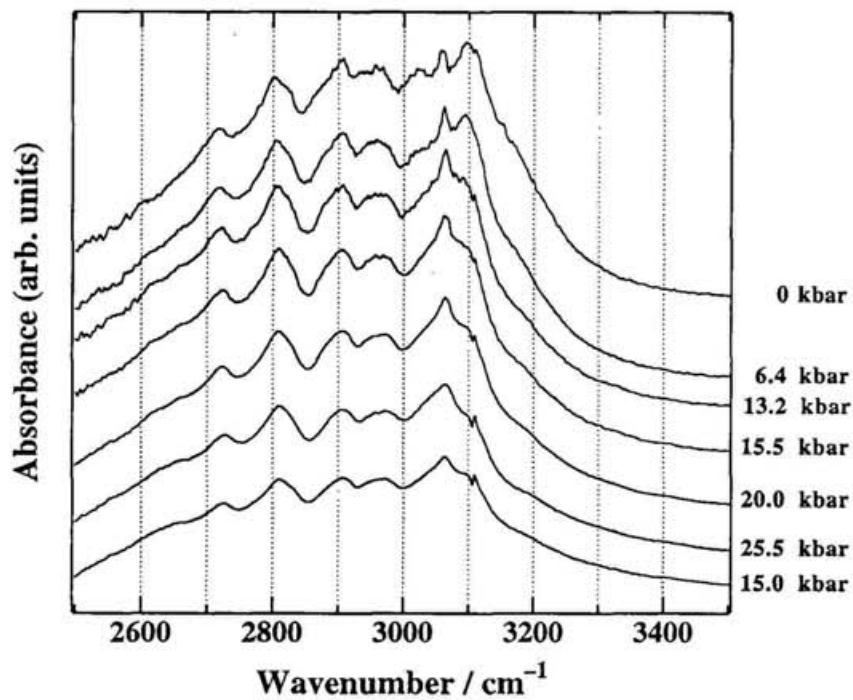

Figure 25. Temperature dependence of IR spectra for complex **1** in the region 1000–4000 cm^{-1}.
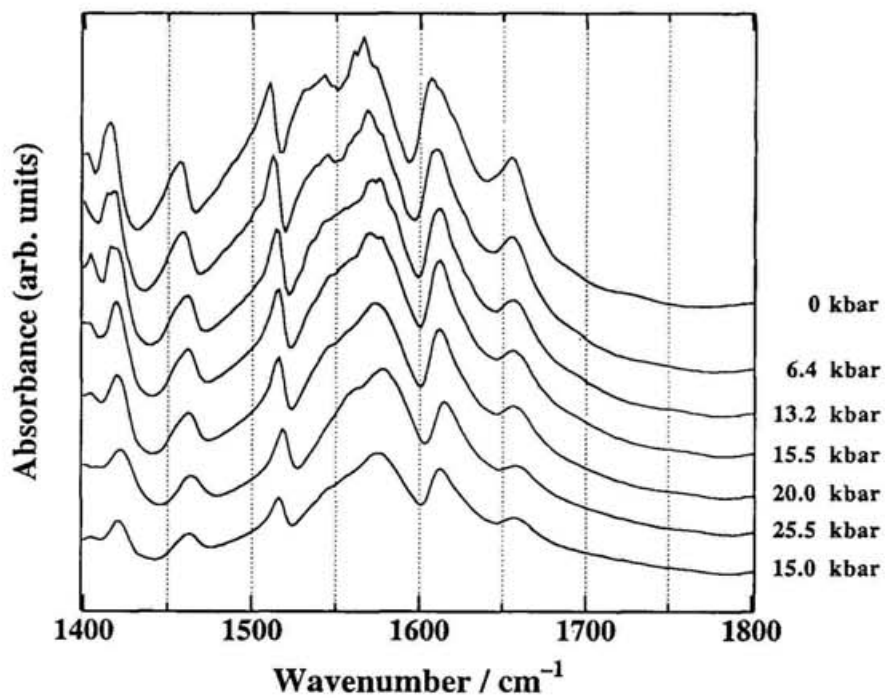
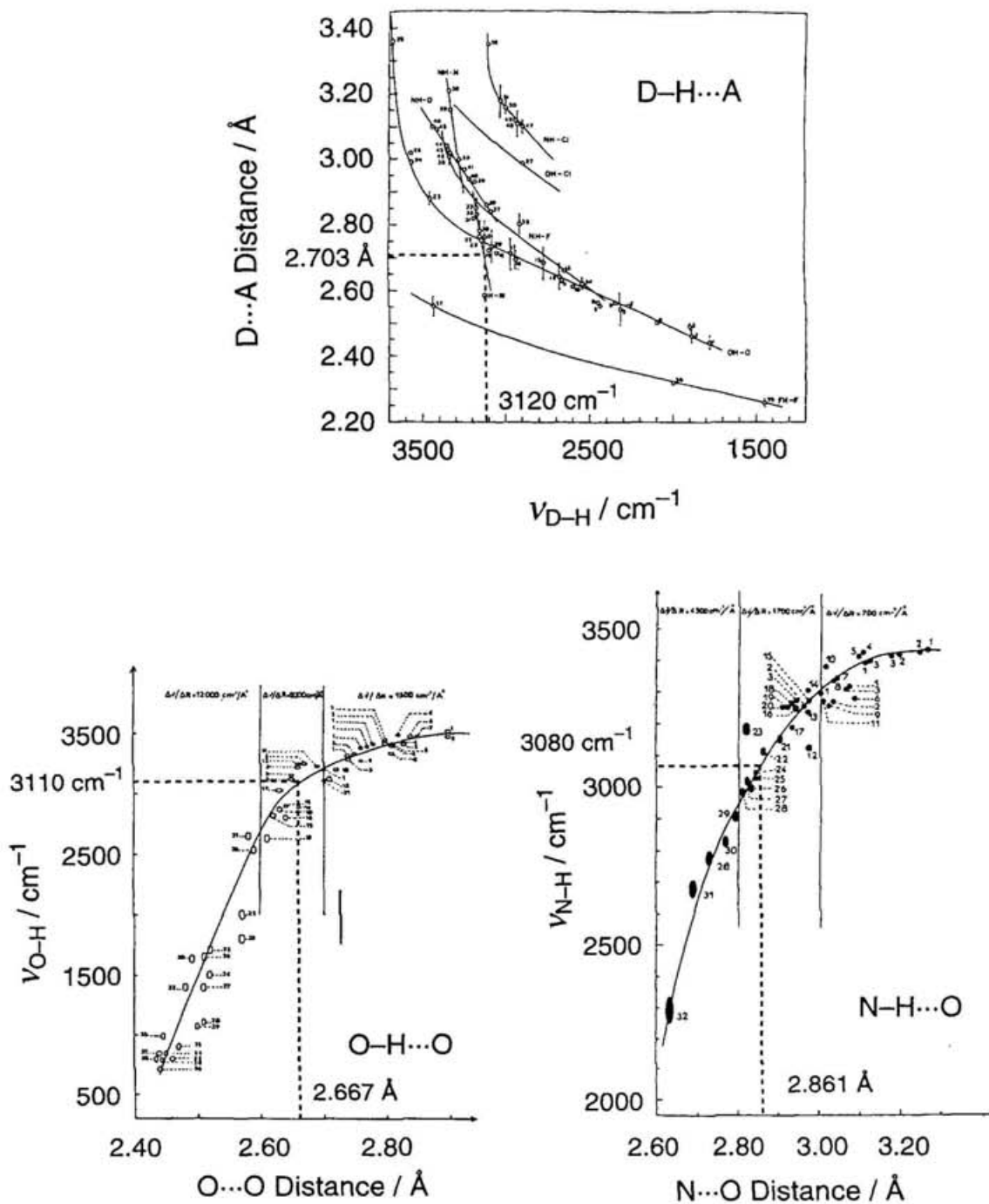**Figure 26.** Temperature dependence of IR spectra for complex **1** in the region 2500–3500 cm^{-1}.
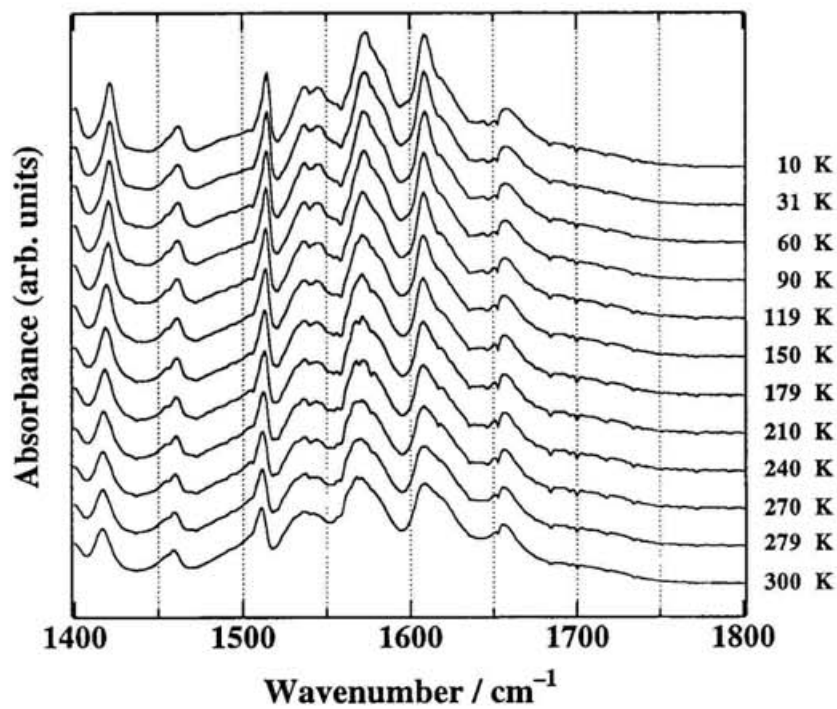
Figure 27. Temperature dependence of IR spectra for complex **1** in the region 1400–1800 cm^{-1}.

34

Figure 28. Pressure dependence of IR spectra for the complex **1** in the region 2500–3500 cm^{-1}.

Figure 29. Pressure dependence of IR spectra for the complex **1** in the region 1400–1800 cm^{-1}.

35

Figure 30. Correlation between D–H stretching frequency and H–bond (D–H⋯A) distance.

1.4 Conclusion

The crystallization of H-bonded metal–pteridine complexes could be made successfully utilizing a diffusion procedure of the deprotonated ligands and metal source in water. The characteristic features in the crystal structures of the

H-bonded metal complexes studied here are as follows: (1) the two pteridines ligands chelate to metal ions through the O(4) and N(5) donor atoms of pteridines, (2) the molecular units are connected to two-dimensional H-bonded molecular sheets by the coordinated water molecules, (3) in the molecular sheet, there are stacking structures of the pteridine skeleton, (4) the sheets are further connected to three-dimensional H-bonded networks via the H-bonded sites of the pteridines ligands, and (5) almost all H-bonding sites existing in the molecule participate in intermolecular H-bonding interactions.

Taking into account the intermolecular interaction by face to face overlap of molecules, it is necessary to form the stacking structure described in general introduction. The complexes **1–4** have not π–d and d–d interactions due to the elongated octahedral coordination geometry of them, but have the π–π type stacking structure of pteridine moieties. However, an absorption which is attributable to intermolecular CT band has not been observed for **1–4**.

If the π-electron configurational change induced by a proton transfer from amide nitrogen to amide oxygen occurs with an increase in pressure or a decrease in temperature, there is the possibility of occurrence of intermolecular CT interaction or metal–ligand CT interaction. In order to obtain the information on the vibrational states of the proton, the temperature dependence and pressure dependence of the IR spectra were measured. However, the temperature dependence and pressure dependence of IR spectra of the complex **1** in the regions of a CO band and a D–H band do not show the spectral change which is attributable to the proton transfer.

One approach to introduce CT interaction into the system is the use of 7,7,8,8-tetracyanoquinodimethane (TCNQ). Advantage of the use of TCNQ is that (1) the TCNQ which has cyano groups is possible to form H-bond with metal complex, (2) the composite compounds[38] composed from copper chelate and TCNQ compounds have a possibility of a partial electron transfer between copper and TCNQ and (3) a TCNQ system having a fractional charge per TCNQ and uniform stack exhibits high electrical conductivity. Attempts to obtain the compound consisted of the complexes **1–4** and TCNQ were unsuccessful due to the insolubility of the these complexes in solvent. Furthermore, another attempt to obtain $Cu(HLM)_2(TCNQ)_x$ from the reaction of LiTCNQ/TCNQ, $[Cu(MeCN)_4]PF_6$ and HLM utilizing the diffusion method was also unsuccessful.

Chapter 2: New Planar Mixed-Valence Dicopper(II,I) Complexes

2.1 Introduction

In Chapter 1, the crystal structure of the metal–pteridine complexes having three-dimensional hydrogen-bonded (H-bonded) network and stacking between pteridine ligands were described. However, it was very difficult to introduce the intermolecular charge-transfer (CT) interaction into these complexes. In this Chapter, the author's attention has been given to the intervalence transfer (IT) interaction of the mixed-valence complex. A model for the hydrogen-bonded charge-transfer (HBCT) system along this strategy is schematically illustrated in Figure 1. This

Delocalized State   Localized State
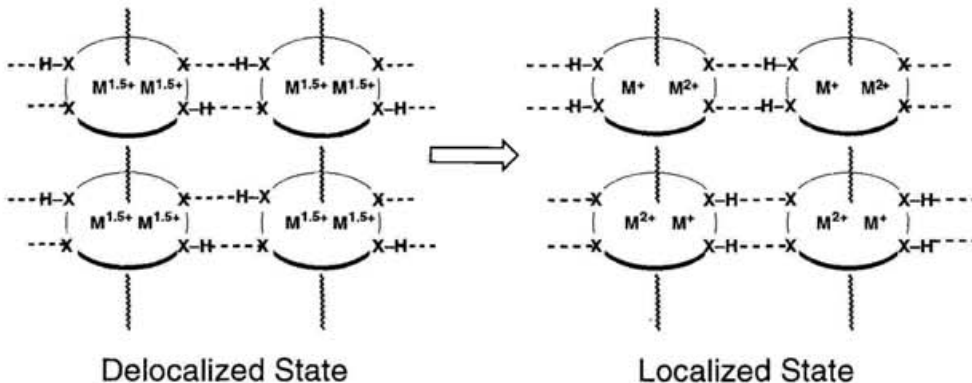
Figure 1. Schematic representation for HBCT system based on planar mixed-valence dimetal(II,I) complex

model represents the molecular assembly which contains the intermolecular interaction: in horizontal, H-bonded interaction and in vertical, stacking interaction (π–π, π–d, d–d interactions) capable of intermolecular electron delocalization. Taking into account the face to face overlap of molecules, planar structure is suitable for the geometry of desired complex. In delocalized state, the effect of delocalized electron on H-bond is equivalent. If the conversion from the delocalized state to the localized state occurs with an increase in pressure or a decrease in temperature, these is the possibility of proton transfer accompanying the

localization of delocalized electron. The goal of this research is exploration of new molecular assemblies with unique solid-state properties originated in the proton–electron transfer (PET) phenomena. As basic research for the study of the HBCT system, one must first construct the molecular assembly as shown in Figure 1. This research effort has been directed toward the construction of such molecular assembly. From the viewpoint of the planarity and the easy electron transfer between the different valence states, the mixed-valence dicopper(II,I) complexes were selected.

The mixed-valence dicopper(II,I) complex are extensively studied in terms of the intramolecular electron-transfer[40] and as a model of the CuA biological electron transfer site in the metalloenzymes[41] and a number of mixed-valence dicopper(II,I) complexes have been prepared and characterized. A theoretical framework for understanding mixed-valence complexes has been developed by Hush.[42] In this formalism, the characteristic electron delocalization parameter for a mixed-valence complex is α^2, which is defined in eq 1 where the ground state wave

$$|G> = (1 - \alpha^2)^{1/2}|\phi[Cu_A(II)Cu_B(I)]> + \alpha|\phi[Cu_A(I)Cu_B(II)]> \quad (1)$$

function is expressed in terms of the wave functions for two states in which the unpaired electron is localized completely on either Cu_A or Cu_B. Robin and Day[43] have classified the behavior of mixed-valence complexes based on the value of α^2 in general, and have divided the behavior into three Classes, I–III, as summarized in Table 1, and applied to the element copper.

As one can see from Table 1, in order to delocalize the unpaired electron on both different valence state, the stereochemistry for different oxidation states must be indistinguishable or nearly identical symmetry. Most of the mixed-valence dicopper(II,I) complexes usually have different stereochemistry of the copper sites and the unpaired electron is completely localized on Cu_A ($\alpha^2 = 0$), which are classified into the Class I. Several mixed-valence dicopper(II,I) complexes or dicopper protein active sites clearly exhibit the delocalization of single unpaired electron

39

Table 1. Characteristics of Mixed-Valence Compounds

Class I	Class II	Class III-A	Class III-B
Metal ions in ligand fields of very different symmetry and/or strength	Metal ions in ligand fields of nearly identical symmetry, differing from one another by distortions of only a few tenths Å	Metal ions indistinguishable but group into polynuclear clusters	All metal ions indistinguishable
$\alpha = 0$; Valences very firmly trapped	$\alpha > 0$; Valences distinguishable, but with slight delocalization	α maximal locally	α maximal; complete delocalization over the cation sublattice
Insulator; resistivity of 10^{10} Ω cm or greater	Semiconductor; resistivity in the range $10-10^7$ Ω cm	Probably insulating	Metallic conductivity; resistivity in the range $10^{-2}-10^{-6}$ Ω cm
No mixed valence transitions in visible region	One or more mixed valence transitions in the visible region	One or more mixed valence transitions in the visible region	Absorption edge in the infrared, opaque with metallic reflectivity in the visible region
Clearly shows spectra of constituent ions, IR, UV, Mössbauer	Shows spectra of constituent ions at very nearly their normal frequencies	Spectra of constituent ions not discernible	Spectra of constituent ions not discernible
Magnetically dilute, paramagnetic or diamagnetic to very low temperatures	Magnetically dilute, both ferromagnetic and antiferromagnetic interactions at low temperatures	Magnetically dilute	Either ferromagnetic with a high Curie temperature or depending upon the presence or absence of local moments

40

on both copper sites above temperature 77 K (Class II behavior).[44] Delocalization of the unpaired electron in Class II complexes is in the range $0 < \alpha^2 < 0.5$. Only recently there have been reports of the cryptate or thiolate-bridged type mixed-valence dicopper(II,I) complexes which show the complete valence delocalization ($\alpha^2 = 0.5$, Class III behavior) mediated by a copper–copper bond or thiolate-bridges.[45] Further, several Class II or III mixed-valence complexes are characterized by the X-ray analysis and those structures are summarized in Figure 2. Although most of those are non-planer geometry, the only $[Cu_2(L^2)](ClO_4) \cdot 0.5MeOH^{44c}$ has the planar geometry. However, the stereochemistry of dicopper site in this complex is non-equivalent.

In order to obtain new planar mixed-valence dicopper(II,I) complex in which both copper sites have equal coordination geometry, it is necessary to design the effective dinucleating ligand which imposes steric constraint upon the coordination geometry. In this viewpoint, 2-(2'-pyridyl)-4(3H)-pyrimidinone derivatives, HL1–HL4, as dinucleating tridentate ligand were designed and synthesized. In consideration of the


HL1[a] R = H
HL2[a] R = Me

HL3[b] R = H
HL4[b] R = Me

[a]known compound
[b]unknown compound
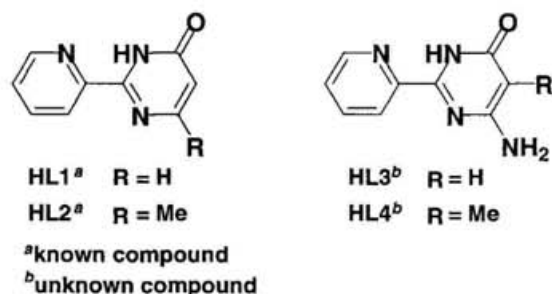
intermolecular H-bonding, an amino group was introduced for HL3 and HL4. With respect to general preparation method[46], the mixed-valence copper(II,I) complexes are prepared (1) from a mixture of copper(II) and copper(I) starting materials or (2) from a copper(II) starting material and mild chemical reduction or controlled electrochemical reduction or (3) from a copper(I) starting material and chemical oxidation. In this study, a new family of mixed-valence dicopper(II,I) complexes **1–4** shown in Figure 3 were successfully prepared from a mixture of $Cu(PF_6)_2$ and $[Cu(MeCN)_4]PF_6$ according to method 1. This Chapter describes the syntheses, crystal structures, and the results of magnetic,
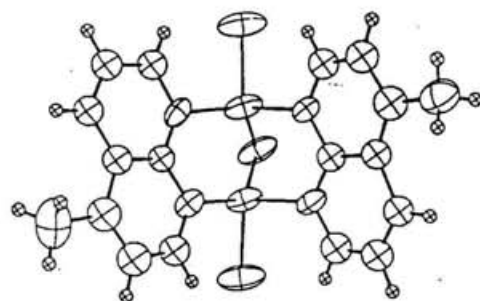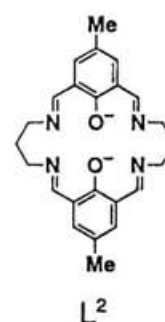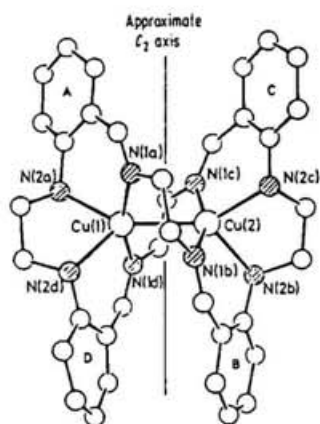
$[Cu_2Cl_3(L^1)_2]$
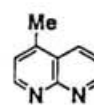
L^1
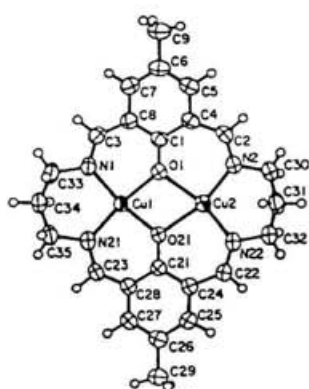
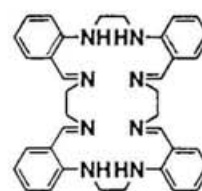$[Cu_2(L^2)]$ cation of $[Cu_2(L^2)](ClO_4)\cdot 0.5MeOH$

L^2

$[Cu_2(L^3)]$ cation of $[Cu_2(L^3)](ClO_4)_3$

L^3

Figure 2. Structures of Class II or III mixed-valence dicopper(II,I) complexes.

42
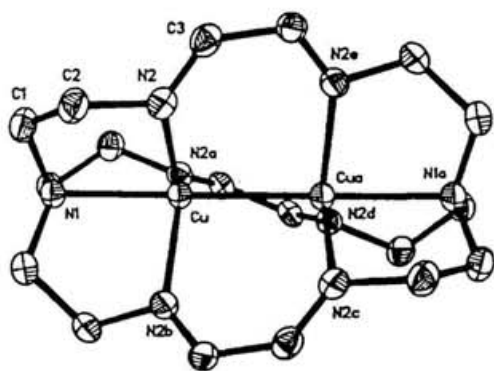
[Cu$_2$(L^4)]$^{2+}$ cation of [Cu$_2$(L^4)](ClO$_4$)$_2$
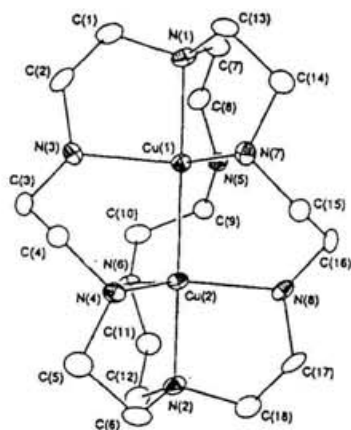
[Cu$_2$(L^5)]$^{3+}$ cation of [Cu$_2$(L^5)](NO$_3$)·2H$_2$O
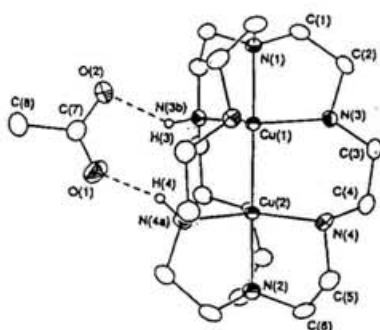
[Cu$_2$(L^5)]$^{3+}$ cation of [Cu$_2$(L^5)](CH$_3$CO$_2$)·6H$_2$O
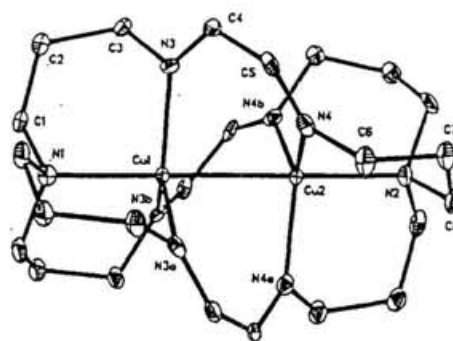
[Cu$_2$(L^6)]$^{3+}$ cation of [Cu$_2$(L^6)](ClO$_4$)$_3$

L^4

L^5

L^6
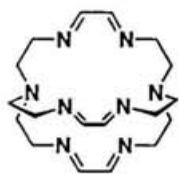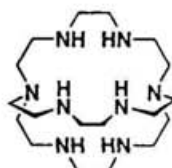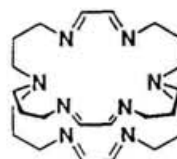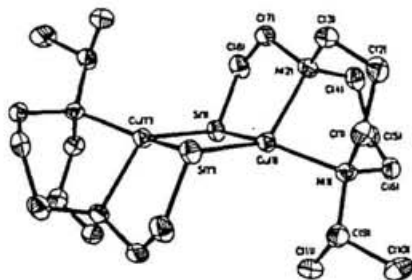
[{Cu(L^7)}$_2$]$^{3+}$ cation of [{Cu(L^7)}$_2$](CF$_3$SO$_3$)
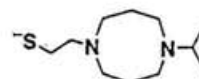
L^7

Figure 2. (Continued)

43

electronic spectroscopic, electrochemical, EPR, and XPS investigations of the mixed-valence dicopper(II,I) complexes 1–4.

[{Cu(L1)}₂]PF₆ (1)

[{Cu(L2)}₂]PF₆ (2)

[{Cu(L3)}₂]PF₆·DMF (3)

[{Cu(L4)}₂]PF₆·0.5MeOH (4)
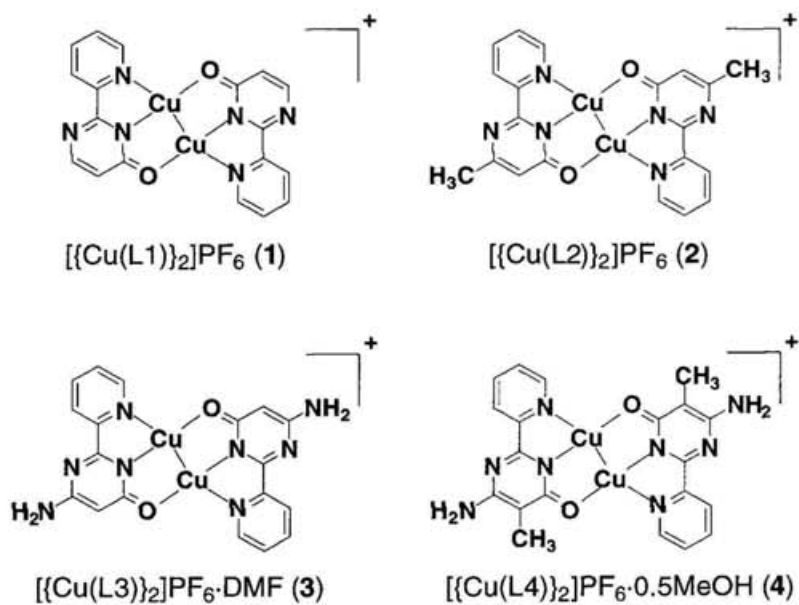
Figure 3. A new family of mixed-valence dicopper(II,I) complexes 1–4

2. 2 Experimental Section

2. 2. 1 Measurements

Melting points were measured on a Yanaco micro melting point apparatus and are uncorrected. IR spectra were recorded as KBr pellets on a Perkin-Elmer 1600 Series FT-IR spectrophotometer and are reported in wave numbers (cm^{-1}). ^{1}H NMR spectra were recorded on a JEOL JNM-EX 270 FT NMR spectrometer. Chemical shifts are expressed in parts per million (ppm, δ) downfield from tetramethylsilane (TMS) as internal standard. UV–visible–Near-IR spectra were recorded on a SHIMADZU UV–3100PC UV–vis–NIR scanning spectrophotometer. Electron ionization mass spectra (EI-MS) were recorded with a SHIMADZU QP-5000 spectrometer with an ionization energy of 70 eV. Temperature dependences of magnetic susceptibilities of the crystalline samples were measured in the temperature range of 2–280 K at a field 1 T using a Quantum Design Model MPMS-5 SQUID susceptometer. Field dependences of magnetization up to 5.5 T were made on a Quantum Design Model MPMS-5 SQUID susceptometer. Diamagnetic corrections were made with Pascal's constants.[47] EPR spectra were recorded at X-band frequency on a JEOL JES-FE2XG spectrometer. The microwave frequency was counted by a Hewlett-Packard 5343A microwave frequency counter. Cyclic voltammetry and differential pulse voltammetry were performed at room temperature under argon by using a Yanaco Polarographic Analyzer P-1100 instrument and a standard three-electrode assembly (glassy-carbon working, Pt-wire auxiliary, SCE reference) with 0.1 M NBu$_4$ClO$_4$ as the supporting electrolyte. Quoted potential values are versus the ferrocene/ferrocenium couple measured under the same conditions. The concentration of the complexes was approximately 1mM. Controlled potential coulometry experiments were carried out with use of BAS CV-50W Voltammetry Analyzer with a platinum gauze for the working electrode and a platinum coil for auxiliary electrode. The X-ray photoelectron spectra (XPS) were recorded on a JEOL model JESCA–3A spectrometer. Mg Kα radiation (1253.6 eV) was used as X-ray excitation source and the measurements

were carried out at $1 \times 10^{-9} - 2 \times 10^{-9}$ mbar. Elemental analyses (carbon, hydrogen and nitrogen) were obtained from the Service Center of Elemental Analysis at Graduate School of Science, Osaka University. Molecular orbital calculations were performed with the ZINDO[48] programs on the CAChe suite of programs available from Tektronix, version 3.7. The geometry of the complex cation in **1** and **3** were taken from the X-ray crystal coordinates for **1** and **3**. The INDO/1 parametrization method of Pople[49] was used in all calculations. The unrestricted Hartee–Fock self-consistent field method was used to generated molecular orbitals in iterative fashion.

2. 2. 2 Materials

Unless noted otherwise, all starting materials were obtained from commercial suppliers and used without further purification. Solvents were dried according to published procedures and distilled under an argon immediately prior to use.[22] Tetrakis(acetonitrile)copper(I) hexafluorophosphate, $[Cu(MeCN)_4]PF_6$, was prepared by a literature method.[24] All air-sensitive reactions were performed under dry argon atmosphere by using the standard Schlenk or vacuum-line technique but products were worked up in the open atmosphere. 2-Pyridinecarboximidamide hydrochloride was prepared by a literature method.[50a] 2-(2'-Pyridyl)-4(3*H*)-pyrimidinone derivatives, HL1 and HL2, as dinucleating tridentate ligands, were synthesized according to the published procedures.[50,51]

2. 2. 3 Preparations

6-Amino-2-(2'-pyridyl)-4(3*H*)-pyrimidinone (HL3). To a solution of sodium (3.65 g, 159 mmol) in 130 mL of ethanol was added 2-pyridinecarboximidamide hydrochloride (15.7 g, 99.5 mmol) and ethyl cyanoacetate (13.0 g, 115 mmol). The mixture was heated under reflux for 6 h with stirring. After cooling, most of the ethanol was removed on a rotary evaporator. The residue was suspended in 140 mL of water and the aqueous suspension was adjusted to pH 5 with acetic acid. The

separated light greenish yellow solid was collected, washed with water. The crude product was recrystallized twice from ethanol to afford 4.26 g (23 %) of colorless crystals: mp > 300 °C; ^{1}H NMR (270 MHz, DMSO-d_6) δ 10.83 (s, 1H, NH), 8.72 (ddd, 1H, J = 4.8, 1.4, 0.9 Hz, 2-pyrigyl-6'H), 8.23 (ddd, 1H, J = 7.8, 1.1, 0.9 Hz, 2-pyrigyl-3'H), 8.04 (ddd, 1H, J = 7.8, 7.6, 1.4 Hz, 2-pyrigyl-4'H), 7.63 (ddd, 1H, J = 7.6, 4.8, 1.1 Hz, 2-pyrigyl-5'H), 6.62 (s, 2H, NH$_2$), 5.11 (s, 1H, 5H); EI-MS m/z (relative intensity) 188 (M$^+$, 100); IR (KBr pellet) 3374 (s), 3346 (s), 3173 (s), 3061 (w), 1660 (vs), 1639 (vs), 1594 (vs), 1570 (s), 1564 (s), 1472 (s), 1441 (m), 1316 (m), 1294 (m), 1242 (m), 1152 (w), 1084 (w), 998 (m), 985 (m), 817 (m), 804 (m), 752 (m), 698 (w), 655 (m), 613 (m). Anal. Calcd for C$_9$H$_8$N$_4$O: C, 57.44; H, 4.28; N, 29.77. Found: C, 57.49; H, 4.19; N, 29.84.

6-Amino-5-methyl-2-(2'-pyridyl)-4(3*H*)-pyrimidinone (HL4) was similarly prepared from 2-cyanopropionic acid (7.04 g, 55.3 mmol) and 2-pyridinecarboximidamide hydrochloride (7.89 g, 50.0 mmol) according to the procedure described for the synthesis of HL3. Recrystallization from ethanol afforded 4.45 g (44 %) of light yellow green crystals: mp 248–250 °C; ^{1}H NMR (270 MHz, DMSO-d_6) δ 10.85 (s, 1H, NH), 8.70 (ddd, 1H, J = 4.8, 1.7, 0.9 Hz, 2-pyrigyl-6'H), 8.22 (ddd, 1H, J = 7.8, 1.1, 0.9 Hz, 2-pyrigyl-3'H), 8.03 (ddd, 1H, J = 7.8, 7.7, 1.7 Hz, 2-pyrigyl-4'H), 7.60 (ddd, 1H, J = 7.7, 4.8, 1.1 Hz, 2-pyrigyl-5'H), 6.33 (s, 2H, NH$_2$), 1.81 (s, 3H, Me); EI-MS m/z (relative intensity) 202 (M$^+$, 100); IR (KBr pellet) 3364 (m), 3262 (s), 3202 (s), 3076 (w), 2914 (w), 1661 (m), 1614 (vs), 1566 (s), 1553 (s), 1479 (w), 1456 (w), 1422 (s), 1365 (w), 1288 (w), 1202 (m), 998 (m), 805 (w), 768 (m), 746 (w), 738 (w), 671 (m), 622 (m). Anal. Calcd for C$_{10}$H$_{10}$N$_4$O: C, 59.40; H, 4.98; N, 27.71. Found: C, 59.45; H, 4.88; N, 27.67.

[{Cu(L1)}$_2$]PF$_6$ (1). A solution of [Cu(MeCN)$_4$]PF$_6$ (372.7 mg, 1.00 mmol) and NH$_4$PF$_6$ (167.9 mg, 1.03 mmol) in 120 mL of methanol was treated with oxygen gas with vigorously stirring. After the oxidation of copper(I) to copper(II), the copper(II) solution was added to [Cu(MeCN)$_4$]PF$_6$ (372.6 mg, 1.00 mmol). To this mixture of copper(I)

and copper(II) was added a solution of HL1 (347.2 mg, 2.00 mmol) in 120 mL of methanol. The resulting dark grayish red solution was allowed to stand for three weeks, and the black crystals thus produced were collected by suction filtration, washed with methanol, and dried *in vaccuo* (374 mg, 61 %): IR (KBr pellet) 3438 (br), 3078 (w), 1592 (vs), 1570 (m), 1530 (m) , 1495 (s), 1471(s), 1448 (m), 1369 (s), 1286 (m), 1243 (w), 1106 (w), 1016 (s), 954 (w), 850 (vs), 833 (s), 770 (m), 762 (m), 678 (m), 624 (m), 558 (s). Anal. Calcd for $C_{18}H_{12}Cu_2F_6N_6O_2P$: C, 35.07; H, 1.96; N, 13.63. Found: C, 35.10; H, 1.92; N, 13.63.

[{Cu(L2)}₂]PF₆ (2) was prepared from HL2 (74.9 mg, 0.400 mmol), [Cu(MeCN)₄]PF₆ (75.1 mg, 0.201 mmol) and Cu(PF₆)₂ (which was obtained from a treatment of [Cu(MeCN)₄]PF₆ (75.9 mg, 0.204 mmol) and NH₄PF₆ (37.4 mg, 0.229 mmol) with oxygen gas) in 140 mL of ethanol in 24 % yield according to the procedure described for the synthesis of **1**: IR (KBr pellet) 3446 (br), 3086 (w), 1610 (s), 1595 (vs), 1492 (s) , 1474 (s), 1449 (m), 1369 (s), 1292 (m), 1208 (m), 1165 (w), 1100 (w), 1027 (m), 986 (w), 842 (vs), 764 (s), 693 (w), 684 (w), 654 (m), 622 (w), 592 (w), 558 (s). Anal. Calcd for $C_{20}H_{16}Cu_2F_6N_6O_2P$: C, 37.28; H, 2.50; N, 13.04. Found: C, 37.11; H, 2.59; N, 12.86

[{Cu(L3)}₂]PF₆·DMF (3) was prepared from HL3 (301 mg, 1.60 mmol), [Cu(MeCN)₄]PF₆ (298 mg, 0.806 mmol) and Cu(PF₆)₂ (which was obtained from a treatment of [Cu(MeCN)₄]PF₆ (295 mg, 0.792 mmol) and NH₄PF₆ (131 mg, 0.806 mmol) with oxygen gas) in a mixture of 300 mL of methanol and 150 mL of *N,N*-dimethylformamide in 19 % yield according to the procedure described for the synthesis of **1**: IR (KBr pellet) 3450 (s), 3354 (s), 3246 (m), 3104 (w), 2944 (vw), 1662 (s), 1612 (s), 1581 (vs), 1568 (vs), 1490 (s), 1468 (m), 1443 (m), 1392 (m), 1376 (m), 1307 (m), 1293 (m), 1270 (m), 1241 (m), 1027 (m), 844 (vs), 806 (m), 756 (m), 558 (m). Anal. Calcd for $C_{21}H_{21}Cu_2F_6N_9O_3P$: C, 35.06; H, 2.94; N, 17.52. Found: C, 35.08; H, 2.94; N, 17.40.

[{Cu(L4)}₂]PF₆·0.5MeOH (4) was prepared from HL4 (162.4 mg, 0.803 mmol), [Cu(MeCN)₄]PF₆ (150.7 mg, 0.404 mmol) and

Cu(PF$_6$)$_2$ (which was obtained from a treatment of [Cu(MeCN)$_4$]PF$_6$ (149.5 mg, 0.401 mmol) and NH$_4$PF$_6$ (78.8 mg, 0.483 mmol) with oxygen gas) in a mixture of 200 mL of methanol and 70 mL of N,N-dimethylformamide in 30 % yield according to the procedure described for the synthesis of **1**: IR (KBr pellet) 3490 (m), 3423 (m), 3232 (m), 3107 (vw), 2916 (vw), 1622 (s), 1586 (vs), 1569 (s), 1490 (s), 1459 (m), 1430 (s), 1385 (s), 1316 (w), 1295 (m), 1271 (w), 1164 (m), 1049 (w), 1024 (m), 854 (vs), 821 (s), 773 (s), 697 (w), 678 (w), 559 (s). Anal. Calcd for C$_{20.5}$H$_{20}$Cu$_2$F$_6$N$_8$O$_{2.5}$P: C, 35.66; H, 2.92; N, 16.23. Found: C, 35.72; H, 2.91; N, 16.14.

2. 2. 4 Crystallographic Studies: X-ray Data Collection.

[{Cu(L1)}$_2$]PF$_6$ (1) and [{Cu(L4)}$_2$]PF$_6$·0.5MeOH (4). A black prismatic crystal of **1** with dimensions of 0.20 x 0.20 x 0.30 mm and a black plate crystal of **4** with dimensions of 0.50 x 0.40 x 0.15 mm were mounted on a glass fiber with epoxy resin, respectively. All measurements were made on a Rigaku AFC7R or AFC5R diffractometer with graphite monochromated Mo Kα radiation (50 kV, 180 mA for **1** and 50 kV, 250 mA for **4**). Accurate cell dimensions and crystal orientation matrices were determined by a least-squares refinement using the setting angles of 24 (**1**) and 25 (**4**) carefully centered reflections in the ranges 21.00 < 2θ < 30.10° (**1**) and 27.28 < 2θ < 27.48° (**4**). The data were collected at a temperature of 296 K using the ω–2θ scan technique to a maximum 2θ value of 60.0° for **1** and 55.0° for **4**, respectively. Omega scans of several intense reflections, made prior to data collection, had an average width at half-height of 0.37° (**1**) and 0.23° (**4**) with a take-off angle of 6.0°. Scans of (1.15 + 0.35 tanθ)° (**1**) and (1.42 + 0.35 tanθ)° (**4**) were made at a speed of 16.0°/min (in ω) (**1**) and 10.0°/min (in ω) (**4**). The weak reflections ($|F_o|$ < 10σ(F_o)) were rescanned (maximum of 5 (**1**) and 3 (**4**) scans) and the counts were accumulated to ensure good counting statistics. Stationary background counts were recorded on each side of the reflection. The ratio of peak counting time to background counting time was 2:1. The diameter of the incident beam collimator was 1.0 mm, the crystal to detector distance was 235 mm, and the detector

apertures were set to 9.0 x 13.0 mm (horizontal x vertical) for **1** and 6.0 x 6.0 mm (horizontal x vertical) for **4**.

Of the 6309 (**1**) and 11702 (**4**) reflections which were collected, 3233 (**1**) and 11269 (**4**) were unique. The intensities of three representative reflection were measured after every 150 reflections. Over the course of data collection, the standard reflections were monitored and the decay corrections were applied by a polynominal correction. An empirical absorption correction based on azimuthal scans of several reflections was applied. The data were corrected for Lorentz and polarization effects.

[{Cu(L3)}₂]PF₆·DMF (3). A black plate crystal of **3** having approximate dimensions of 0.20 x 0.10 x 0.05 mm was mounted on a glass fiber with epoxy resin. All measurements were made on a Rigaku RAXIS CS imaging plate area detector with graphite monochromated Mo Kα radiation. (50 kV, 250 mA). Indexing was performed from 3 stills which were exposed for 5.0 minutes. The crystal-to-detector distance was 143 mm. The detector swing angle was 0.03°. Readout was performed in the 0.1 mm pixel mode. Cell constants and an orientation matrix for data collection corresponded to a primitive triclinic cell with dimensions: $a =$ 10.564(3) Å, $b = 14.936(4)$ Å, $c = 8.218(4)$ Å, $\alpha = 92.75(4)°$, $\beta =$ 91.15(4)°, $\gamma = 87.20(2)°$, $V = 1293.5(7)$ Å^3. Based on a statistical analysis of intensity distribution, and the successful solution and refinement of the structure, the space group was determined to be $P\bar{1}$. The data were collected at a temperature of 273 K to a maximum 2θ value of 60.1°. The oscillation range was 10°, and a total of 18 images were collected, each being exposed for 30 minutes. The crystal to detector distance was 143 mm. The detector swing angle was 0.03°. Readout was performed in the 0.1 mm pixel mode. A total of 3342 unique reflections were obtained, of which 3333 with $|Fo| > 3\sigma(Fo)$ were used for the structure analysis. The linear absorption coefficient, μ, for Mo Kα radiation is 17.9 cm^{-1}. The data were corrected for Lorentz and polarization effects.

Structure Solution and Refinement.

The structure was solved by direct methods[30c] for **1** and **3** and by heavy-atom Patterson methods[30a] for **4** and expanded using Fourier techniques.[32] The non-hydrogen atoms of **1** and **3** were refined anisotropically. The non-hydrogen atoms for the complex cations and PF_6 anions in **4** were refined anisotropically, while those of methanol were refined isotropically. The oxygen atom of methanol is disordered and was refined over two position with site occupancies of 50%. All the hydrogen atoms for **1** were located in the Fourier difference maps and refined isotropically. All the hydrogen atoms for **3** were placed in the calculated positions and the hydrogen atoms of the complex cation were refined isotropically, the rest were included in fixed positions. All the hydrogen atoms of the complex cations in **4** were placed in the calculated positions and refined isotropically.

All least-square refinements in these analyses were carried out on F, the function minimized being $\Sigma w(|F_o| - |F_c|)^2$ with a weighting scheme $w = 4F_o^2/\sigma^2(F_o^2)$ for **1** and $w = [\sigma_c^2(F_o) + (p^2/4)F_o^2]^{-1}$ for **3** and **4**, respectively. The usual agreement factor are $R = \Sigma||F_o| - |F_c||/\Sigma|F_o|$ and $R_w = [\Sigma w(|F_o| - |F_c|)^2/\Sigma w|F_o|^2]^{1/2}$. The goodness of fit are $S = [\Sigma w(|F_o|^2 - |F_c|^2)^2/(N_o - N_v)]^{1/2}$, where N_o is the number of reflections and N_v is the number of refined parameters. The final cycle of full-matrix least-squares refinement was based on 2025(**1**), 3333 (**3**) and 6243 (**4**) observed reflections ($F_o > 3.00\sigma(F_o)$) and 184 (**1**), 435 (**3**) and 859 (**4**) variable parameters and converged with unweighted and weighted agreement factors $R = 0.037$ (**1**), 0.075 (**3**) and 0.057 (**4**) and $R_w = 0.039$ (**1**), 0.065 (**3**) and 0.035 (**4**), respectively. The values of S were 1.66 (**1**), 3.41 (**3**) and 2.10 (**4**), respectively. The weighting scheme was based on counting statistics and included a factor ($p = 0.015$ (**1**), 0.015 (**3**) and 0.005 (**4**)) to downweight the intense reflections. Plots of $\Sigma w(|F_o| - |F_c|)^2$ versus $|F_o|$, reflection order in data collection, $\sin\theta/\lambda$ and various classes of indices showed no unusual trends. The maximum and minimum peaks on the final difference Fourier map corresponded to 0.65 and -0.35 eÅ^{-3} for **1**, 0.68 and -1.27 eÅ^{-3} for **3**, 1.00 and -0.60 eÅ^{-3} for **4**, respectively.

51

Neutral atom scattering factors were taken from Cromer and Waber.[26] Anomalous dispersion effects were included in F_c[27]; the values for $\Delta f'$ and $\Delta f''$ were those of Creagh and McAuley[28]. The values for the mass attenuation coefficients are those of Creagh and Hubbel.[29] All calculations were performed using the teXsan[31] crystallographic software package of Molecular Structure Corporation.

Crystal data for the complexes **1**, **3**, and **4** are summarized in Table 2. The fractional atomic coordinates and equivalent isotropic displacement parameters for **1**, **3**, and **4** are listed in Tables 3–5.

Table 2. Crystal Data and Structure Determination for **1**, **3**, and **4**

	1	3	4
formula	$C_{18}H_{12}Cu_2F_6N_6O_2P$	$C_{21}H_{21}Cu_2F_6N_9O_3P$	$C_{20.5}H_{20}Cu_2F_6N_8O_{2.5}P$
fw	616.39	719.51	690.49
color	black	black	black
cryst dimens, mm	0.20 x 0.20 x 0.30	0.20 x 0.10 x 0.05	0.50 x 0.40 x 0.15
a, Å	14.565(2)	10.564(3)	14.895(2)
b, Å	8.863(1)	14.936(4)	14.908(2)
c, Å	8.0630(7)	8.218(4)	13.689(2)
α, deg		92.75(4)	114.761(10)
β, deg	90.42(1)	91.15(4)	99.61(1)
γ, deg		87.20(2)	108.60(1)
V, Å^3	1040.8(2)	1293.5(7)	2451.3(8)
Z	2	2	4
crystal system	monoclinic	triclinic	triclinic
space group	$P2_1/n$	$P\bar{1}$	$P\bar{1}$
ρ_{calc}, g cm^{-1}	1.967	1.847	1.871
$F(000)$	610.00	722.00	1384.00
μ,cm^{-1}	22.05	17.95	18.87
diffractomrter	Rigaku AFC7R	Rigaku AXICS CS	Rigaku AFC5R
radiation (λ, Å)	0.71069 (graphite monochromated)	0.71070 (graphite monochromated)	0.71069 (graphite monochromated)
temp, K	296	273	296
no. of reflcns collcd	6309	3342	11702
no. of unique data	3233	3342	11269
no. of obsd reflcns	2025 ($|F_o| > 3\sigma(F_o)$)	3333 ($|F_o| > 3\sigma(F_o)$)	6243 ($|F_o| > 3\sigma(F_o)$)
no. of variables	184	435	859
R^a	0.037	0.075	0.057
$R_w{}^b$	0.039	0.065	0.035
S, goodness of fit^c	1.66	3.41	2.10
final max/min $\Delta\rho$, e Å^{-3}	0.65/–0.35	0.68/–1.27	1.00/–0.60

^{a} $R = \Sigma||F_o| - |F_c||/\Sigma|F_o|$. ^{b} $R_w = \{(\Sigma w(|F_o| - |F_c|)^2/\Sigma w|F_o|^2)\}^{1/2}$. ^{c} $S = \{\Sigma w(|F_o| - |F_c|)^2/(N_o - N_v)\}^{1/2}$.

Table 3. Fractional Atomic Coordinates and Equivalent Isotropic Displacement Parameters (Å) with Esd's in Parentheses for [{Cu(L1)}$_2$]PF$_6$ (**1**)

atom	x	y	z	$B_{eq},^a$ Å^2
Cu	0.04242(3)	0.11016(5)	0.45974(5)	2.529(8)
P	0	0	0	3.66(3)
F(1)	−0.0854(2)	0.1012(4)	0.0414(4)	7.8(1)
F(2)	0.0180(3)	0.0858(4)	−0.1659(4)	9.8(1)
F(3)	0.0611(3)	0.1120(5)	0.0981(5)	11.0(1)
O(14)	−0.1540(2)	−0.0135(3)	0.4961(3)	3.04(5)
N(11)	−0.1476(2)	0.4059(4)	0.2921(4)	3.82(8)
N(13)	−0.0744(2)	0.1936(3)	0.4140(3)	2.47(6)
N(21)	0.0874(2)	0.3172(3)	0.3840(3)	2.80(6)
C(12)	−0.0740(3)	0.3318(4)	0.3422(4)	2.84(7)
C(14)	−0.1551(2)	0.1201(4)	0.4360(4)	2.73(7)
C(15)	−0.2357(3)	0.1953(5)	0.3883(5)	3.6(1)
C(16)	−0.2284(3)	0.3339(5)	0.3198(6)	4.2(1)
C(22)	0.0175(3)	0.3989(4)	0.3207(4)	2.88(7)
C(23)	0.0327(3)	0.5345(5)	0.2420(5)	3.8(1)
C(24)	0.1212(4)	0.5865(5)	0.2275(6)	4.9(1)
C(25)	0.1922(3)	0.5048(5)	0.2937(6)	4.3(1)
C(26)	0.1729(3)	0.3690(5)	0.3718(5)	3.57(9)
H(15)	−0.287(2)	0.156(4)	0.407(4)	3.0(8)
H(16)	−0.275(3)	0.381(5)	0.287(5)	5(1)
H(23)	−0.014(3)	0.586(4)	0.197(5)	4(1)
H(24)	0.135(3)	0.669(5)	0.178(5)	5(1)
H(25)	0.251(3)	0.535(5)	0.283(5)	5(1)
H(26)	0.214(3)	0.310(4)	0.423(5)	4(1)

$^a B_{eq} = (8/3\pi^2)(U_{11}(aa^*)^2 + U_{22}(bb^*)^2 + U_{33}(cc^*)^2 + 2U_{12}aa^*bb^*\cos\gamma + 2U_{13}aa^*cc^*\cos\beta + 2U_{23}bb^*cc^*\cos\alpha)$

Table 4. Fractional Atomic Coordinates and Equivalent Isotropic Displacement Parameters (Å) with Esd's in Parentheses for [{Cu(L3)}$_2$]PF$_6$·DMF (**3**)

atom	x	y	z	$B_{eq},^a$ Å^2
Cu(1)	0.21156(9)	0.06526(7)	0.4423(1)	2.79(3)
Cu(2)	0.28462(9)	−0.07631(7)	0.5456(1)	2.83(3)
P(1)	0.2414(3)	0.4003(2)	0.8024(4)	5.41(8)
F(1)	0.3503(8)	0.4531(5)	0.890(1)	11.2(3)
F(2)	0.1845(10)	0.4882(6)	0.737(1)	14.1(4)
F(3)	0.1419(7)	0.3453(5)	0.709(1)	11.2(3)
F(4)	0.160(1)	0.4172(8)	0.946(1)	18.2(5)
F(5)	0.300(1)	0.3125(5)	0.868(1)	14.8(4)
F(6)	0.3269(9)	0.3845(7)	0.651(1)	13.9(4)

53

O(14)	0.1514(5)	–0.1335(3)	0.4412(7)	3.3(1)
O(34)	0.3432(5)	0.1229(3)	0.5530(6)	3.0(1)
O(51)	0.7357(8)	0.2841(5)	0.886(1)	7.2(2)
N(11)	–0.0987(6)	0.0113(4)	0.1598(8)	3.0(2)
N(13)	0.0852(6)	–0.0018(4)	0.3333(7)	2.6(2)
N(16)	–0.2074(6)	–0.1163(5)	0.0866(9)	3.2(2)
N(21)	0.1173(6)	0.1684(4)	0.3329(8)	3.1(2)
N(31)	0.5888(6)	–0.0249(4)	0.8364(8)	2.9(2)
N(33)	0.4101(6)	–0.0115(4)	0.6569(8)	2.8(2)
N(36)	0.6932(7)	0.1017(5)	0.9221(9)	3.7(2)
N(41)	0.3741(6)	–0.1803(4)	0.6547(8)	3.0(2)
N(51)	0.7296(9)	0.4040(5)	0.729(1)	5.3(2)
C(12)	–0.0009(7)	0.0452(5)	0.2428(9)	2.6(2)
C(14)	0.0715(8)	–0.0915(5)	0.3487(9)	2.8(2)
C(15)	–0.0297(8)	–0.1316(5)	0.2688(10)	3.2(2)
C(16)	–0.1118(8)	–0.0801(5)	0.1727(9)	2.9(2)
C(22)	0.0176(8)	0.1426(5)	0.2428(9)	2.8(2)
C(23)	–0.0591(9)	0.2031(6)	0.159(1)	3.7(2)
C(24)	–0.0312(9)	0.2930(6)	0.173(1)	4.5(3)
C(25)	0.0669(10)	0.3209(6)	0.270(1)	4.9(3)
C(26)	0.1417(8)	0.2562(6)	0.345(1)	3.7(2)
C(32)	0.4953(7)	–0.0577(5)	0.7498(9)	2.5(2)
C(34)	0.4237(7)	0.0790(5)	0.6454(9)	2.7(2)
C(35)	0.5223(8)	0.1193(5)	0.7329(9)	3.0(2)
C(36)	0.6004(7)	0.0657(5)	0.8297(10)	3.0(2)
C(42)	0.4721(8)	–0.1560(5)	0.7498(10)	3.0(2)
C(43)	0.5434(9)	–0.2178(6)	0.833(1)	4.0(2)
C(44)	0.511(1)	–0.3066(6)	0.826(1)	5.3(3)
C(45)	0.4094(10)	–0.3308(6)	0.730(1)	4.8(3)
C(46)	0.3426(10)	–0.2670(6)	0.647(1)	4.1(2)
C(51)	0.651(2)	0.477(1)	0.676(2)	10.8(6)
C(52)	0.856(1)	0.402(1)	0.688(3)	14.2(7)
C(53)	0.690(2)	0.3459(10)	0.821(2)	9.4(5)
H(11)	–0.261(7)	–0.085(5)	0.018(9)	3(1)
H(12)	–0.219(8)	–0.179(5)	0.095(9)	5(1)
H(15)	–0.037(8)	–0.196(5)	0.279(9)	3(1)
H(23)	–0.129(8)	0.184(5)	0.086(10)	4(1)
H(24)	–0.085(8)	0.334(5)	0.12(1)	4(1)
H(25)	0.084(8)	0.382(6)	0.28(1)	6(2)
H(26)	0.210(7)	0.270(5)	0.407(9)	2(1)
H(31)	0.748(8)	0.066(5)	0.979(10)	3(1)
H(32)	0.707(8)	0.163(5)	0.918(9)	3(1)
H(35)	0.534(7)	0.182(5)	0.729(9)	2(1)
H(43)	0.614(8)	–0.199(5)	0.894(10)	4(1)
H(44)	0.559(8)	–0.351(6)	0.88(1)	5(2)
H(45)	0.383(8)	–0.389(6)	0.724(10)	5(1)
H(46)	0.274(8)	–0.284(5)	0.58(1)	5(2)
H(51)	0.6208	0.5146	0.7719	11.2392
H(52)	0.6923	0.5169	0.6092	11.2392
H(53)	0.5758	0.4583	0.6200	11.2392

atom	x	y	z	$B_{eq},^a$ Å^2
H(54)	0.8825	0.3485	0.6271	13.8541
H(55)	0.8727	0.4519	0.6136	13.8541
H(56)	0.9107	0.4109	0.7785	13.8541
H(57)	0.6006	0.3582	0.8380	11.7686

$^a B_{eq} = (8/3\pi^2)(U_{11}(aa^*)^2 + U_{22}(bb^*)^2 + U_{33}(cc^*)^2 + 2U_{12}aa^*bb^*\cos\gamma + 2U_{13}aa^*cc^*\cos\beta + 2U_{23}bb^*cc^*\cos\alpha)$

Table 5. Fractional Atomic Coordinates and Equivalent Isotropic Displacement Parameters (Å) with Esd's in Parentheses for [{Cu(L4)}$_2$]PF$_6$·0.5MeOH (**4**)

atom	x	y	z	$B_{eq},^a$ Å^2
Cu(1)	0.14261(6)	0.45792(7)	0.08197(7)	2.91(2)
Cu(2)	0.22912(6)	0.61776(7)	0.07133(7)	2.93(2)
Cu(3)	0.34373(6)	0.46552(6)	0.01087(7)	2.99(2)
Cu(4)	0.27092(6)	0.46285(6)	−0.16078(7)	3.13(2)
P(1)	0.7599(2)	0.1993(2)	0.2988(2)	3.99(5)
P(2)	0.2508(2)	0.1928(2)	0.2934(2)	4.20(5)
F(11)	0.6834(4)	0.2468(4)	0.2814(4)	7.8(2)
F(12)	0.6969(4)	0.0960(3)	0.1737(3)	7.9(1)
F(13)	0.8352(4)	0.1494(4)	0.3150(4)	8.0(2)
F(14)	0.8251(4)	0.2612(4)	0.2496(4)	8.5(2)
F(15)	0.6949(4)	0.1374(4)	0.3488(4)	7.8(1)
F(16)	0.8228(3)	0.3028(3)	0.4236(3)	6.6(1)
F(21)	0.2547(4)	0.2094(4)	0.4152(4)	8.0(2)
F(22)	0.1330(3)	0.1266(4)	0.2459(4)	8.5(2)
F(23)	0.2467(4)	0.1770(4)	0.1736(4)	8.9(2)
F(24)	0.2413(4)	0.3021(4)	0.3265(4)	8.3(2)
F(25)	0.2633(4)	0.0861(4)	0.2641(4)	8.3(2)
F(26)	0.3691(3)	0.2596(4)	0.3412(4)	8.1(2)
O(14)	0.1361(3)	0.5576(3)	−0.0742(3)	3.1(1)
O(34)	0.2352(3)	0.5163(4)	0.2265(4)	3.2(1)
O(54)	0.3735(4)	0.5992(4)	−0.1114(4)	3.7(1)
O(74)	0.2389(3)	0.3309(3)	−0.0363(4)	3.2(1)
O(91)	0.323(1)	−0.022(1)	0.473(1)	7.3(4)
O(92)	0.267(1)	−0.013(2)	0.446(2)	13.7(6)
N(11)	−0.1061(4)	0.2645(4)	−0.2055(5)	2.9(1)
N(13)	0.0475(4)	0.4089(4)	−0.0615(4)	2.5(1)
N(16)	−0.1702(5)	0.2644(5)	−0.3692(5)	3.7(2)
N(21)	0.0440(4)	0.3160(4)	0.0618(5)	2.7(1)
N(31)	0.4569(4)	0.8266(4)	0.3749(5)	3.7(2)
N(33)	0.3160(4)	0.6711(4)	0.2197(4)	2.9(1)
N(36)	0.5232(5)	0.8263(6)	0.5396(6)	5.2(2)
N(41)	0.3184(4)	0.7669(4)	0.0986(5)	3.3(1)
N(51)	0.6045(4)	0.7423(4)	0.1878(5)	3.5(1)
N(53)	0.4484(4)	0.5987(4)	0.0464(5)	2.8(1)

N(56)	0.6842(5)	0.8926(6)	0.1718(7)	5.3(2)
N(61)	0.4340(4)	0.4910(4)	0.1570(5)	3.0(1)
N(71)	0.0513(4)	0.1535(4)	−0.3699(4)	3.6(1)
N(73)	0.1788(4)	0.3184(4)	−0.2086(5)	2.6(1)
N(76)	−0.0193(6)	−0.0004(5)	−0.3572(6)	6.2(2)
N(81)	0.1950(4)	0.4229(4)	−0.3204(5)	3.0(1)
C(12)	−0.0348(5)	0.3124(5)	−0.1077(6)	2.5(2)
C(14)	0.0564(5)	0.4662(5)	−0.1193(5)	2.5(2)
C(15)	−0.0204(5)	0.4208(5)	−0.2244(5)	2.5(2)
C(16)	−0.0968(5)	0.3187(5)	−0.2646(6)	2.7(2)
C(17)	−0.0154(7)	0.4804(8)	−0.2901(8)	4.0(2)
C(22)	−0.0364(5)	0.2595(5)	−0.0371(6)	2.5(2)
C(23)	−0.1112(5)	0.1604(6)	−0.0678(6)	3.2(2)
C(24)	−0.1060(6)	0.1167(6)	0.0018(7)	4.1(2)
C(25)	−0.0259(6)	0.1751(6)	0.1033(7)	4.2(2)
C(26)	0.0483(6)	0.2730(6)	0.1292(6)	3.5(2)
C(32)	0.3890(5)	0.7739(6)	0.2725(6)	3.0(2)
C(34)	0.3068(5)	0.6146(6)	0.2786(6)	2.9(2)
C(35)	0.3756(5)	0.6648(6)	0.3886(6)	3.0(2)
C(36)	0.4496(5)	0.7692(6)	0.4320(6)	3.6(2)
C(37)	0.3665(8)	0.6076(8)	0.4571(8)	4.7(3)
C(42)	0.3893(5)	0.8290(6)	0.2048(6)	3.0(2)
C(43)	0.4563(6)	0.9366(6)	0.2447(7)	4.2(2)
C(44)	0.4484(6)	0.9811(6)	0.1742(7)	4.7(2)
C(45)	0.3774(6)	0.9173(7)	0.0670(7)	4.5(2)
C(46)	0.3141(6)	0.8104(6)	0.0325(7)	3.5(2)
C(52)	0.5268(5)	0.6480(6)	0.1455(6)	3.0(2)
C(54)	0.4480(5)	0.6479(5)	−0.0192(6)	3.1(2)
C(55)	0.5296(5)	0.7471(6)	0.0185(6)	3.2(2)
C(56)	0.6037(5)	0.7924(6)	0.1243(7)	3.8(2)
C(57)	0.5359(8)	0.8035(8)	−0.0512(9)	5.1(3)
C(62)	0.5196(5)	0.5872(6)	0.2075(6)	3.2(2)
C(63)	0.5920(5)	0.6244(6)	0.3124(6)	3.5(2)
C(64)	0.5780(6)	0.5600(7)	0.3615(7)	4.2(2)
C(65)	0.4927(6)	0.4619(6)	0.3081(7)	4.4(2)
C(66)	0.4224(6)	0.4318(6)	0.2073(6)	3.5(2)
C(72)	0.1153(5)	0.2571(5)	−0.3182(6)	2.6(2)
C(74)	0.1774(5)	0.2706(5)	−0.1407(6)	2.5(2)
C(75)	0.1088(5)	0.1611(5)	−0.1886(6)	2.7(2)
C(76)	0.0485(5)	0.1068(5)	−0.3014(6)	3.3(2)
C(77)	0.1044(7)	0.1036(7)	−0.1204(7)	3.7(2)
C(82)	0.1214(5)	0.3178(5)	−0.3816(6)	2.8(2)
C(83)	0.0583(6)	0.2747(6)	−0.4907(6)	3.4(2)
C(84)	0.0686(7)	0.3400(7)	−0.5410(7)	4.3(2)
C(85)	0.1441(6)	0.4453(7)	−0.4793(7)	4.1(2)
C(86)	0.2039(6)	0.4836(6)	−0.3706(7)	4.0(2)
C(91)	0.2567(8)	0.0258(8)	0.5260(9)	9.1(3)
H(11)	−0.220(4)	0.193(5)	−0.395(5)	3(1)
H(12)	−0.168(4)	0.295(5)	−0.418(5)	4(1)
H(13)	−0.065(5)	0.448(5)	−0.354(6)	5(1)

H(14)	0.039(5)	0.499(5)	−0.308(5)	5(1)
H(15)	−0.016(5)	0.547(5)	−0.250(5)	5(1)
H(23)	−0.165(4)	0.123(4)	−0.139(5)	2(1)
H(24)	−0.159(4)	0.047(5)	−0.018(5)	4(1)
H(25)	−0.019(4)	0.148(5)	0.158(5)	4(1)
H(26)	0.106(4)	0.315(4)	0.198(5)	3(1)
H(31)	0.574(5)	0.897(5)	0.561(6)	5(1)
H(32)	0.526(5)	0.789(6)	0.583(6)	6(1)
H(33)	0.414(5)	0.645(6)	0.526(6)	6(1)
H(34)	0.306(5)	0.587(6)	0.467(6)	7(1)
H(35)	0.367(5)	0.536(6)	0.419(6)	6(1)
H(43)	0.504(4)	0.976(5)	0.320(5)	4(1)
H(44)	0.490(5)	1.057(5)	0.199(5)	5(1)
H(45)	0.368(4)	0.942(5)	0.011(5)	4(1)
H(46)	0.264(4)	0.764(5)	−0.044(5)	3(1)
H(51)	0.723(5)	0.914(6)	0.245(6)	6(1)
H(52)	0.687(6)	0.939(6)	0.140(6)	6(1)
H(53)	0.593(5)	0.864(6)	−0.019(6)	7(1)
H(54)	0.538(5)	0.763(6)	−0.124(6)	6(1)
H(55)	0.483(5)	0.825(6)	−0.059(6)	7(1)
H(63)	0.652(4)	0.695(5)	0.349(5)	3(1)
H(64)	0.626(5)	0.582(5)	0.435(5)	5(1)
H(65)	0.480(5)	0.411(5)	0.339(5)	4(1)
H(66)	0.362(4)	0.365(5)	0.170(5)	3(1)
H(71)	−0.062(5)	−0.035(6)	−0.438(6)	8(1)
H(72)	−0.027(5)	−0.039(6)	−0.317(6)	7(1)
H(73)	0.121(4)	0.043(5)	−0.151(5)	3(1)
H(74)	0.152(4)	0.153(5)	−0.044(5)	3(1)
H(75)	0.040(4)	0.076(5)	−0.113(5)	4(1)
H(83)	0.006(4)	0.202(4)	−0.531(5)	2(1)
H(84)	0.024(4)	0.313(5)	−0.619(5)	4(1)
H(85)	0.154(4)	0.493(5)	−0.510(5)	3(1)
H(86)	0.254(4)	0.556(5)	−0.324(5)	3(1)

$^a B_{eq} = (8/3\pi^2)(U_{11}(aa^*)^2 + U_{22}(bb^*)^2 + U_{33}(cc^*)^2 + 2U_{12}aa^*bb^*\cos\gamma + 2U_{13}aa^*cc^*\cos\beta + 2U_{23}bb^*cc^*\cos\alpha)$

2. 3 Results and Discussion

2. 3. 1 Molecular and Crystal Structures.

[{Cu(L1)}2]PF6 (1). ORTEP diagram of the complex cation in **1** is shown in Figure 4. Bond distances and angles are given in Tables 6 and 7. Complex **1** was crystallized in the monoclinic $P2_1/n$ space group with two complex cations and two PF_6 anions in the unit cell. The cation is essentially planar structure with an inversion center at the midpoint of two copper atoms. The maximum deviations from the mean plane of the cation are 0.238(5) Å of C(24) atom and –0.238(5) Å of C(24') atom. The two copper atoms are bridged by the N(13) and O(14) atoms of (L1)⁻ ligand and the remaining site are occupied by the N(21) atom of that ligand. The Cu–Cu distance is 2.4028(8) Å, which is short enough to suggest the possibility of some overlap of metal orbitals. This is the first example of the planar mixed-valence dicopper(II,I) complex in which both copper sites have equal coordination geometry.
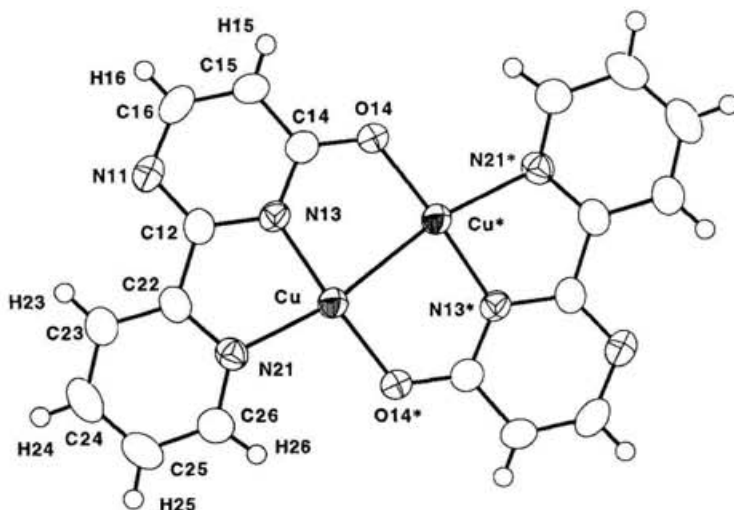
Figure 4. ORTEP diagram of [{Cu(L1)}2]⁺ cation in **1**, showing the labeling scheme and 50 % thermal ellipsoids.

Table 6. Bond Distances (Å) with Esd's in Parentheses for [{Cu(L1)}2]PF6 (**1**)

Cu–Cu'	2.4028(8)	Cu–O(14)	1.869(2)
Cu–N(13)	1.890(3)	Cu–N(21)	2.043(3)

58

P–F(1)	1.572(3)	P–F(2)	1.563(3)
P–F(3)	1.548(3)	O(14)–C(14)	1.279(4)
N(11)–C(12)	1.317(4)	N(11)–C(16)	1.358(5)
N(13)–C(12)	1.355(4)	N(13)–C(14)	1.356(4)
N(21)–C(22)	1.346(4)	N(21)–C(26)	1.332(5)
C(12)–C(22)	1.471(5)	C(14)–C(15)	1.401(5)
C(15)–C(16)	1.351(6)	C(22)–C(23)	1.378(5)
C(23)–C(24)	1.375(6)	C(24)–C(25)	1.368(7)
C(25)–C(26)	1.388(6)		

[a] Single prime as superscript refers to the following equivalent positions relative to the x, y, z set: (') –x, –y, 1–z.

Table 7. Bond Angles (deg) with Esd's in Parentheses for [{Cu(L1)}$_2$]PF$_6$ (**1**)[a]

Cu'–Cu–O(14')	91.38(8)	Cu'–Cu–N(13)	84.65(9)
Cu'–Cu–N(21)	167.74(9)	O(14')–Cu–N(13)	175.8(1)
O(14')–Cu–N(21)	100.9(1)	N(13)–Cu–N(21)	83.1(1)
Cu'–O(14)–C(14)	120.3(2)	Cu–N(13)–C(12)	115.5(2)
Cu–N(13)–C(14)	124.5(2)	Cu–N(21)–C(22)	110.7(2)
Cu–N(21)–C(26)	129.3(3)	F(1)–P–F(1")	180.0
F(1)–P–F(2)	92.4(2)	F(1)–P–F(2")	87.6(2)
F(1)–P–F(3)	88.8(2)	F(1)–P–F(3")	91.2(2)
F(1")–P–F(2)	87.6(2)	F(1")–P–F(2")	92.4(2)
F(1")–P–F(3)	91.2(2)	F(1")–P–F(3")	88.8(2)
F(2)–P–F(2")	180.0	F(2)–P–F(3)	91.5(2)
F(2)–P–F(3")	88.5(2)	F(2")–P–F(3)	88.5(2)
F(2")–P–F(3")	91.5(2)	F(3)–P–F(3")	180.0
C(12)–N(11)–C(16)	114.8(3)	C(12)–N(13)–C(14)	119.8(3)
C(22)–N(21)–C(26)	119.4(3)	N(11)–C(12)–N(13)	125.1(3)
N(11)–C(12)–C(22)	119.9(3)	N(13)–C(12)–C(22)	115.0(3)
O(14)–C(14)–N(13)	119.1(3)	O(14)–C(14)–C(15)	123.6(3)
N(13)–C(14)–C(15)	117.4(3)	C(14)–C(15)–C(16)	118.5(4)
N(11)–C(16)–C(15)	124.4(4)	N(21)–C(22)–C(12)	114.9(3)
N(21)–C(22)–C(23)	121.4(4)	C(12)–C(22)–C(23)	123.8(4)
C(22)–C(23)–C(24)	119.1(4)	C(23)–C(24)–C(25)	119.7(4)
C(24)–C(25)–C(26)	118.7(4)	N(21)–C(26)–C(25)	121.7(4)

[a] Single and double primes as superscripts refer to the following equivalent positions relative to the x, y, z set: (') –x, –y, 1–z; (") –x, –y, –z.

Packing diagrams and a stereoview of **1** are shown in Figures 5–8. The complex cations and PF$_6$ anions are alternately aligned along the *c*-axis in the crystal as shown in Figure 5. The interatomic distances
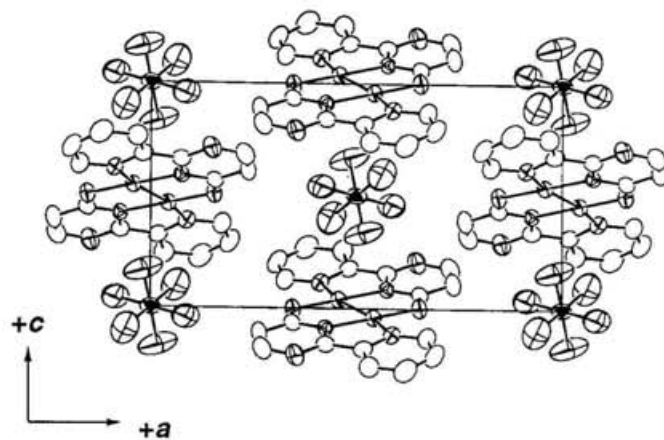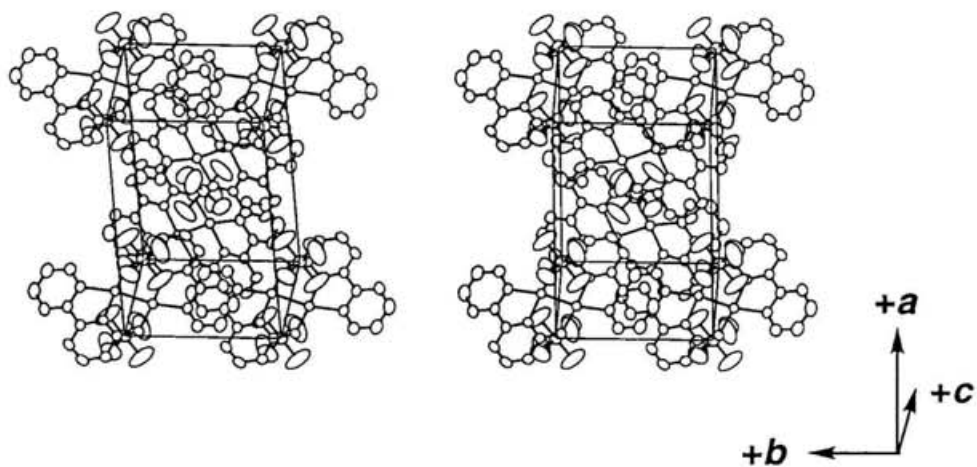
Figure 5. Packing diagram projected down to the *b*-axis for **1**.
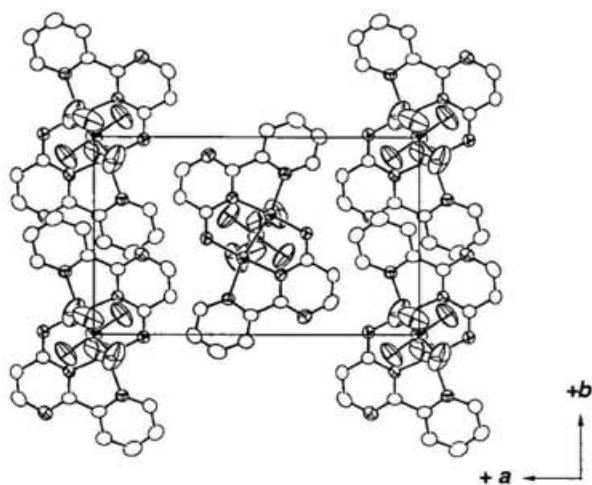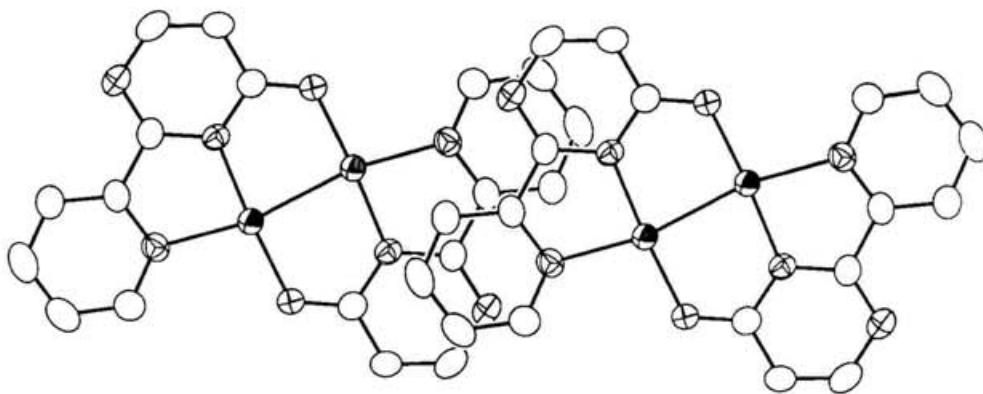

Figure 6. Packing diagram projected down to the *c*-axis for **1**.

Figure 7. Packing diagram projected down to the *a*-axis for **1**.

60
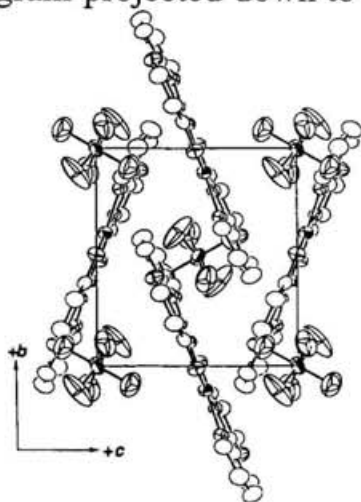
Figure 8. Stereoview of the unit cell of **1**.

Figure 9. Top view of $[\{Cu(L1)\}_2]^+$ cations in **1**.

between copper and fluorine atoms are Cu···F(3) = 2.930(4) Å, Cu···F(2) (x, y, 1+z) = 3.049(3) Å, and Cu···F(2) (−x, −y, −z) = 3.061(4) Å. The (L1)⁻ ligands of adjacent cations along the crystallographic b-axis are stacked and the interplanar spacing between the mean planes of (L1)⁻ ligands is 3.40 Å (Figure 9). The shortest intermolecular copper···copper distance is Cu···Cu (−x, 1−y, 1−z) = 7.0508(8) Å and the next is Cu···Cu (−x, −y, −z) = 7.7568(8) Å, which exclude any significant Cu···Cu interactions.

[{Cu(L3)}₂]PF₆·DMF (3). ORTEP diagram of the complex cation in **3** is shown in Figure 10. Bond distances and angles are given in Tables 8 and 9. Complex **3** was crystallized in the triclinic $P\overline{1}$ space group with two complex cations, two PF₆ anions, and two DMF molecules in the unit cell. The cation is essentially planar structure. The maximum deviation from the mean plane of the cation is 0.15(1) Å of C(25) atom. There is no crystallographically imposed symmetry but the coordination geometries about each copper atom are very similar. The two copper atoms are bridged by the N(13), O(14), N(33), and O(34) atoms of two (L3)⁻ ligands and the remaining sites are occupied by the N(21) and N(41) atoms of those ligands. The Cu(1)–Cu(2) distance is 2.403(1) Å, which is short enough to suggest the possibility of some overlap of metal orbitals.
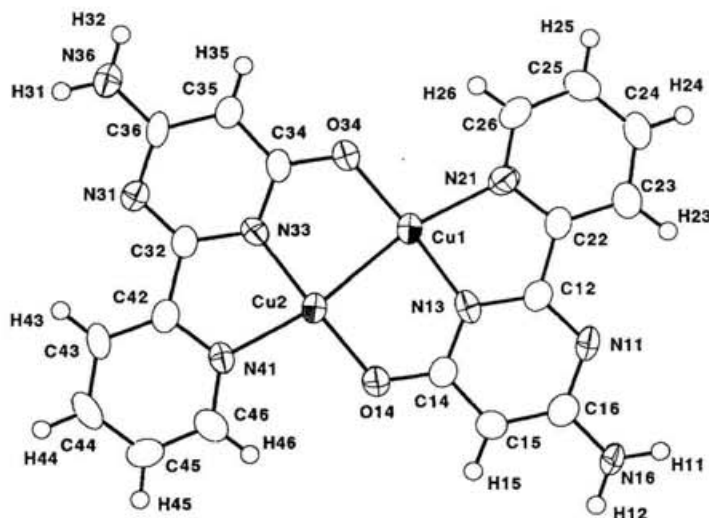
Figure 10. ORTEP diagram of [{Cu(L3)}₂]⁺ cation in **3**, showing the labeling scheme and 50 % thermal ellipsoids.

Table 8. Bond Distances (Å) with Esd's in Parentheses for [{Cu(L3)}$_2$]PF$_6$·DMF (**3**)

Cu(1)–Cu(2)	2.403(1)	Cu(1)–O(34)	1.869(5)
Cu(1)–N(13)	1.893(6)	Cu(1)–N(21)	2.031(7)
Cu(2)–O(14)	1.856(5)	Cu(2)–N(33)	1.877(6)
Cu(2)–N(41)	2.017(6)	P(1)–F(1)	1.571(6)
P(1)–F(2)	1.534(9)	P(1)–F(3)	1.537(6)
P(1)–F(4)	1.476(9)	P(1)–F(5)	1.540(9)
P(1)–F(6)	1.55(1)	O(14)–C(14)	1.285(9)
O(34)–C(34)	1.304(9)	O(51)–C(53)	1.17(2)
N(11)–C(12)	1.333(8)	N(11)–C(16)	1.39(1)
N(13)–C(12)	1.35(1)	N(13)–C(14)	1.366(9)
N(16)–C(16)	1.342(9)	N(21)–C(22)	1.337(9)
N(21)–C(26)	1.35(1)	N(31)–C(32)	1.307(8)
N(31)–C(36)	1.369(9)	N(33)–C(32)	1.354(9)
N(33)–C(34)	1.374(9)	N(36)–C(36)	1.344(9)
N(41)–C(42)	1.339(9)	N(41)–C(46)	1.351(9)
N(51)–C(51)	1.42(2)	N(51)–C(52)	1.38(2)
N(51)–C(53)	1.27(1)	C(12)–C(22)	1.48(1)
C(14)–C(15)	1.39(1)	C(15)–C(16)	1.39(1)
C(22)–C(23)	1.38(1)	C(23)–C(24)	1.39(1)
C(24)–C(25)	1.36(1)	C(25)–C(26)	1.38(1)
C(32)–C(42)	1.50(1)	C(34)–C(35)	1.398(9)
C(35)–C(36)	1.39(1)	C(42)–C(43)	1.36(1)
C(43)–C(44)	1.38(1)	C(44)–C(45)	1.37(1)
C(45)–C(46)	1.36(1)		

Table 9. Bond Angles (deg) with Esd's in Parentheses for [{Cu(L3)}$_2$]PF$_6$·DMF (**3**)

Cu(2)–Cu(1)–O(34)	90.9(2)	Cu(2)–Cu(1)–N(13)	84.8(2)
Cu(2)–Cu(1)–N(21)	166.9(2)	O(34)–Cu(1)–N(13)	175.5(3)
O(34)–Cu(1)–N(21)	102.2(2)	N(13)–Cu(1)–N(21)	82.2(2)
Cu(1)–Cu(2)–O(14)	91.1(2)	Cu(1)–Cu(2)–N(33)	85.8(2)
Cu(1)–Cu(2)–N(41)	168.2(2)	O(14)–Cu(2)–N(33)	175.5(3)
O(14)–Cu(2)–N(41)	100.7(2)	N(33)–Cu(2)–N(41)	82.4(3)
F(1)–P(1)–F(2)	90.0(4)	F(1)–P(1)–F(3)	175.9(6)
F(1)–P(1)–F(4)	90.7(6)	F(1)–P(1)–F(5)	89.6(5)
F(1)–P(1)–F(6)	88.7(5)	F(2)–P(1)–F(3)	91.6(5)
F(2)–P(1)–F(4)	87.8(7)	F(2)–P(1)–F(5)	179.5(6)
F(2)–P(1)–F(6)	91.2(6)	F(3)–P(1)–F(4)	93.1(6)
F(3)–P(1)–F(5)	88.8(5)	F(3)–P(1)–F(6)	87.4(5)
F(4)–P(1)–F(5)	92.5(7)	F(4)–P(1)–F(6)	178.9(7)
F(5)–P(1)–F(6)	88.5(7)	Cu(2)–O(14)–C(14)	121.7(5)
Cu(1)–O(34)–C(34)	121.1(4)	C(12)–N(11)–C(16)	115.3(7)
Cu(1)–N(13)–C(12)	116.3(5)	Cu(1)–N(13)–C(14)	124.5(5)

C(12)–N(13)–C(14)	119.1(6)	Cu(1)–N(21)–C(22)	113.1(5)
Cu(1)–N(21)–C(26)	128.0(5)	C(22)–N(21)–C(26)	118.9(7)
C(32)–N(31)–C(36)	115.5(7)	Cu(2)–N(33)–C(32)	117.6(5)
Cu(2)–N(33)–C(34)	124.3(5)	C(32)–N(33)–C(34)	118.1(6)
Cu(2)–N(41)–C(42)	113.2(5)	Cu(2)–N(41)–C(46)	127.6(6)
C(42)–N(41)–C(46)	119.2(7)	C(51)–N(51)–C(52)	117(1)
C(51)–N(51)–C(53)	122(1)	C(52)–N(51)–C(53)	120(1)
N(11)–C(12)–N(13)	125.8(7)	N(11)–C(12)–C(22)	119.4(7)
N(13)–C(12)–C(22)	114.8(6)	O(14)–C(14)–N(13)	117.7(6)
O(14)–C(14)–C(15)	123.5(7)	N(13)–C(14)–C(15)	118.7(8)
C(14)–C(15)–C(16)	119.2(7)	N(11)–C(16)–N(16)	116.5(8)
N(11)–C(16)–C(15)	121.8(6)	N(16)–C(16)–C(15)	121.7(7)
N(21)–C(22)–C(12)	113.6(7)	N(21)–C(22)–C(23)	121.9(7)
C(12)–C(22)–C(23)	124.5(7)	C(22)–C(23)–C(24)	117.8(8)
C(23)–C(24)–C(25)	121.1(9)	C(24)–C(25)–C(26)	117.7(8)
N(21)–C(26)–C(25)	122.5(7)	N(31)–C(32)–N(33)	126.8(7)
N(31)–C(32)–C(42)	120.2(7)	N(33)–C(32)–C(42)	113.0(6)
O(34)–C(34)–N(33)	117.9(6)	O(34)–C(34)–C(35)	123.3(7)
N(33)–C(34)–C(35)	118.8(8)	C(34)–C(35)–C(36)	117.9(7)
N(31)–C(36)–N(36)	116.6(7)	N(31)–C(36)–C(35)	122.9(6)
N(36)–C(36)–C(35)	120.5(8)	N(41)–C(42)–C(32)	113.7(7)
N(41)–C(42)–C(43)	121.0(7)	C(32)–C(42)–C(43)	125.2(7)
C(42)–C(43)–C(44)	119.9(8)	C(43)–C(44)–C(45)	118.6(9)
C(44)–C(45)–C(46)	119.3(8)	N(41)–C(46)–C(45)	121.9(8)
O(51)–C(53)–N(51)	136(2)		

Packing diagrams and a stereoview of **3** are shown in Figures 11–14. The crystal structure consists of complex cation sheets separated by layers of PF$_6$ anions and DMF molecules. The cations are stacked in an infinite column parallel to the *a*-axis, and weakly dimerized (Figure 15). The interplanar spacings between the mean planes of the complex cations are 3.06 and 3.18 Å, alternately. These distances are very shorter than the separation usually observed between stacked π-delocalized molecules.[52] On the upper and lower sites of each copper atom, the pyrimidine nitrogen and carbon atoms in ortho-positions of the amino groups are located to achieved a pseudo-octahedral environment around copper atoms: Cu(1)···N(31) (*1–x, –y, 1–z*) = 3.162(7) Å, Cu(2)···C(35) (*1–x, –y, 1–z*) = 3.119(9) Å, Cu(1)···C(15) (*–x, –y, 1–z*) = 3.175(9), Cu(2)···N(11) (*–x, –y, 1–z*) = 3.232(7) Å. As shown in Figure 16, the cations are connected together through a pair of complementary N(16)–
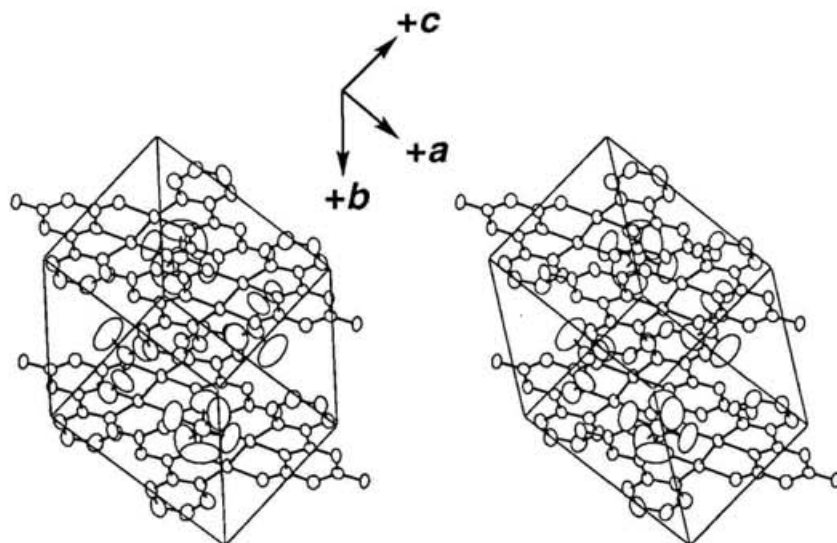
64
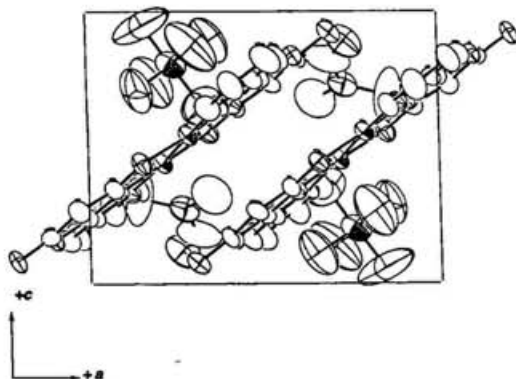
Figure 11. Packing diagram projected down to the *b*-axis for **3**.
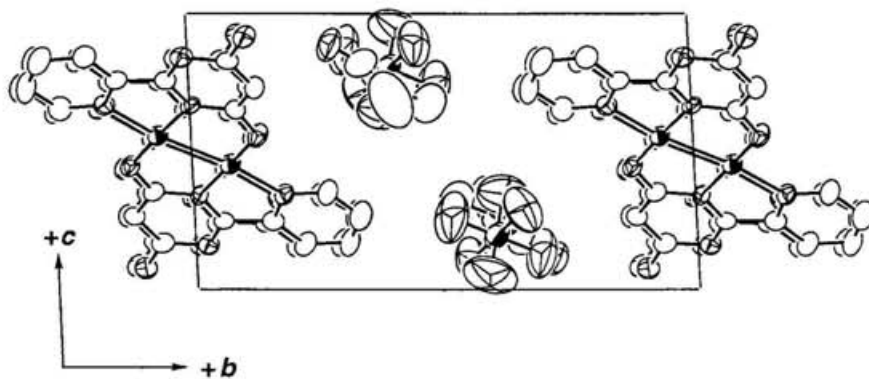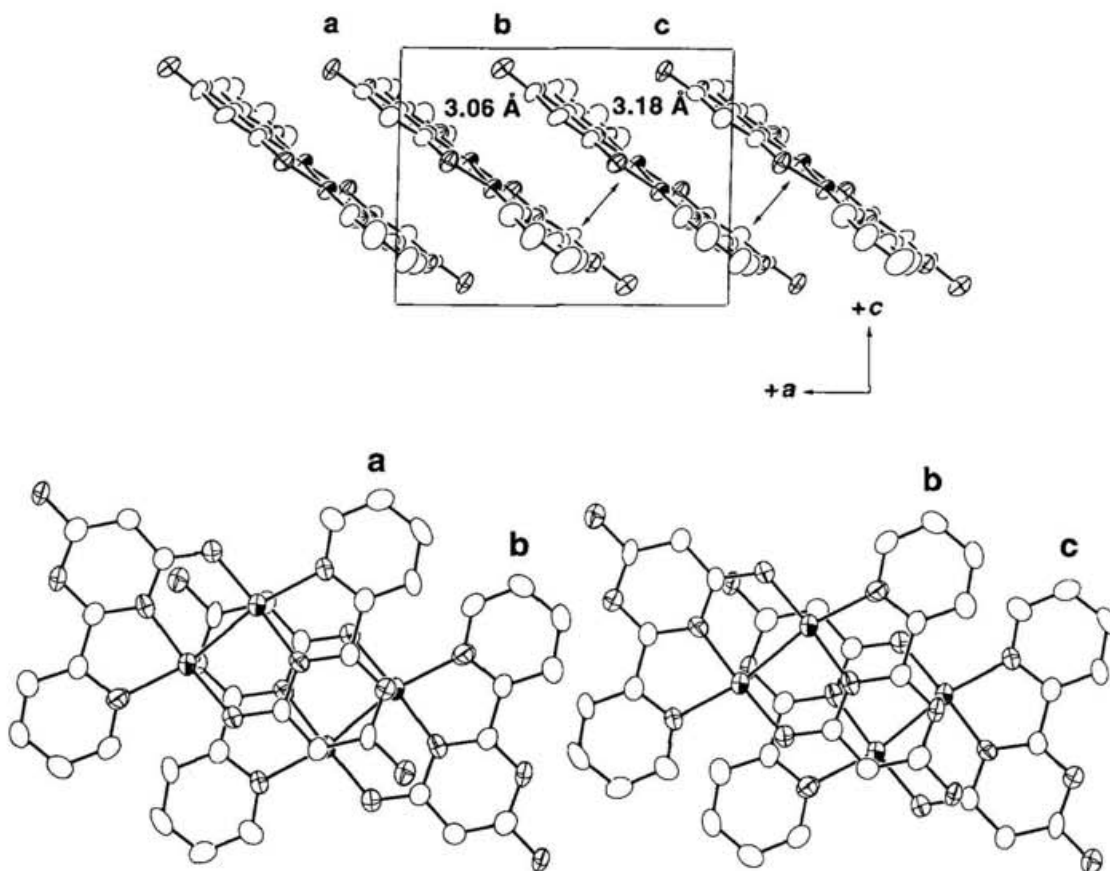

**Figure 12.** Packing diagram projected down to the *a*-axis for **3**.
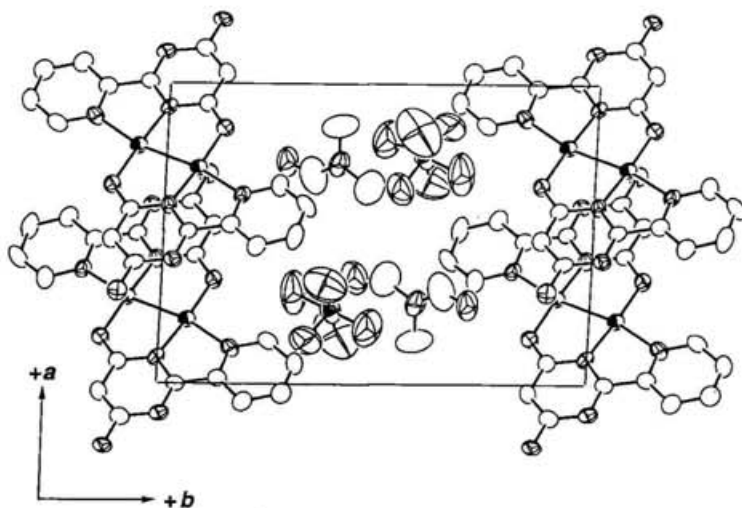
Figure 13. Packing diagram projected down to the c-axis for **3**.

Figure 14. Stereoview of the unit cell of **3**.

Figure 15. Slipped-stack structure of [{Cu(L3)}$_2$]$^+$ cation in **3**. The three cations a, b, and c are related by the following symmetry operations: (a) $1-x$, $-y$, $1-z$; (b) x, y, z; (c) $-x$, $-y$, $1-z$. (top) side view down to the b-axis; (bottom) top view showing the two types of overlap.
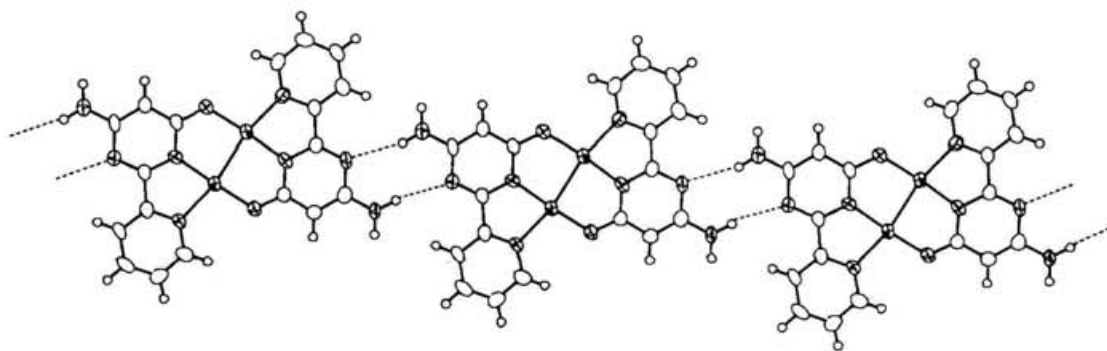
Figure 16. ORTEP diagram showing the hydrogen-bonded ribbon structure of [{Cu(L3)}$_2$]$^+$ cation in **3**.

H(11)···N(31) and N(36)–H(31)···N(11) H-bonds along to the [101] direction: N(16)···N(31) $(-1+x, y, -1+z)$ = 3.245(10) Å and N(36)···N(11) $(1+x, y, 1+z)$ = 3.204(10) Å. Therefore the infinite columns of the cations form molecular sheet parallel to the *ac* plane via these H-bonds. Another hydrogen donor sites of each amino group are participated in the N(16)–H(12)···F(5) and N(36)–H(32)···O(51) H-bonds with PF_6 anion and DMF molecule, respectively: N(16)···F(5) $(-x, -y, 1-z)$ = 3.173(10) Å and N(36)···O(51) = 2.812(10) Å. Distances and angles assigned to the H-bonding contacts are listed in Table 10.[33]

Table 10. H-Bonding Distances and Angles for **3**

D–H···A	D···A Å	D–H Å	H···A Å	D–H···A angle, deg
N(16)–H(11)···N(31)[a]	3.245(10)	0.92(8)	2.33(8)	172(6)
N(16)–H(12)···F(5)[b]	3.173(10)	0.95(8)	2.24(8)	165(7)
N(36)–H(31)···N(11)[c]	3.204(10)	0.91(8)	2.32(8)	165(7)
N(36)–H(32)···O(51)[d]	2.812(10)	0.94(8)	1.88(8)	174(7)

Symmetry operations: [a] $-1+x, y, -1+z$; [b] $-x, -y, 1-z$; [c] $1+x, y, 1+z$; [d] x, y, z.

Such infinite stack of dicopper complexes has been reported by Gagné et al. for a mixed-valence dicopper(II,I) complex $[Cu_2(L^2)](ClO_4)$[44c] and a dicopper(I) complex $Cu^I{}_2ISOIM(Etpy)_2 (pz)$.[53] In the case of $[Cu_2(L^2)](ClO_4)$, the complex cations (Figure 2) are all parallel and are arranged in slipped stack, with alternating kind of overlap as shown in Figure 17. The intermolecular distance, measured between the best planes through the four nitrogen atoms, is 3.37 Å in both cases. The molecular and crystal structures of $Cu^I{}_2ISOIM(Etpy)_2(pz)$ are shown in Figures 18 and 19. The complexes form an infinite stack in the direction of the *b*-axis. The average distance of atoms O1, C1, C8, C9, and N2 from the mean plane of atoms N1, C3, C2, C1, and O1 in the neighboring molecule just below is 3.20 Å. The shortest intermolecular copper–copper distance is 2.968 Å.
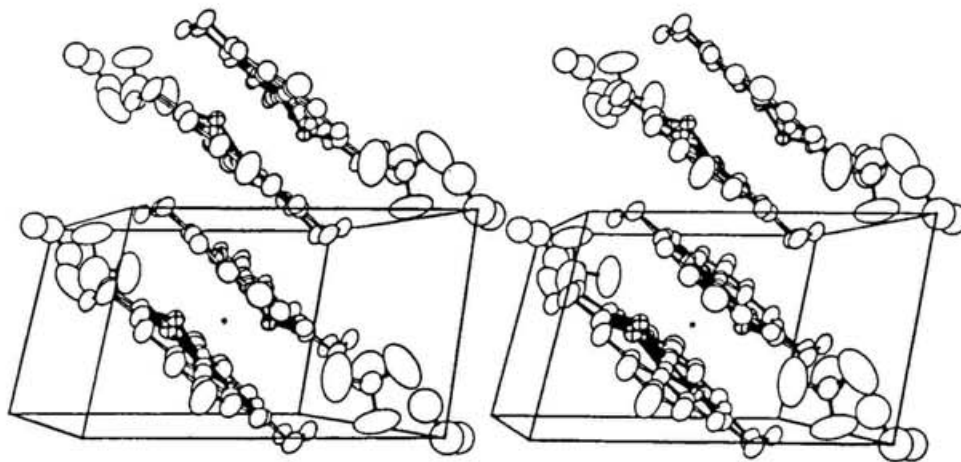
Figure 17. Crystal structures of $[Cu_2(L^2)](ClO_4)$.

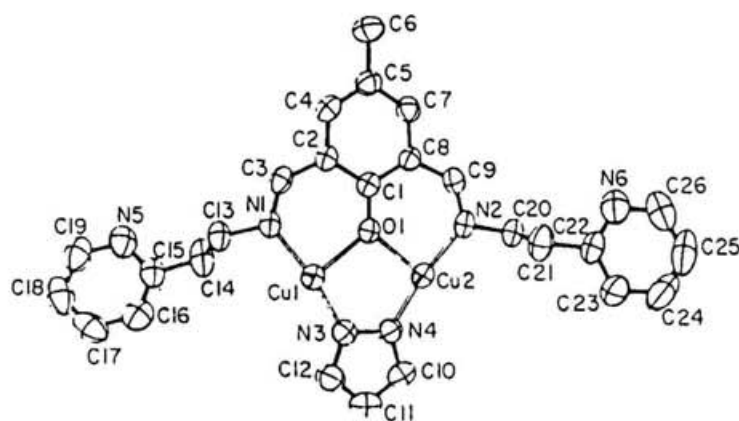**Figure 18.** Molecular structure of $Cu^I_2ISOIM(Etpy)_2(pz)$.
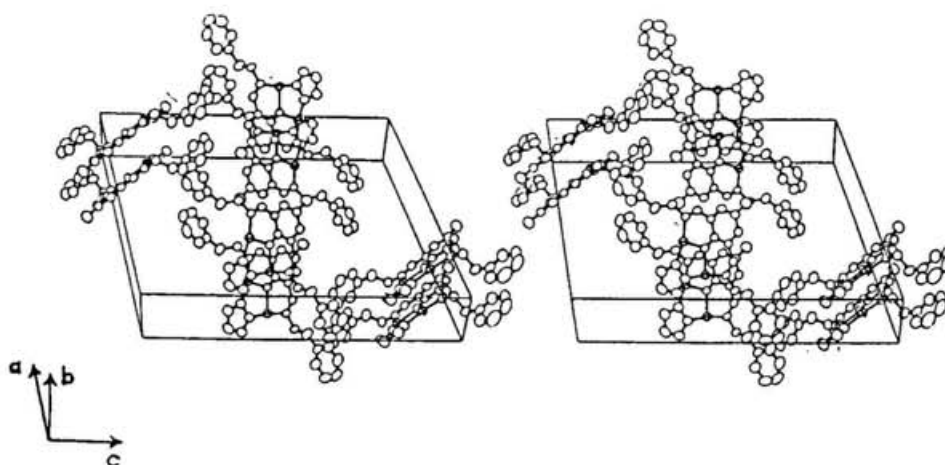
Figure 19. Crystal structures of $Cu^I_2ISOIM(Etpy)_2(pz)$.

69

[{Cu(L4)}$_2$]PF$_6$·0.5MeOH (4). ORTEP diagrams of the complex cations 1 and 2 in complex **4** are shown in Figure 20. Bond distances and angles are given in Tables 11 and 12.
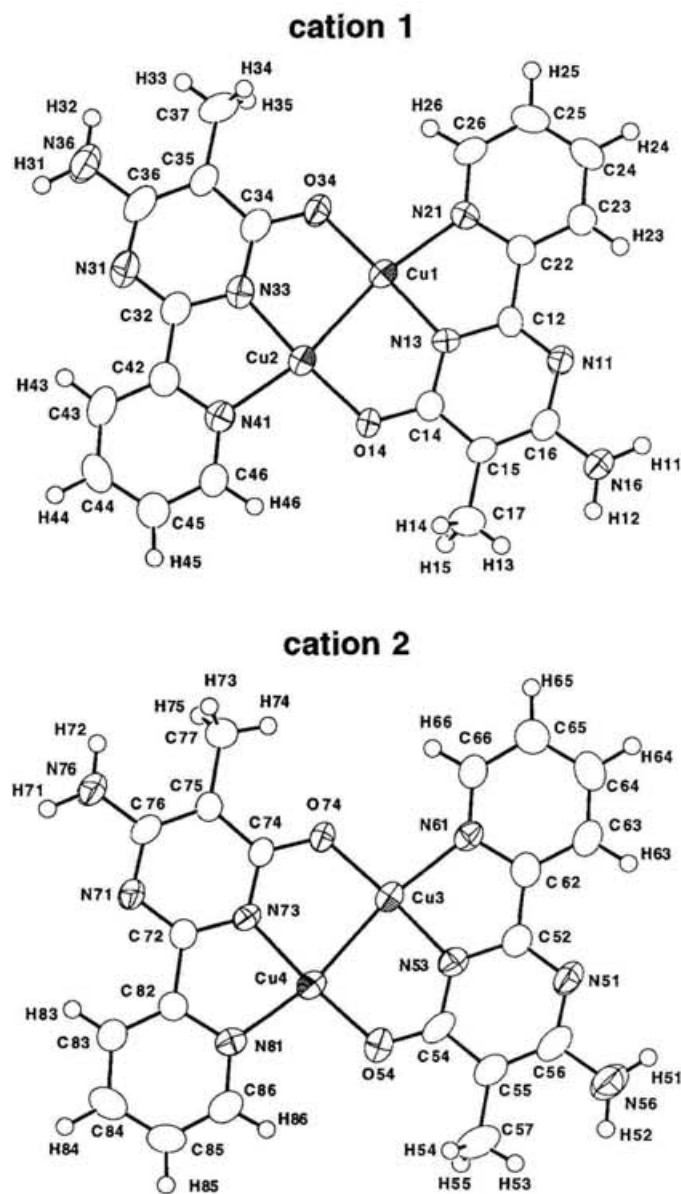
cation 1

cation 2

Figure 20. ORTEP diagrams of [{Cu(L4)}$_2$]$^+$ cations 1 (top) and 2 (bottom) in **4**, showing the labeling scheme and 50 % thermal ellipsoids.

Table 11. Bond Distances (Å) with Esd's in Parentheses for [{Cu(L4)}$_2$]PF$_6$ ·0.5MeOH (**4**)

Cu(1)–Cu(2)	2.399(1)	Cu(1)–O(34)	1.858(4)
Cu(1)–N(13)	1.900(5)	Cu(1)–N(21)	2.026(5)
Cu(2)–O(14)	1.865(4)	Cu(2)–N(33)	1.883(6)

Cu(2)–N(41)	2.025(6)	Cu(3)–Cu(4)	2.396(1)
Cu(3)–O(74)	1.861(4)	Cu(3)–N(53)	1.890(5)
Cu(3)–N(61)	2.024(6)	Cu(4)–O(54)	1.856(5)
Cu(4)–N(73)	1.893(5)	Cu(4)–N(81)	2.015(6)
P(1)–F(11)	1.557(5)	P(1)–F(12)	1.586(4)
P(1)–F(13)	1.565(5)	P(1)–F(14)	1.555(4)
P(1)–F(15)	1.561(4)	P(1)–F(16)	1.585(4)
P(2)–F(21)	1.567(5)	P(2)–F(22)	1.566(5)
P(2)–F(23)	1.545(5)	P(2)–F(24)	1.560(5)
P(2)–F(25)	1.550(5)	P(2)–F(26)	1.574(5)
O(14)–C(14)	1.291(7)	O(34)–C(34)	1.291(7)
O(54)–C(54)	1.265(8)	O(74)–C(74)	1.286(7)
O(91)–O(92)	0.93(2)	O(91)–C(91)	1.50(2)
O(92)–C(91)	1.07(2)	N(11)–C(12)	1.293(7)
N(11)–C(16)	1.357(7)	N(13)–C(12)	1.351(7)
N(13)–C(14)	1.378(7)	N(16)–C(16)	1.357(8)
N(21)–C(22)	1.354(8)	N(21)–C(26)	1.331(8)
N(31)–C(32)	1.305(8)	N(31)–C(36)	1.372(8)
N(33)–C(32)	1.341(8)	N(33)–C(34)	1.382(8)
N(36)–C(36)	1.382(9)	N(41)–C(42)	1.350(8)
N(41)–C(46)	1.321(8)	N(51)–C(52)	1.306(8)
N(51)–C(56)	1.365(8)	N(53)–C(52)	1.353(8)
N(53)–C(54)	1.379(8)	N(56)–C(56)	1.369(9)
N(61)–C(62)	1.367(8)	N(61)–C(66)	1.316(8)
N(71)–C(72)	1.309(7)	N(71)–C(76)	1.381(7)
N(73)–C(72)	1.345(8)	N(73)–C(74)	1.387(7)
N(76)–C(76)	1.359(8)	N(81)–C(82)	1.362(8)
N(81)–C(86)	1.336(8)	C(12)–C(22)	1.479(8)
C(14)–C(15)	1.407(8)	C(15)–C(16)	1.378(8)
C(15)–C(17)	1.50(1)	C(22)–C(23)	1.370(9)
C(23)–C(24)	1.366(9)	C(24)–C(25)	1.37(1)
C(25)–C(26)	1.373(9)	C(32)–C(42)	1.474(9)
C(34)–C(35)	1.388(9)	C(35)–C(36)	1.380(9)
C(35)–C(37)	1.50(1)	C(42)–C(43)	1.389(9)
C(43)–C(44)	1.39(1)	C(44)–C(45)	1.36(1)
C(45)–C(46)	1.38(1)	C(52)–C(62)	1.473(9)
C(54)–C(55)	1.391(9)	C(55)–C(56)	1.39(1)
C(55)–C(57)	1.51(1)	C(62)–C(63)	1.402(9)
C(63)–C(64)	1.37(1)	C(64)–C(65)	1.38(1)
C(65)–C(66)	1.38(1)	C(72)–C(82)	1.488(8)
C(74)–C(75)	1.397(8)	C(75)–C(76)	1.368(9)
C(75)–C(77)	1.506(9)	C(82)–C(83)	1.367(9)
C(83)–C(84)	1.395(9)	C(84)–C(85)	1.37(1)
C(85)–C(86)	1.36(1)		

Table 12. Bond Angles (deg) with Esd's in Parentheses for [{Cu(L4)}$_2$]PF$_6$ ·0.5MeOH (**4**)

Cu(2)–Cu(1)–O(34)	92.0(1)	Cu(2)–Cu(1)–N(13)	84.9(2)
Cu(2)–Cu(1)–N(21)	167.2(2)	O(34)–Cu(1)–N(13)	175.5(2)
O(34)–Cu(1)–N(21)	100.3(2)	N(13)–Cu(1)–N(21)	82.6(2)
Cu(1)–Cu(2)–O(14)	91.5(1)	Cu(1)–Cu(2)–N(33)	84.6(2)
Cu(1)–Cu(2)–N(41)	167.7(2)	O(14)–Cu(2)–N(33)	175.8(2)
O(14)–Cu(2)–N(41)	100.6(2)	N(33)–Cu(2)–N(41)	83.3(2)
Cu(4)–Cu(3)–O(74)	91.8(1)	Cu(4)–Cu(3)–N(53)	84.2(2)
Cu(4)–Cu(3)–N(61)	167.2(2)	O(74)–Cu(3)–N(53)	175.5(2)
O(74)–Cu(3)–N(61)	100.0(2)	N(53)–Cu(3)–N(61)	83.8(2)
Cu(3)–Cu(4)–O(54)	91.7(2)	Cu(3)–Cu(4)–N(73)	84.4(2)
Cu(3)–Cu(4)–N(81)	166.8(2)	O(54)–Cu(4)–N(73)	173.1(2)
O(54)–Cu(4)–N(81)	100.5(2)	N(73)–Cu(4)–N(81)	82.9(2)
F(11)–P(1)–F(12)	89.3(3)	F(11)–P(1)–F(13)	179.0(3)
F(11)–P(1)–F(14)	89.4(3)	F(11)–P(1)–F(15)	90.9(3)
F(11)–P(1)–F(16)	90.5(3)	F(12)–P(1)–F(13)	89.9(3)
F(12)–P(1)–F(14)	90.6(3)	F(12)–P(1)–F(15)	89.7(3)
F(12)–P(1)–F(16)	179.7(3)	F(13)–P(1)–F(14)	91.2(3)
F(13)–P(1)–F(15)	88.6(3)	F(13)–P(1)–F(16)	90.3(3)
F(14)–P(1)–F(15)	179.6(3)	F(14)–P(1)–F(16)	89.2(3)
F(15)–P(1)–F(16)	90.5(3)	F(21)–P(2)–F(22)	90.6(3)
F(21)–P(2)–F(23)	179.6(3)	F(21)–P(2)–F(24)	90.4(3)
F(21)–P(2)–F(25)	88.5(3)	F(21)–P(2)–F(26)	89.5(3)
F(22)–P(2)–F(23)	89.4(3)	F(22)–P(2)–F(24)	90.9(3)
F(22)–P(2)–F(25)	90.6(3)	F(22)–P(2)–F(26)	179.8(3)
F(23)–P(2)–F(24)	89.2(3)	F(23)–P(2)–F(25)	91.9(3)
F(23)–P(2)–F(26)	90.5(3)	F(24)–P(2)–F(25)	178.2(3)
F(24)–P(2)–F(26)	88.9(3)	F(25)–P(2)–F(26)	89.6(3)
Cu(2)–O(14)–C(14)	121.2(4)	Cu(1)–O(34)–C(34)	120.8(4)
Cu(4)–O(54)–C(54)	121.4(5)	Cu(3)–O(74)–C(74)	120.3(4)
O(92)–O(91)–C(91)	44(1)	O(91)–O(92)–C(91)	97(2)
C(12)–N(11)–C(16)	115.8(6)	Cu(1)–N(13)–C(12)	116.9(4)
Cu(1)–N(13)–C(14)	124.3(4)	C(12)–N(13)–C(14)	118.8(6)
Cu(1)–N(21)–C(22)	112.0(4)	Cu(1)–N(21)–C(26)	129.7(5)
C(22)–N(21)–C(26)	118.3(6)	C(32)–N(31)–C(36)	115.0(6)
Cu(2)–N(33)–C(32)	116.2(5)	Cu(2)–N(33)–C(34)	125.0(5)
C(32)–N(33)–C(34)	118.7(6)	Cu(2)–N(41)–C(42)	110.9(5)
Cu(2)–N(41)–C(46)	130.5(5)	C(42)–N(41)–C(46)	118.5(6)
C(52)–N(51)–C(56)	115.3(6)	Cu(3)–N(53)–C(52)	115.7(5)
Cu(3)–N(53)–C(54)	124.7(5)	C(52)–N(53)–C(54)	119.6(6)
Cu(3)–N(61)–C(62)	110.7(5)	Cu(3)–N(61)–C(66)	130.8(5)
C(62)–N(61)–C(66)	118.4(6)	C(72)–N(71)–C(76)	115.0(6)
Cu(4)–N(73)–C(72)	116.8(5)	Cu(4)–N(73)–C(74)	124.4(5)
C(72)–N(73)–C(74)	118.7(5)	Cu(4)–N(81)–C(82)	112.1(4)

72

Cu(4)–N(81)–C(86)	130.3(5)	C(82)–N(81)–C(86)	117.6(6)
N(11)–C(12)–N(13)	126.0(6)	N(11)–C(12)–C(22)	120.3(6)
N(13)–C(12)–C(22)	113.7(6)	O(14)–C(14)–N(13)	117.6(6)
O(14)–C(14)–C(15)	124.0(6)	N(13)–C(14)–C(15)	118.3(6)
C(14)–C(15)–C(16)	116.7(6)	C(14)–C(15)–C(17)	120.6(7)
C(16)–C(15)–C(17)	122.6(7)	N(11)–C(16)–N(16)	114.6(6)
N(11)–C(16)–C(15)	124.2(6)	N(16)–C(16)–C(15)	121.2(7)
N(21)–C(22)–C(12)	114.8(6)	N(21)–C(22)–C(23)	121.2(6)
C(12)–C(22)–C(23)	123.9(6)	C(22)–C(23)–C(24)	120.1(7)
C(23)–C(24)–C(25)	118.7(7)	C(24)–C(25)–C(26)	119.1(7)
N(21)–C(26)–C(25)	122.6(7)	N(31)–C(32)–N(33)	126.3(7)
N(31)–C(32)–C(42)	119.2(7)	N(33)–C(32)–C(42)	114.5(7)
O(34)–C(34)–N(33)	117.5(6)	O(34)–C(34)–C(35)	123.6(7)
N(33)–C(34)–C(35)	118.9(7)	C(34)–C(35)–C(36)	117.0(7)
C(34)–C(35)–C(37)	120.6(7)	C(36)–C(35)–C(37)	122.3(7)
N(31)–C(36)–N(36)	113.8(7)	N(31)–C(36)–C(35)	124.1(7)
N(36)–C(36)–C(35)	122.1(7)	N(41)–C(42)–C(32)	114.9(6)
N(41)–C(42)–C(43)	121.2(7)	C(32)–C(42)–C(43)	123.9(7)
C(42)–C(43)–C(44)	119.0(7)	C(43)–C(44)–C(45)	119.2(7)
C(44)–C(45)–C(46)	118.5(8)	N(41)–C(46)–C(45)	123.5(8)
N(51)–C(52)–N(53)	125.4(7)	N(51)–C(52)–C(62)	119.8(7)
N(53)–C(52)–C(62)	114.8(6)	O(54)–C(54)–N(53)	117.7(6)
O(54)–C(54)–C(55)	123.9(7)	N(53)–C(54)–C(55)	118.4(7)
C(54)–C(55)–C(56)	116.8(7)	C(54)–C(55)–C(57)	121.2(8)
C(56)–C(55)–C(57)	121.9(7)	N(51)–C(56)–N(56)	114.4(7)
N(51)–C(56)–C(55)	124.3(7)	N(56)–C(56)–C(55)	121.3(8)
N(61)–C(62)–C(52)	114.9(6)	N(61)–C(62)–C(63)	121.1(7)
C(52)–C(62)–C(63)	123.9(7)	C(62)–C(63)–C(64)	118.8(7)
C(63)–C(64)–C(65)	119.4(8)	C(64)–C(65)–C(66)	119.0(8)
N(61)–C(66)–C(65)	123.2(8)	N(71)–C(72)–N(73)	126.2(6)
N(71)–C(72)–C(82)	119.9(6)	N(73)–C(72)–C(82)	113.9(6)
O(74)–C(74)–N(73)	117.5(6)	O(74)–C(74)–C(75)	123.9(6)
N(73)–C(74)–C(75)	118.6(6)	C(74)–C(75)–C(76)	117.4(6)
C(74)–C(75)–C(77)	121.4(7)	C(76)–C(75)–C(77)	121.1(6)
N(71)–C(76)–N(76)	113.6(6)	N(71)–C(76)–C(75)	124.1(6)
N(76)–C(76)–C(75)	122.3(7)	N(81)–C(82)–C(72)	114.1(6)
N(81)–C(82)–C(83)	121.9(6)	C(72)–C(82)–C(83)	124.0(6)
C(82)–C(83)–C(84)	119.4(7)	C(83)–C(84)–C(85)	118.3(8)
C(84)–C(85)–C(86)	119.4(8)	N(81)–C(86)–C(85)	123.4(8)

Complex **4** was crystallized in the triclinic $P\bar{1}$ space group with four complex cations and four PF_6 anions and two disordered methanol molecules in the unit cell. The cations 1 and 2 have no crystallographically imposed symmetry and are nonplanar due to the

73

dimerization of those (Figure 21). In each cation, the two copper atoms are bridged by the nitrogen and oxygen atoms of two pyrimidine moieties and the remaining sites are occupied by the pyridine nitrogen atoms of that ligands. Within the dimer, neighboring cations are oriented so that the one oxygen atom of each cation is located mutually on the one copper atom of its neighbor: Cu(1)···O(74) = 2.865(5) Å and Cu(4)···O(14) = 2.938(4) Å. Furthermore, the short distance between Cu(2) and Cu(3) in the dimer is observed: Cu(2)···Cu(3) = 3.181(1) Å. As a result, each cation is bent in opposite direction on the lines through the Cu(1) and O(14) atoms in cation 1 and the Cu(4) and O(74) atoms in cation 2, forming the dihedral angles 8.0 and 13.3°.

Most of the hydrogen atoms of the amino groups participate in H-bonding interactions with the fluorine atoms of the PF_6 anions. Further, the neighboring cations 2 form a H-bonded dimer through a very weak complementary N(76)–H(71)···N(71) H-bonds: N(76)···N(71) (–x, –y, –1–z) = 3.311(9) Å, (see Figure 22). Distances and angles assigned to the H-bonding contacts are listed in Table 13.[33]

Table 13. H-Bonding Distances and Angles for **4**

D–H···A	D···A Å	D–H Å	H···A Å	D–H···A angle, deg
N(16)–H(12)···F(16)[a]	3.112(7)	0.95(6)	2.20(6)	159(5)
N(36)–H(32)···F(26)[b]	3.011(8)	0.96(6)	2.21(7)	139(6)
N(56)–H(52)···F(12)[c]	2.967(8)	0.96(7)	2.14(7)	144(6)
N(76)–H(71)···N(71)[d]	3.311(9)	0.99(7)	2.54(7)	134(6)
N(76)–H(72)···F(22)[e]	3.155(8)	0.94(7)	2.33(7)	147(6)

Symmetry operations: [a] –1+x, y, –1+z; [b] 1–x, 1–y, 1–z; [c] x, 1+y, z; [d] –x, –y, –1–z; [e] –x, –y, –z.

As shown in Figure 23, the dimer units form an infinite stack in the direction of the *a*-axis. The interplanar spacings between the dimer units a and b and the dimer units b and c are 3.37 Å and 3.31 Å, respectively. Figure 23 also shows two types of overlap present. In type A, on the upper sites of each copper atom, the endocyclic nitrogen and carbon

74
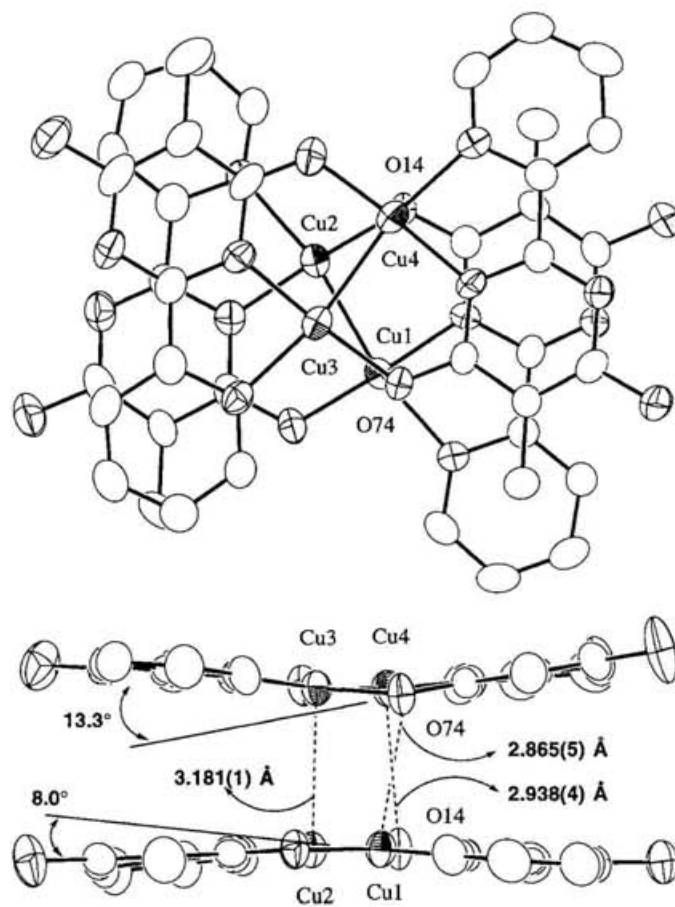
Figure 21. Dimer structures of [{Cu(L4)}$_2$]$^+$ cations in **4**.
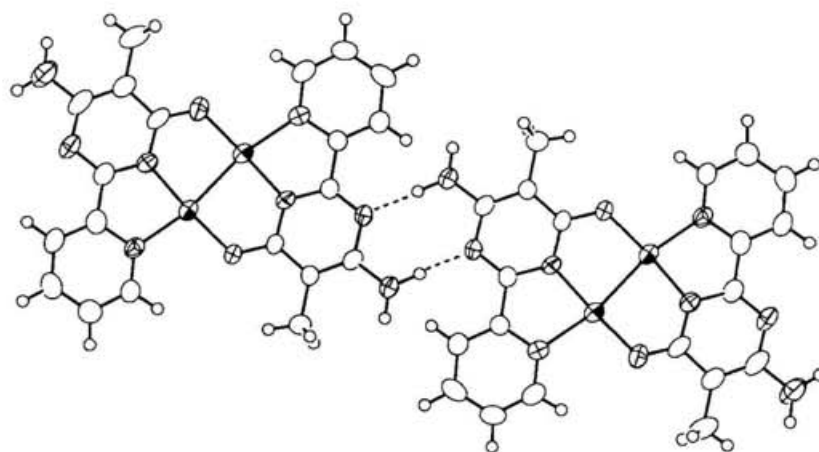
Figure 22. H-bonded dimer of [{Cu(L4)}$_2$]$^+$ cations in **4**.

75
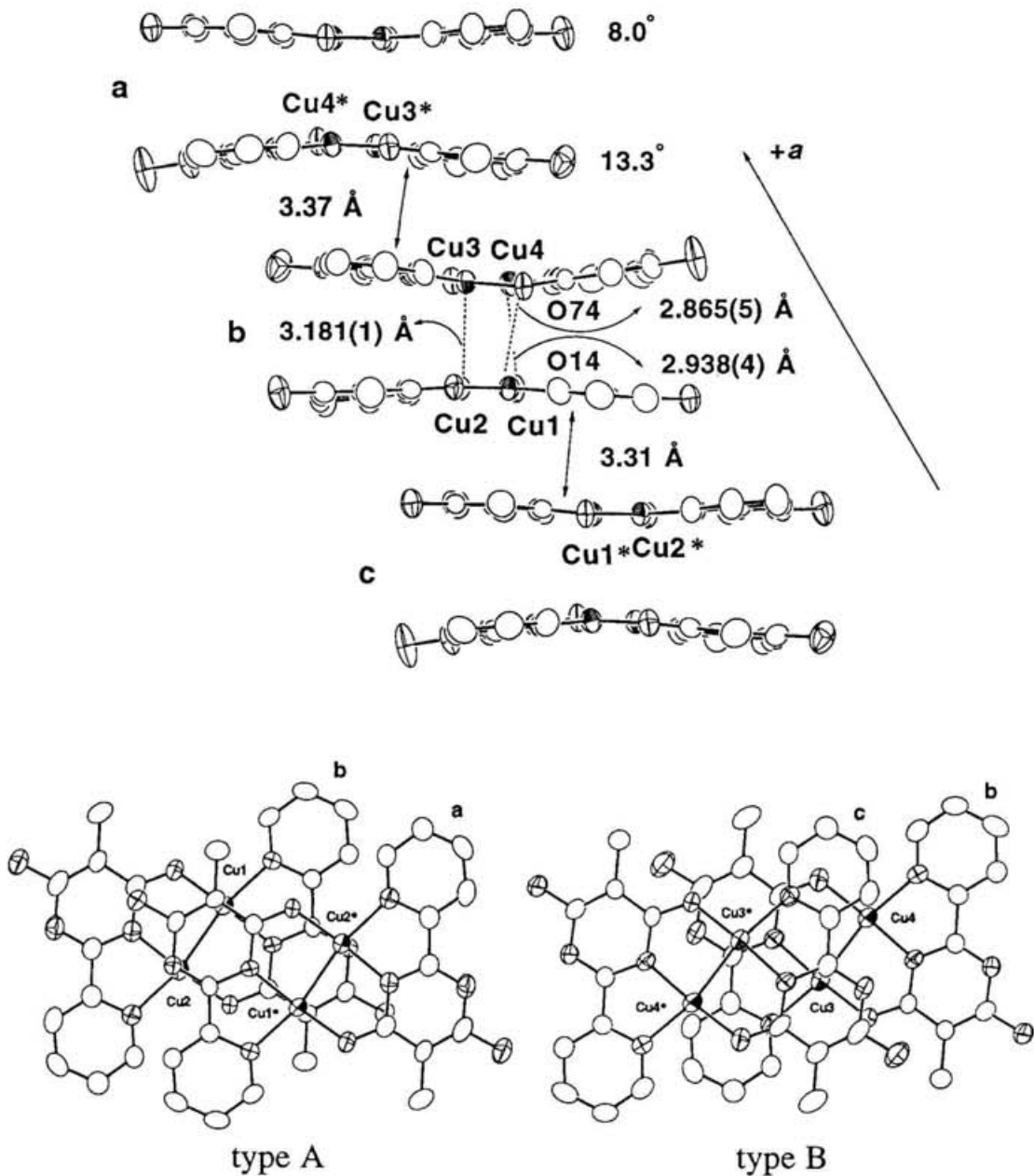
Figure 23. Stacking structure of [{Cu(L4)}$_2$]$^+$ cation in **4**. The three dimer cations a, b, and c are related by the following symmetry operations: (a) $-x$, $1-y$, $-z$; (b) x, y, z; (c) $1-x$, $1-y$, $-z$. (top) side view; (bottom) top view showing the two types of overlap.

atoms of the pyrimidine moiety are located: Cu(1)···C(15) (–x, 1–y, –z) = 3.274(6), Cu(2)···N(11) (–x, 1–y, –z) = 3.207(5) Å. In the case of type B, on the upper sites of each copper atom, two endocyclic carbon atoms of the pyrimidine moiety are located: Cu(3)···C(52) (1–x, 1–y, –z) = 3.405(7), Cu(4)···C(63) (1–x, 1–y, –z) = 3.320(7) Å. Packing diagrams and a stereoview of **4** are shown in Figures 24–27.
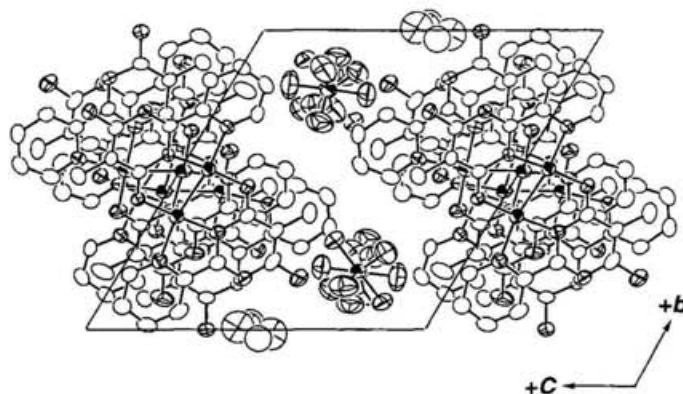
Figure 24. Packing diagram projected down to the *a*-axis for **4**.
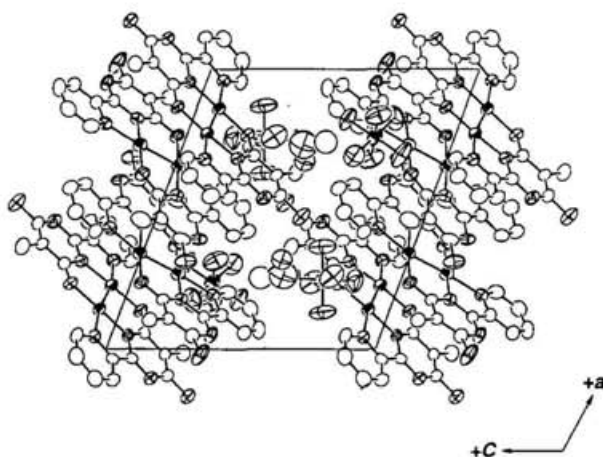
Figure 25. Packing diagram projected down to the *b*-axis for **4**.
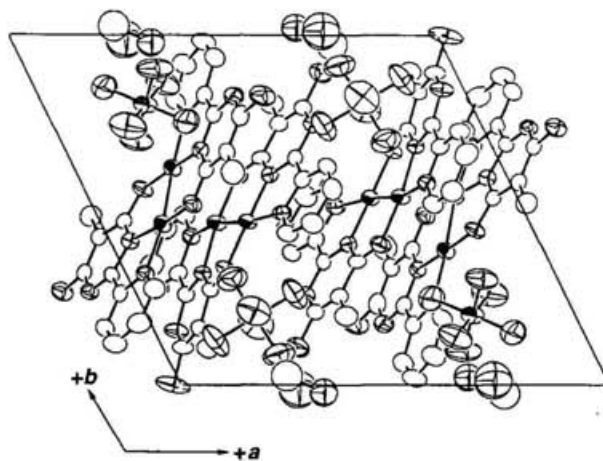
Figure 26. Packing diagram projected down to the c-axis for **4**.
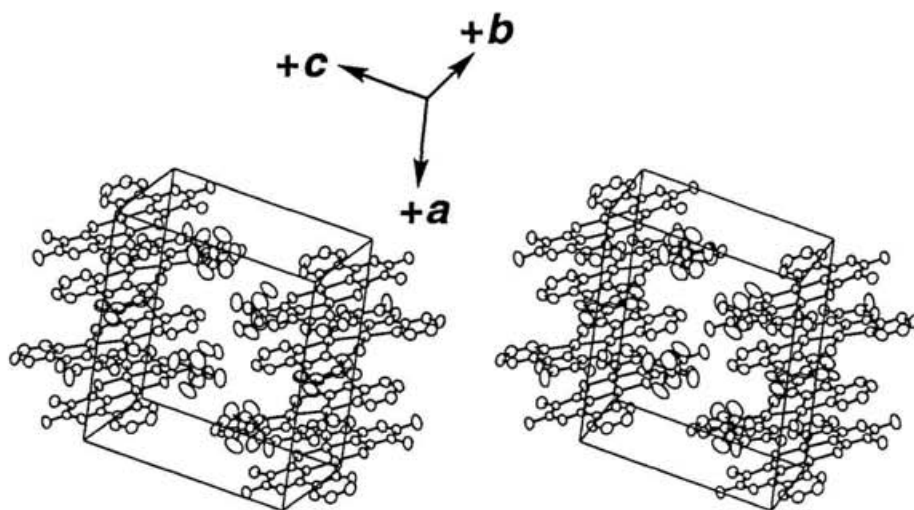
Figure 27. Stereoview of the unit cell of **4**.

Comparison of Bond Distances. For comparison the bond distances around the copper atom of complexes **1**, **3**, and **4** are summarized in Table 14. As one can see from Table 14, the corresponding bond distances in **1**, **3**, and **4** are almost the same values: Cu–Cu = 2.396(1)–2.403(1) Å, Cu–O(14) = 1.856(5)–1.869(2) Å, Cu–N(13) = 1.877(6)–1.900(5) Å, and Cu–N(21) = 2.015(6)–2.043(3) Å. The Cu–Cu distances observed for **1**, **3**, and **4** are comparable to those reported for the cryptate type mixed-valence dicopper(II,I) complexes shown in Figure 2, which have the copper–copper bonds of 2.364(1) Å in $[Cu_2(L^5)](NO_3)\cdot 2H_2O$,[45b] 2.415(1) Å in $[Cu_2(L^5)](CH_3CO_2)\cdot 6H_2O$,[45b] and 2.419(1) Å in $[Cu_2(L^6)](ClO_4)_3$.[45d] The crystal structures of 2-pyridonate bridged tetracopper(I) complex and dicopper(II) complexes have so far reported and the bond distances around copper atom of them are listed in Table 15. The Cu–O(14) and Cu–N(13) distances of **1**, **3**, and **4** are slightly longer than reported for the tetracopper(I) complex $[Cu_4(6\text{-mpyd})_4]$.[54] The distances are shorter than those reported for dicopper(II) complexes $[Cu_2(3\text{-epyd})_4(DMF)_2]$[55] and $[Cu_2(6\text{-cpyd})_4]$.[56]

Table 14. Comparison of Bond Distances (Å) in Complexes 1, 3, and 4

Bond[a]		1	3		4			
					Cation 1		Cation 2	
Cu–Cu	Cu–Cu*	2.4028(8)	Cu(1)–Cu(2)	2.403(1)	Cu(1)–Cu(2)	2.399(1)	Cu(3)–Cu(4)	2.396(1)
Cu–O(14)	Cu–O(14)	1.869(2)	Cu(1)–O(34)	1.869(5)	Cu(1)–O(34)	1.858(4)	Cu(3)–O(74)	1.861(4)
			Cu(2)–O(14)	1.856(5)	Cu(2)–O(14)	1.865(4)	Cu(4)–O(54)	1.856(5)
Cu–N(13)	Cu–N(13)	1.890(3)	Cu(1)–N(13)	1.893(6)	Cu(1)–N(13)	1.900(5)	Cu(3)–N(53)	1.890(5)
			Cu(2)–N(33)	1.877(6)	Cu(2)–N(33)	1.883(6)	Cu(4)–N(73)	1.893(5)
Cu–N(21)	Cu–N(21)	2.043(3)	Cu(1)–N(21)	2.031(7)	Cu(1)–N(21)	2.026(5)	Cu(3)–N(61)	2.024(6)
			Cu(2)–N(41)	2.017(6)	Cu(2)–N(41)	2.025(6)	Cu(4)–N(81)	2.015(6)

[a]The numbering scheme shown blow is used.
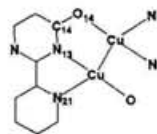
Table 15. Bond Distances (Å) around Copper Atom

Bond[a]	$[Cu^I_4(6\text{-mpyd})_4]$	$[Cu^{II}_2(3\text{-epyd})_4(DMF)_2]$	$[Cu^{II}_2(6\text{-cpyd})_4]$
Cu–Cu	2.666(1)–2.709(1)	2.550(1)	2.4989(11)
Cu–O(2)	1.823(4)–1.843(4)	1.956(6), 1.961(6)	1.928 ± 0.004^b
Cu–N(1)	1.878(4)–1.892(4)	1.997(6), 2.003(6)	2.014 ± 0.014^b

[a]The numbering scheme shown blow is used. [b]Average distance. 6-mpyd = 6-methyl-2-pyridonate; 3-epyd = 3-ethyl-2-pyridonate, 6-cpyd = 6-chloro-2-pyridonate.

79
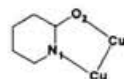
MO calculations. Barr et al.[45b] reported the Fenske–Hall MO calculation of the structurally characterized cryptate type mixed-valence dicopper complex $[Cu_2(L^5)]^{3+}$ (see Figure 2). The results indicated that the SOMO consists primarily of Cu d_{z^2}–Cu d_{z^2} σ^* combination. However, the copper–copper bond is unknown for the complex which has the SOMO composed of Cu $d_{x^2-y^2}$–Cu $d_{x^2-y^2}$ σ^* combination. In order to confirm the presence of copper–copper bond and the composition of SOMO, the ZINDO calculations were performed on the complexes **1** and **3** using the geometry of the crystal structures. The Energy Levels of **1** and **3** are presented in Figure 28 . The SOMO of **1** and **3** are mainly composed of Cu $d_{x^2-y^2}$–Cu $d_{x^2-y^2}$ σ^* combination. While the HOMO of **1** and **3** are mainly composed of Cu $d_{x^2-y^2}$–Cu $d_{x^2-y^2}$ σ-bonding interaction. The Wyberg bond indexes of Cu–Cu in **1** and **3** are 0.35. These values suggest the presence of the copper–copper bond.
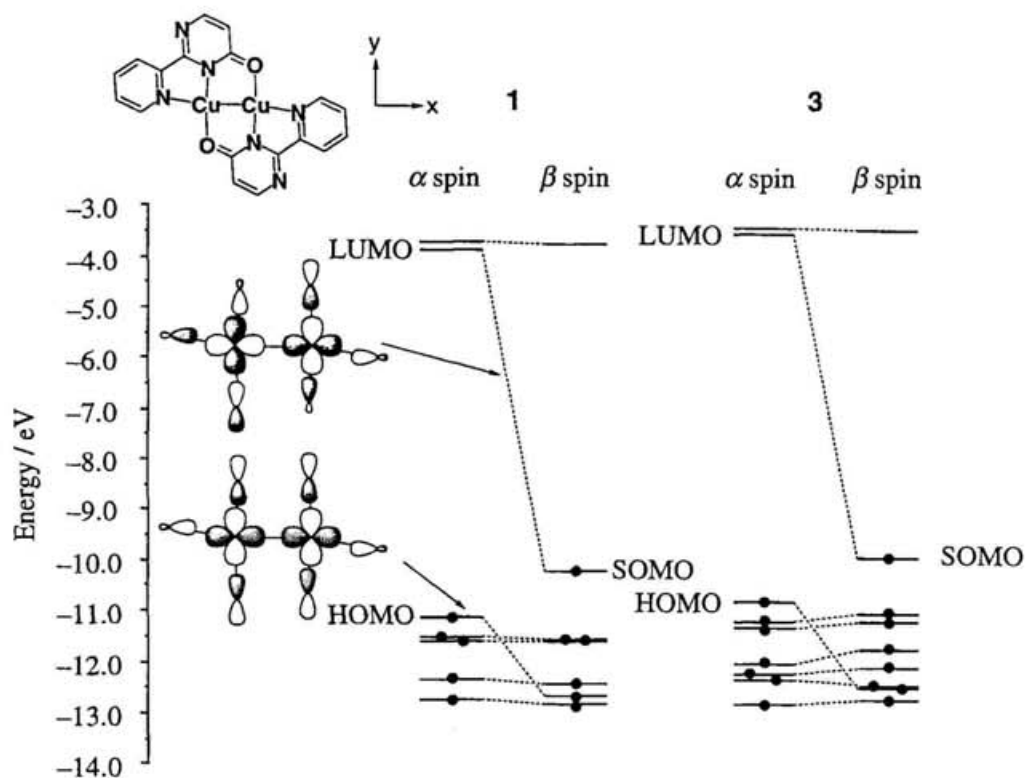
Figure 28. Energy Levels calculated by the UHF-INDO/1 method for **1** and **3**.

2. 3. 2 Magnetic Properties

Magnetic susceptibility measurements were performed for crystalline samples in the temperature range of 2–280 K.

[{Cu(L1)}$_2$]PF$_6$ (1). The χ_M^{-1} vs. T and $\chi_M T$ vs. T plots are shown in Figure 29, where χ_M and T denote molar magnetic susceptibility and temperature, respectively. The χ_M^{-1} vs. T plot of **1** obeys the Curie-Weiss law with a negative Weiss constant of $\Theta = -0.21$ K and a Curie constant $C = 0.395$ emu K mol^{-1}. The negative Weiss constant Θ indicates the operation of an antiferromagnetic interaction. The $\chi_M T$ value at 280 K is 0.395 emu K mol^{-1} that well agrees with a noncoupled copper(II) complex ($N\beta^2 g^2/4k$ = ca. 0.40 emu K mol^{-1}, where N, β, g, and k denote Avogadro number, Bohr magneton, g factor, and Boltzmann constant, respectively). On lowering the temperature, the $\chi_M T$ keeps constant value and then decreases slightly below 5 K. A slight decrease in the magnetic moment may be attribute to a very weak intermolecular antiferromagnetic interaction.

[{Cu(L2)}$_2$]PF$_6$ (2). The χ_M vs. T plot is shown in Figure 30. The $\chi_M T$ value at 280 K is 0.379 emu K mol^{-1}, which is slightly lower than the expected value for a noncoupled copper(II) complex ($N\beta^2 g^2/4k$ = ca. 0.40 emu K mol^{-1}). The χ_M vs. T plot shows a round maximum at about 12 K, and shows the tendency to have finite susceptibility as the temperatures approach zero. This behavior is expected for an infinite linear chain. The magnetic susceptibility data were analyzed by Heisenberg linear chain model. The spin Hamiltonian is

$$H = -2J\sum_i S_i \cdot S_{i+1}$$

where J is the intrachain exchange-coupling constant and the summation is over all numbers of the chain. The following numerical expression by Hall was used to fit the data.[57]

$$\chi_M = \frac{Ng^2\beta^2}{kT}\frac{0.25 + 0.14995X + 0.30094X^2}{1.0 + 1.9862X + 0.68854X^2 + 6.0626X^3} \tag{2}$$
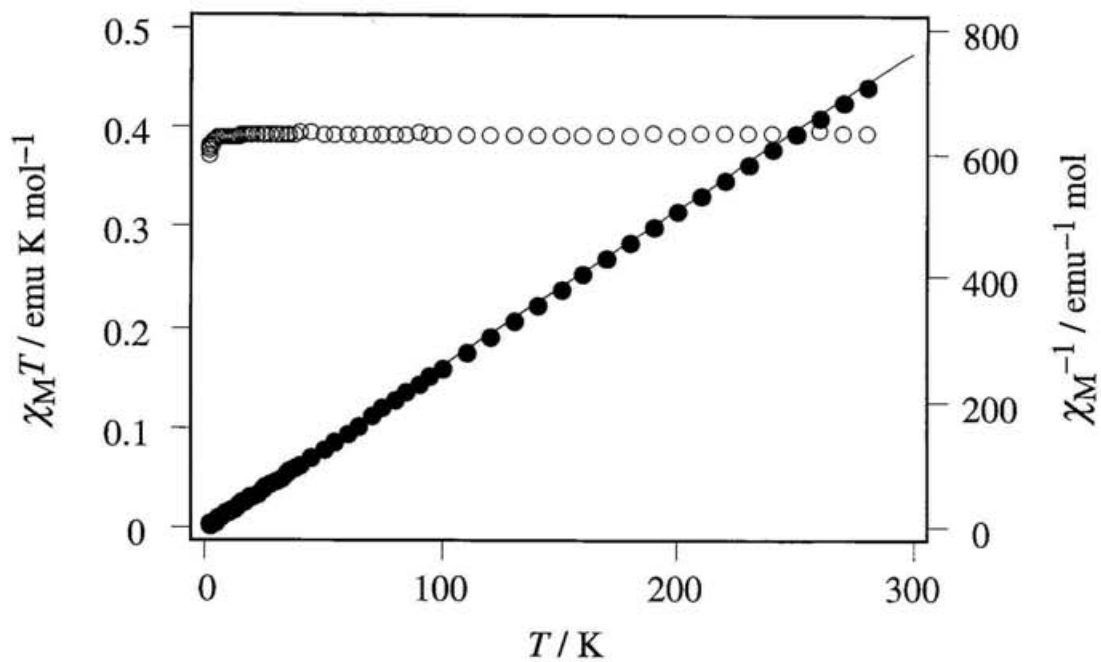
Figure 29. χ_M^{-1} vs T ($\bullet$) and $\chi_M T$ vs T ($\circ$) plots for complex **1**.
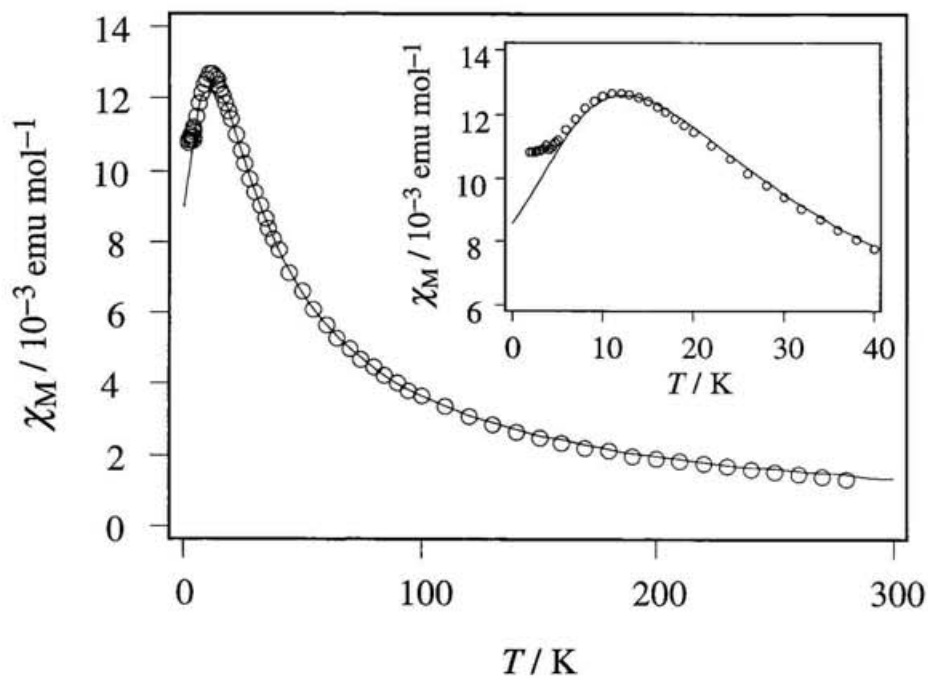

Figure 30. χ_M vs T plot for complex **2**.

82

where

$$X = |J|/kT$$

The parameters were found as $J = -6.7$ cm^{-1} and $g = 2.10$. Below 4 K, the χ_M vs. T curve is deviated from the theoretical curve, which is attributable to the presence of small amounts of noncoupled impurities.[51] The detailed crystal structure of **2** is unknown. The one-dimensional Heisenberg magnetic behavior of **2**, however, suggests that the complex cations are aligned at equal spaces and presumably form the stacked column structure as shown in Figure 31.
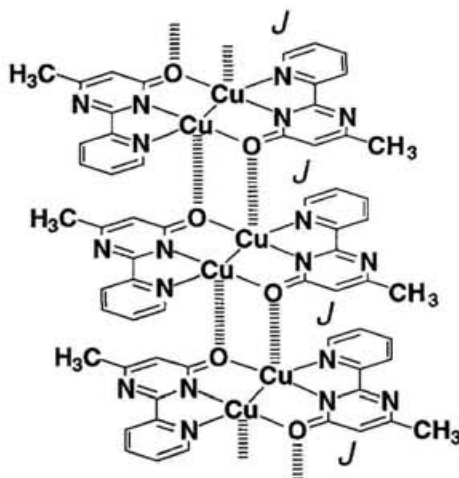
Figure 31. Schematic drawing of Proposed uniform stacked column structure.

[{Cu(L3)}₂]PF₆·DMF (3). The χ_M^{-1} vs. T and $\chi_M T$ vs. T plots are shown in Figure 32. The χ_M^{-1} vs. T plot of **3** obeys the Curie-Weiss law behavior with a positive Weiss constant of $\Theta = +0.11$ K and a Curie constant $C = 0.420$ emu K mol^{-1}. In contrast to **1**, the complex **3** shows the positive Weiss constant Θ which indicates the operation of a ferromagnetic interaction. The $\chi_M T$ value at 280 K is 0.420 emu K mol^{-1} that well agrees with a noncoupled copper(II) complex ($N\beta^2 g^2/4k$ = ca. 0.40 emu K mol^{-1}). On lowering the temperature, the $\chi_M T$ keeps constant value and then increases very slightly below 15 K. The observed magnetic behavior strongly suggests the operation of very weak intermolecular ferromagnetic spin-exchange interaction. The

83
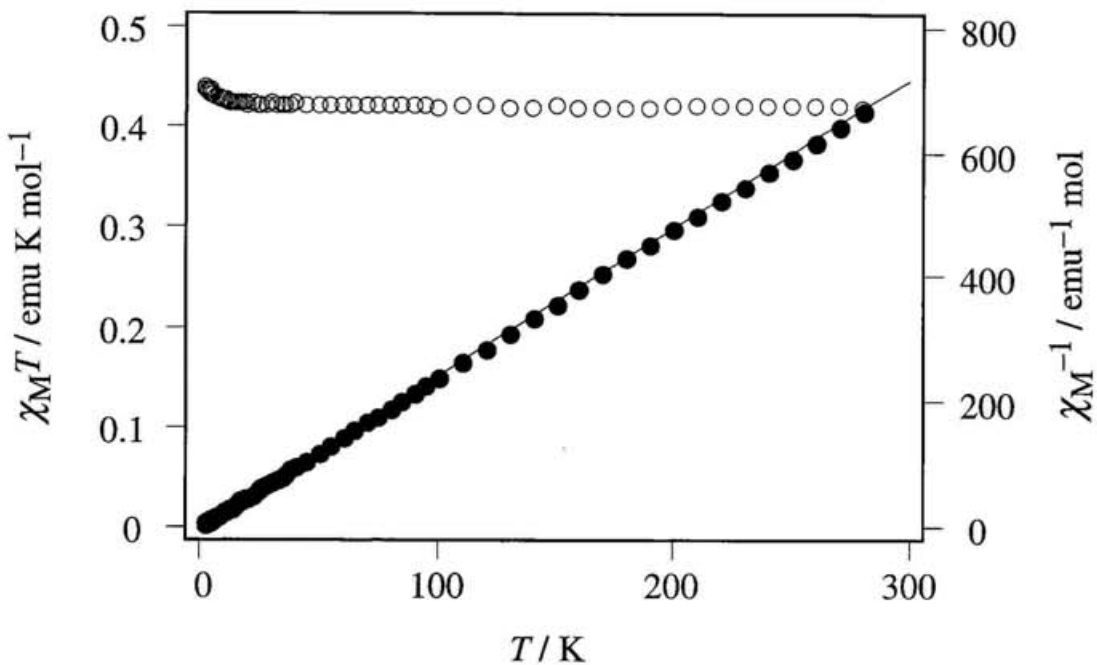
Figure 32. χ_M^{-1} vs T ($\bullet$) and $\chi_M T$ vs T ($\circ$) plots for complex **3**.
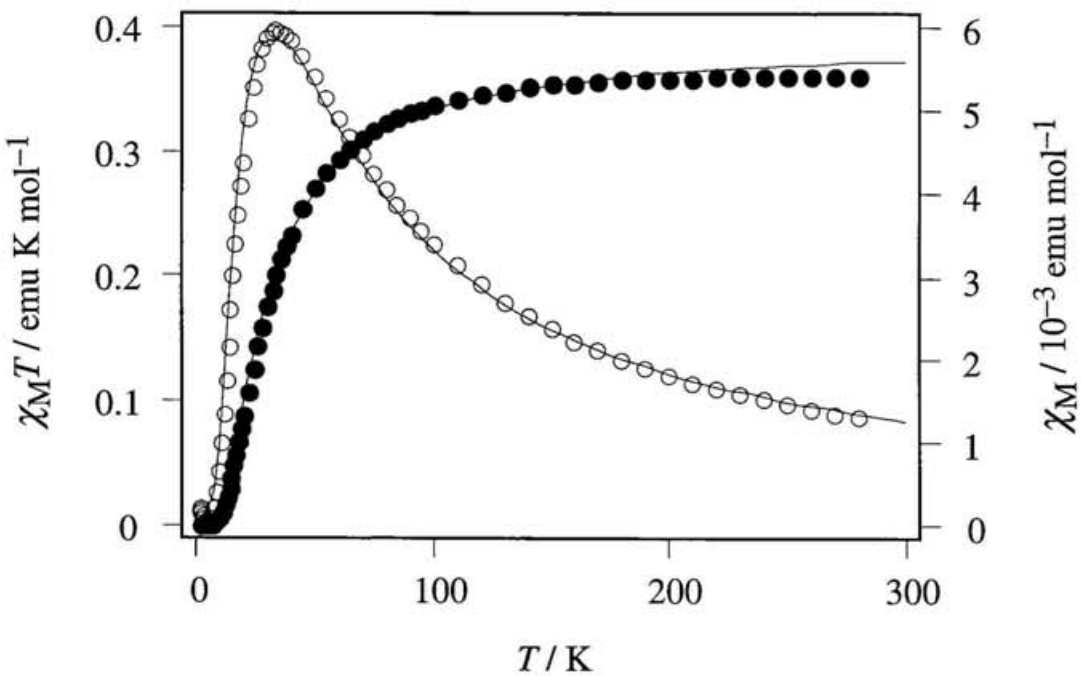
Figure 33. χ_M vs T ($\circ$) and $\chi_M T$ vs T ($\bullet$) plots for complex **4**.

84

ferromagnetic spin-coupling observed for **3** can be rationalized by the simple Heitler–London model.[58] The exchange coupling constant J between two singly occupied molecular orbitals (SOMOs), a and b, can be expressed by this model as follows.

$$J = 2\beta S + K \qquad (3)$$
$$S = \int ab\, dv$$
$$\beta = \int a\hat{h}b\, dv$$
$$K = \int a(1)b(2)\frac{e^2}{r_{12}}a(2)b(1)\, dv_1 dv_2$$

where K, S, and β represent the bielectronic exchange integral, the overlap integral between the magnetic orbitals, and the resonance integral, respectively. The equation 3 contains two terms of opposite sign. Monoelectronic term $2\beta S$, proportional to $-S^2$, is negative, which represents the antiferromagnetic contribution to J. As for the bielectronic exchange integral K, it has positive sign and represent ferromagnetic contribution to J. The crystal structure of **3** shows that the cations which have the SOMO composed of Cu $d_{x^2-y^2}$–Cu $d_{x^2-y^2}$ σ^* combination in the plane are slipped stacked with alternate distances of 3.06 and 3.18 Å as shown Figure 34. It follows that the overlap between the SOMOs is expected to be very small if not negligible. Thus, the $2\beta S$ term is expected to be less small compared with the K term so that the weak intermolecular ferromagnetic interaction may be slightly predominant.
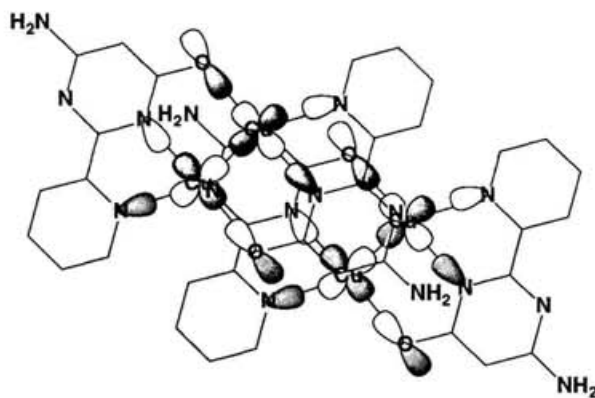
Figure 34. Schematic drawing of orientation of SOMOs for **3**.

[{Cu(L4)}₂]PF₆·DMF (4). The $\chi_M T$ vs. T and χ_M vs. T plots are shown in Figure 33. At 280 K, the $\chi_M T$ value is 0.359 emu K mol⁻¹, which is a little lower than that expected for a noncoupled copper(II) complex ($N\beta^2 g^2/4k$ = ca. 0.40 emu K mol⁻¹). The $\chi_M T$ value decreases gradually as the temperature was lowered from 280 to 100 K and rapidly blow 100 K. The χ_M increases with lowering the temperature until a round maximum in χ_M is reached at ca. 34 K. Below this temperature the χ_M decreases rapidly. The data were fitted to the Bleaney-Bowers expression[59] (eq 4) for intradimer exchange coupled copper(II) pairs, using the isotropic spin Hamiltonian ($H = -JS_1S_2$) for two $S = 1/2$ centers

$$\chi_M = \frac{Ng^2\beta^2}{kT}\left[3 + \exp\left(-\frac{J}{kT}\right)\right]^{-1} \quad (4)$$

to give $J = -36.9$ cm⁻¹ and $g = 2.04$, where J is the spin singlet-triplet energy gap. Such behavior reveals an intradimer antiferromagnetic interaction with the spin singlet ground state. This result is consistent with the dimerization of the cations in the solid state.

Magnetization Data for 1 and 3. To confirm the ground spin state, the field dependences of the magnetization M of **1** and **3** were measured on crystalline samples up to 5.5 T at 2 K. The $M/N\beta$ vs. H curves are shown in Figures 35 and 36, where H is applied magnetic field. The experimental data of M obtained for **1** and **3** agreed with the theoretical curves of $M = Ng\beta SB_s(y)$ represented by the Brillouin function $B_S(y)$ with $S = 1/2$, where $g = 2.1$ for **1** and $g = 2.2$ for **3**. These results also demonstrate that **1** and **3** are the mixed-valence dicopper(II,I) complex.

$$M = Ng\beta SB_s(y)$$

$$B_s(y) = \frac{2S+1}{2S}\coth\left[\frac{2S+1}{2S}y\right] - \frac{1}{2S}\coth\left[\frac{1}{2S}y\right]$$

where

$$y = \frac{g\beta SH}{kT}$$
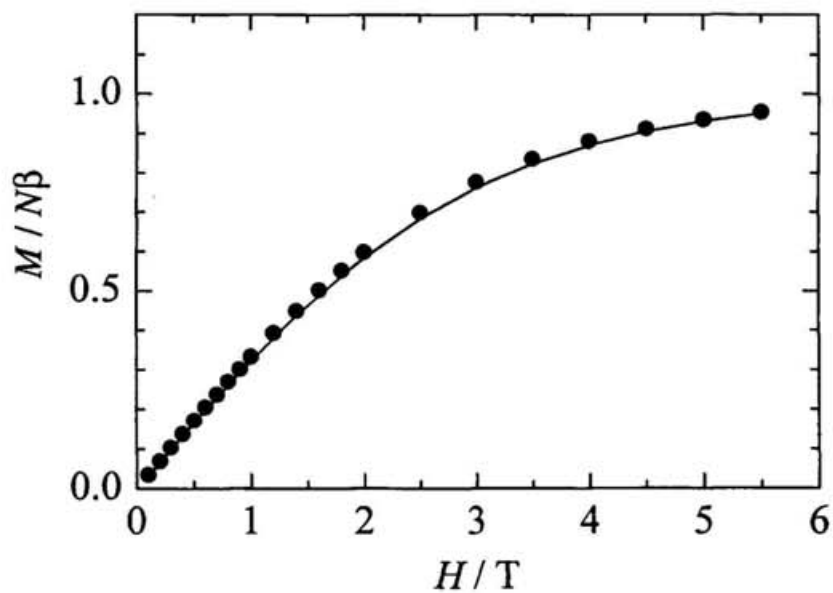
Figures 35. Field dependence of the magnetization M for complex **1** at 2 K. Solid curve is drawn according to the theoretical Brillouin function with $g = 2.1$ and $S = 1/2$.
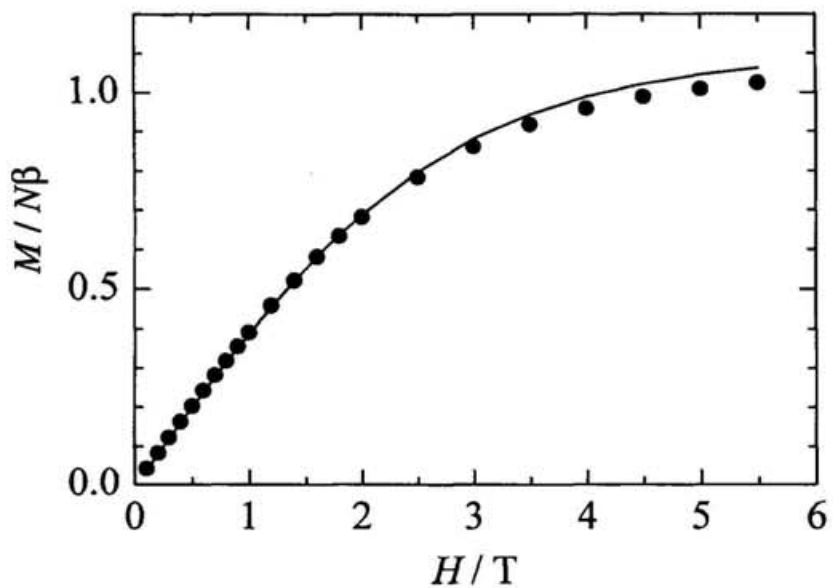
Figures 36. Field dependence of the magnetization M for complex **3** at 2 K. Solid curve is drawn according to the theoretical Brillouin function with $g = 2.2$ and $S = 1/2$.

2. 3. 3 Electronic Absorption Spectra.

Electronic absorption spectra of the complexes **1–4** in the visible–near-IR region were measured in the solid state (dispersed in KBr) and CH_2Cl_2 or DMF solution. Solution spectram of **2** was measured in noncoordinating CH_2Cl_2. Insolubility of **1**, **3**, and **4** in that solvent prevented spectral measurement. Therefore, the spectra for **1**, **3**, and **4** were examined in weakly coordinating DMF together with that of **2**. The spectral data for **1–4** are summarized in Table 16.

The electronic absorption spectra of **1–4** in the solid state are shown in Figure 37. All the spectra of **1–4** exhibit the tail of an intense absorption in the range of 350–400 nm that is presumably attributable to the ligand absorption. The complexes **1–4** exhibit two absorbance maxima, a band in the region of 462–476 nm and a more intense band in the region of 734–754 nm, and the low-intensity maximum or shoulder in the region of 550–600 nm. Furthermore, the complexes **3** and **4** exhibit a broad low intensity shoulder around 1100 nm, respectively.

The solution spectra of the complex **2** are shown in Figure 38. The spectram of **2** in CH_2Cl_2 solution exhibits three absorbance maxima; 460 nm (ε_{max} 1400 $M^{-1}cm^{-1}$), 566 nm (ε_{max} 810 $M^{-1}cm^{-1}$), and 750 nm (ε_{max} 3400 $M^{-1}cm^{-1}$). This spectram is consistent with that observed in the solid state, which suggests that dicopper(II,I) unit is retained in the CH_2Cl_2 solution.

Generally, the mixed-valence complexes have relatively intense bands in the visible and near-infrared regions of their spectra which are present only for the mixed-valence complexes.[42,43] The bands have been described as intervalence transfer (IT) bands in which photoassisted electron transfer occurs between the metal centers. The electronic absorption spectra for the mixed-valence dicopper(II,I) complexes have been reported so far. Gagné et al.[44a,44b] and Hendrickson et al.[44d] reported that the mixed-valence dicopper(II,I) complexes of macrocycle ligands, $[Cu_2(L^2)](ClO_4)$ and I–VII (see Figure 40), in which each dicopper unit is bridged by the phenolic oxygen atoms exhibit several solvent-dependent bands in the region of 600–1700 nm. These absorption bands were assigned to the intervalence transfer (IT) transition within the

Cu_2^{3+} unit. Nelson et al.,[45a] Barr et al.,[45b] and Thomson et al.[45d] reported that the cryptate type mixed-valence dicopper(II,I) complexes having a copper–copper bond, $[Cu_2(HL^4)]^{4+}$, $[Cu_2(L^5)]^{3+}$, and $[Cu_2(L^6)]^{3+}$ (see Figure 2), exhibit an intense band in the region of 750–850 nm (ε_{max} ca. 5000 $M^{-1}cm^{-1}$). In the Class III type mixed-valence complex, no intervalence transfer takes place. These absorption bands were assigned to an allowed transition between ground and excited state of the Cu_2^{3+} unit. From these reported results, the observed near-IR band (750 nm, ε_{max} 3400 $M^{-1}cm^{-1}$) for **2** has been assigned to the IT absorption.

On the other hand, the spectram of **2** in DMF solution exhibits two absorbance maxima; 488 nm (ε_{max} 1500 $M^{-1}cm^{-1}$) and 846 nm (ε_{max} 2300 $M^{-1}cm^{-1}$) (Figure 38). The IT band in the near-IR region is shift to lower energy with a decrease in intensity compared to that observed in CH_2Cl_2 solution. This is presumably attributable to the preferential ligation of the DMF molecule to the axial site of either Cu(II) or Cu(I) ion.

The spectra of the complexes **1**, **3**, and **4** in DMF are shown in Figure 39. These spectra exhibit two absorbance maxima; a band in the region of 468–490 nm (ε_{max} ca. 830–1400 $M^{-1}cm^{-1}$) and a more intense band in the region of 790–854 nm (ε_{max} ca. 1200–2200 $M^{-1}cm^{-1}$). In addition to these bands, the complexes **3** and **4** exhibit a weak broad band at 544 nm (660 $M^{-1}cm^{-1}$) and 540 nm (800 $M^{-1}cm^{-1}$), respectively. Similarly to **2**, each IT band in the near-IR region observed for **1**, **3**, and **4** is shift to lower energy compared to that observed in the solid state. Furthermore, the broad low intensity shoulder around 1100 nm observed for **3** and **4** in the sold state is absent in the DMF solution, which suggests that this shoulder is attributable to the presence of the intermolecular interaction in the solid state. When exposed to molecular oxygen, each DMF solution of **1**–**4** turns green and exhibits only a weak d–d band around 650 nm in the visible–near-IR regions.
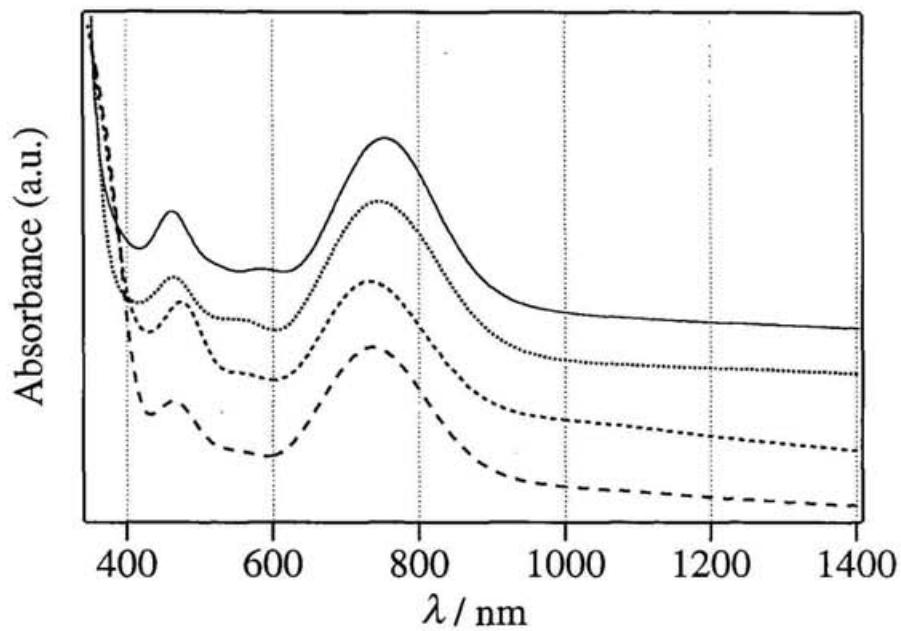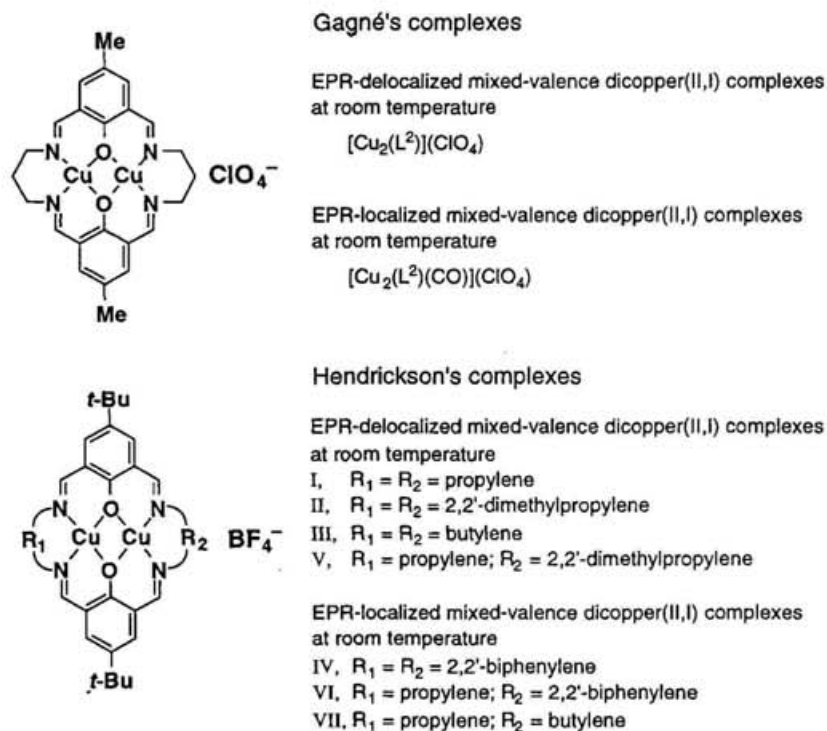
Figure 37. Electronic absorption spectra of **1–4** in the solid state (dispersed in KBr); **1** (——), **2** (·······), **3** (-------), and **4** (– – – –).
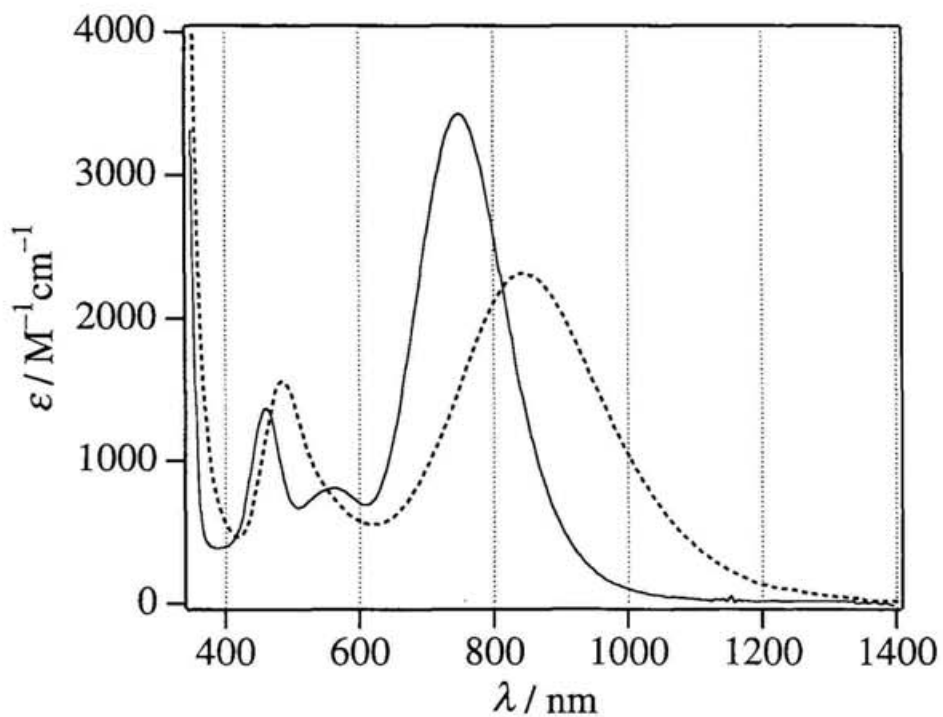
Figure 38. Electronic absorption spectra of **2** in CH_2Cl_2 (——) and DMF (-------).
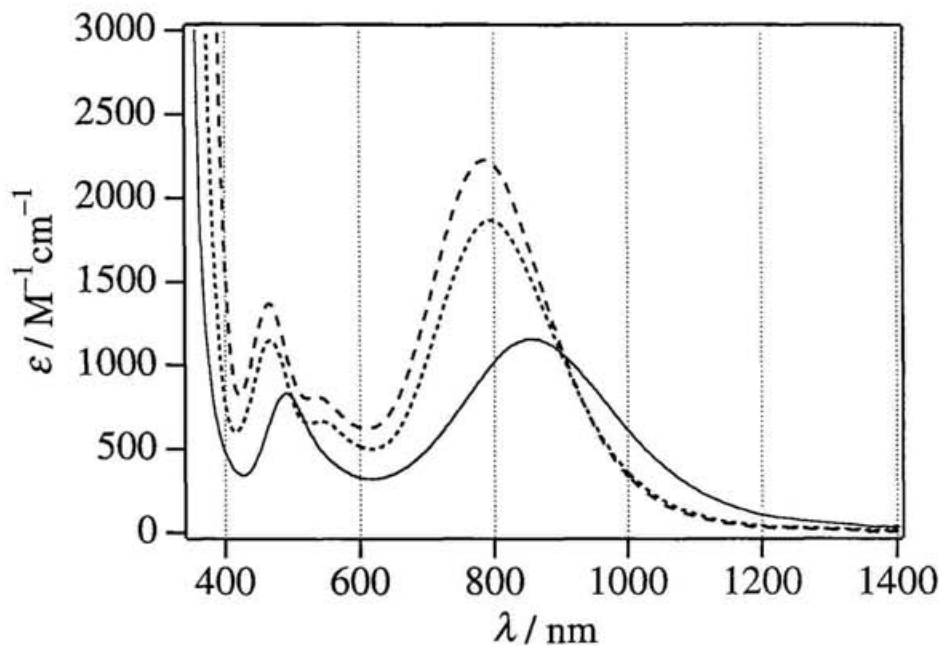
Figure 39. Electronic absorption spectra of **1**, **3**, and **4** in DMF; **1** (———), **3** (-------), and **4** (– – – –).

Gagné's complexes

EPR-delocalized mixed-valence dicopper(II,I) complexes at room temperature

$[Cu_2(L^2)](ClO_4)$

EPR-localized mixed-valence dicopper(II,I) complexes at room temperature

$[Cu_2(L^2)(CO)](ClO_4)$

Hendrickson's complexes

EPR-delocalized mixed-valence dicopper(II,I) complexes at room temperature
I, $R_1 = R_2$ = propylene
II, $R_1 = R_2$ = 2,2'-dimethylpropylene
III, $R_1 = R_2$ = butylene
V, R_1 = propylene; R_2 = 2,2'-dimethylpropylene

EPR-localized mixed-valence dicopper(II,I) complexes at room temperature
IV, $R_1 = R_2$ = 2,2'-biphenylene
VI, R_1 = propylene; R_2 = 2,2'-biphenylene
VII, R_1 = propylene; R_2 = butylene

Figure 40. Gagné's and Hendrickson's mixed-valence dicopper(II,I)–macrocycle ligand complexes.

Table 16. Electronic Absorption Spectral Data for Complexes **1–4**

complex	medium	λ_{max} / nm (ε / $M^{-1}cm^{-1}$)
1	DMF	462, 586, 754
		490 (830), 854 (1200)
2	solid	466, 555 (sh), 748
	CH_2Cl_2	460 (1400), 566 (810), 750 (3400)
	DMF	488 (1500), 846 (2300)
3	solid	476, 555 (sh), 734
	DMF	470 (1100), 544 (660), 798 (1900)
4	solid	466, 560 (sh), 738
	DMF	468 (1400), 540 (800), 790 (2200)

Mixed-Valence Analyses. The spectroscopic parameters of the IT bands for **1–4** in DMF are given in Table 17. The ground state of a mixed-valence dicopper(II,I) complex can be described by a wave function of the form of eq 1 which expresses the delocalized ground-state electronic distribution in terms of localized wave functions. The mixing coefficient is α and the delocalization parameter α^2 represents the unpaired electron density on Cu_B. The Hush equations[42] relate the intensity parameters of an IT band to α^2 and to H_{AB}, the electronic coupling integral between the two localized state.

$$\alpha^2_{opt} = 4.24 \times 10^{-4}\varepsilon_{max}E_{1/2}/(E_{max}R^2) \qquad (6)$$

$$H_{AB} = \alpha_{opt}E_{max} \qquad (7)$$

In eqs 6 and 7, ε_{max} is the molar absorptivity at the band maximum, $E_{1/2}$ is the half-with of the band, E_{max} is the energy of maximum absorption, and R is the distance in Å that the electron is transferred. In this analysis, R is taken as 2.40 Å based on Cu–Cu distances determined from X-ray analyses for **1, 3** and **4**. The values of α^2_{opt} and H_{AB} calculated from the IT parameters are given in Table 17. Solomon et al. reported the values of α^2opt of half-met-L hemocyanins derivertives (L = Cl⁻, Br⁻, and I⁻), which exhibit EPR delocalization at 77K, calculated from the IT parameters and for the most delocalized case (half-met-I⁻)

93

the value of α^2_{opt} is 2.0 x 10^{-2}.[44h] In the case of Creutz–Taube complex ion, $[(NH_3)_5Ru(III)(pyz)Ru(II)(NH_3)_5]^{5+}$, α^2_{opt} is ca. 9 x 10^{-3}.[66] The α^2_{opt} values for **1–4** are greater than that of half-met-I$^-$ and indicated that the ground state electronic interactions between the copper ions relatively strong. Creutz reported the potential energy diagrams for symmetric mixed-valence complexes (Figure 41).[65] The diagrams a, b, and c in Figure 41 correspond to Class I, II and III, respectively. Because the values of α_{opt} for **1–4** are 0.17, 0.23, 0.20, and 0.21, respectively, the potential energy diagrams for **1–4** are intermediate between b and c.

Table 17. IT Parameters and Mixed-Valence Analyses for 1–4

	1^b	2^a	2^b	3^b	4^b
E_{max} (cm^{-1})	11700	13300	11800	12500	12700
ε_{max} (M^{-1}cm^{-1})	1200	3400	2300	1900	2200
$E_{1/2}$ (cm^{-1})	4000	2800	3700	3500	3500
α^2_{opt}	3.0 x 10^{-2}	5.3 x 10^{-2}	5.3 x 10^{-2}	3.9 x 10^{-2}	4.5 x 10^{-2}
α_{opt}	0.17	0.23	0.23	0.20	0.21
H_{AB} (cm^{-1})	2000	3100	2700	2500	2700

^{a} CH$_2$Cl$_2$ solution. ^{b} DMF solution.
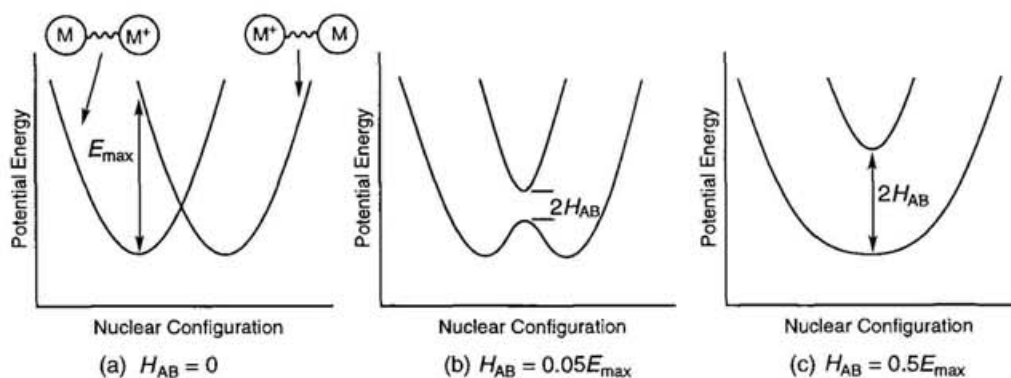
Figure 41. Potential energy diagrams for symmetric mixed-valence complexes.

2. 3. 4   Electrochemistry.

The electrochemical properties of the complexes **1–4** were studied by cyclic voltammetry and differential pulse voltammetry in DMF. The two voltammograms of **1–4** are displayed in Figures 42 and 43, respectively. The electrochemical data are summarized in Table 18.

In the case of the complex **4**, it is apparent from Figure 42 that there are two reduction processes at –0.31 and –2.00 V vs. SCE. The first reduction process is reversible, while the second process is irreversible. Controlled-potential electrolysis of **4** in DMF at –0.22 V vs. SCE (n=1.0) yields a dark yellowish brown solution which is EPR-silent. Therefore, the first wave is assigned to $Cu_2(II,I)/Cu_2(I,I)$ process. The second reduction peak at –2.00 V vs. SCE is assigned to the ligand-based reduction in comparison with the reduction potential of the free ligand HL4. When scanning to positive potentials is undertaken, the complex **4** shows one irreversible oxidation process which is tentatively assigned to $Cu_2(II,I)/Cu_2(II,II)$ process. A similar redox behavior was observed for **3** (see Figure 42). The cyclic voltammogram of **2** is also shown in Figure 42. The complex **2** displays one quasi-reversible reduction process and one irreversible reduction peak corresponding to the $Cu_2(II,I)/Cu_2(I,I)$ process and ligand-based reduction at –0.14 and –1.79 V vs. SCE, respectively. The oxidation wave corresponding to $Cu_2(II,I)/Cu_2(II,II)$ process was not observed. The cyclic voltammogram of **1** in Figure 42 indicates two irreversible reduction processes at –0.06 and –1.91 V vs. SCE. The first and second reduction peaks are assigned to the $Cu_2(II,I)/Cu_2(I,I)$ process and ligand-based reduction, respectively. The oxidation wave corresponding to $Cu_2(II,I)/Cu_2(II,II)$ process was not observed. The observed cyclic voltammograms of **1–4** reveal no evidence for the formation of a stable $Cu_2(II,II)$ spices.

The stability of the mixed-valence dicopper(II,I) species is related to the conproportionation constant K_{con} for the following equilibrium.

$$[Cu_2(II,II)] + [Cu_2(I,I)] \xrightleftharpoons{K_{con}} 2[Cu_2(II,I)]$$
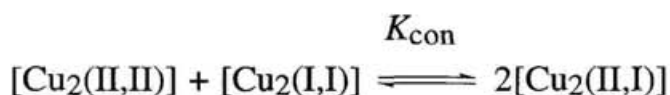
The K_{con} values of the equilibrium can be determined electrochemically using the equation log $K_{con} = (E_1 - E_2)/0.0591$ at 25 °C. The irreversibility of Cu$_2$(II,I)/Cu$_2$(II,II) process does not permit precise determination of the K_{con} value. However, the K_{con} values of **3** and **4** have been roughly evaluated using the $E_{1/2}$ values estimated from differential pulse voltammograms for the irreversible Cu$_2$(II,I)/Cu$_2$(II,II) process. The K_{con} values obtained for **3** and **4** are 1×10^{10} and 1×10^{11}, respectively. These values are comparable to those obtained for the dicopper–macrocycle complexes ($K_{con} = 10^6$–10^{13})[44b,44d,60] and indicate that the mixed-valence dicopper(II,I) species is highly stabilized. The stabilization of the dicopper(II,I) species seems to be ascribable to the electron delocalization over the dinuclear unit through the direct copper–copper interaction, the π back-donation from the filled d orbitals of Cu(I) to the antibonding orbitals of ligand, and/or the steric constraint of the dinuclear tridentate ligand upon the copper coordination geometry.

Table 18. Electrochemical Data of Complexes **1–4** and Ligands HL1–HL4[a]

| Compound | Cu$_2$(II,I)/Cu$_2$(II,II) | | Cu$_2$(II,I)/Cu$_2$(I,I) | | | | |
	E_{pa}^b	$E_{1/2}^{1\,b}$	E_{pa}^b	E_{pc}^b	$E_{1/2}^{2\,b}$	E_{pc}^b	K_{con}^e
1				-0.06[c]		-1.91[c]	
2			-0.04	-0.14	-0.09	-1.79[c]	
3	+0.46[c]	+0.37[d]	-0.18	-0.26	-0.22	-1.92[c]	1x10^{10}
4	+0.49[c]	+0.38[d]	-0.22	-0.31	-0.27	-2.00[c]	1x10^{11}
HL1						-1.54[c]	
HL2						-1.59[c]	
HL3						-1.72[c]	
HL4						-1.80[c]	

[a] All cyclic and differential pulse voltammograms were recorded in DMF using a glassy-carbon electrode at a scan rate of 100 and 5 mV s^{-1}, respectively. [b] Potentials are given in volts vs. SCE. [c] Peak potentials for an irreversible process. [d] $E_{1/2}$ value is estimated from differential pulse voltammograms. [e] Conproportionation constant.
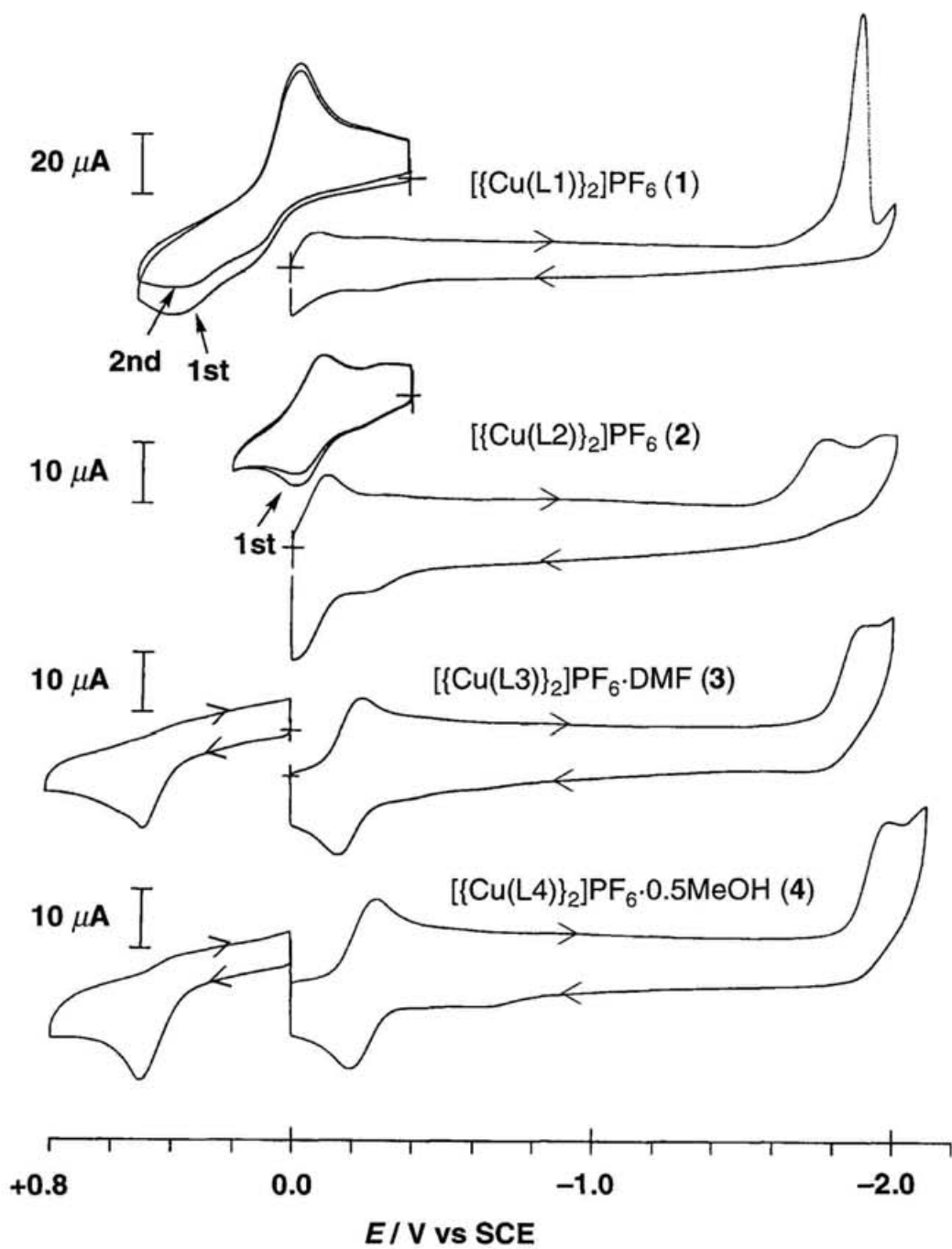
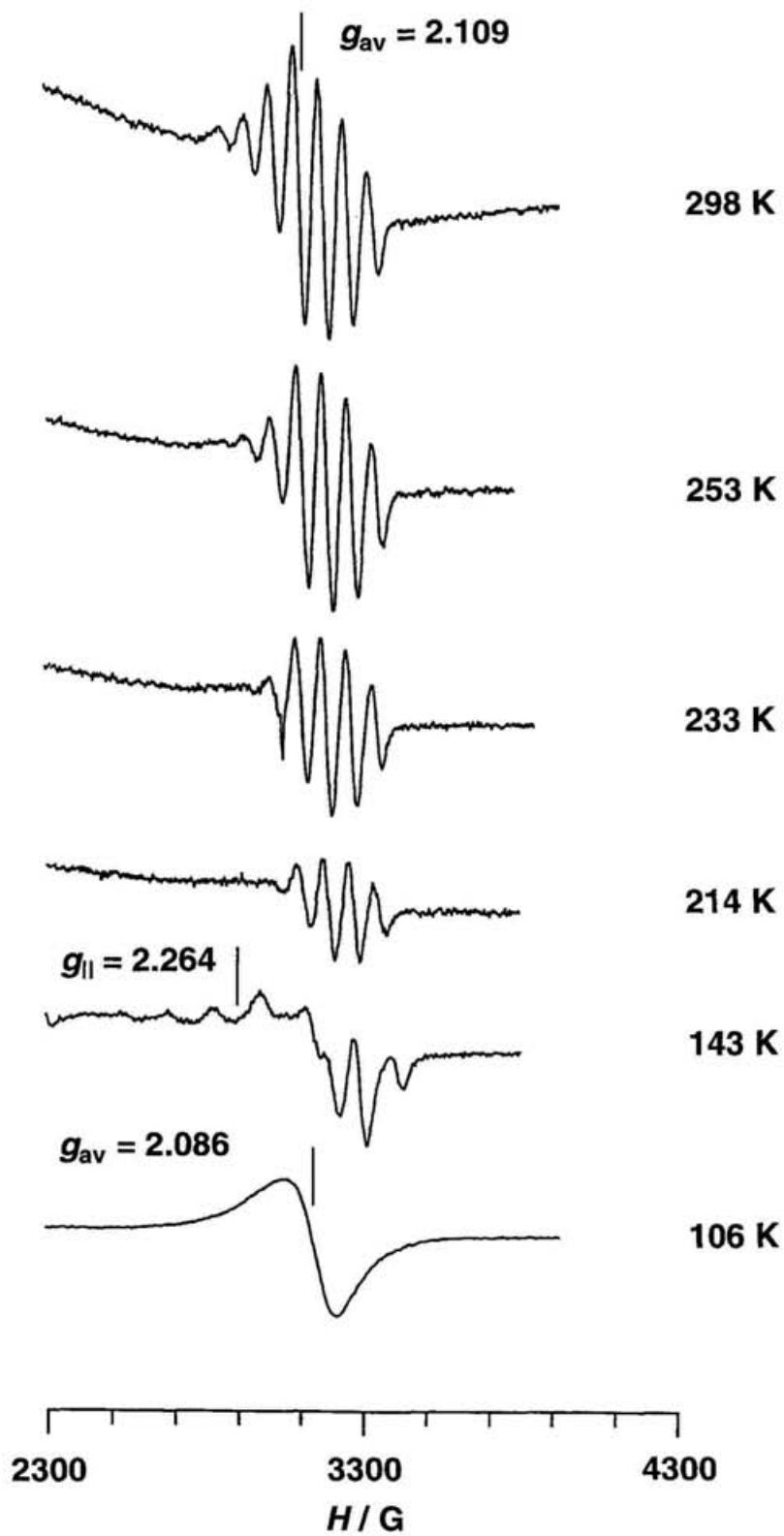**Figure 42.** Cyclic voltammograms of complexes **1–4** in DMF at scan rate 100 mV s^{-1} .

97
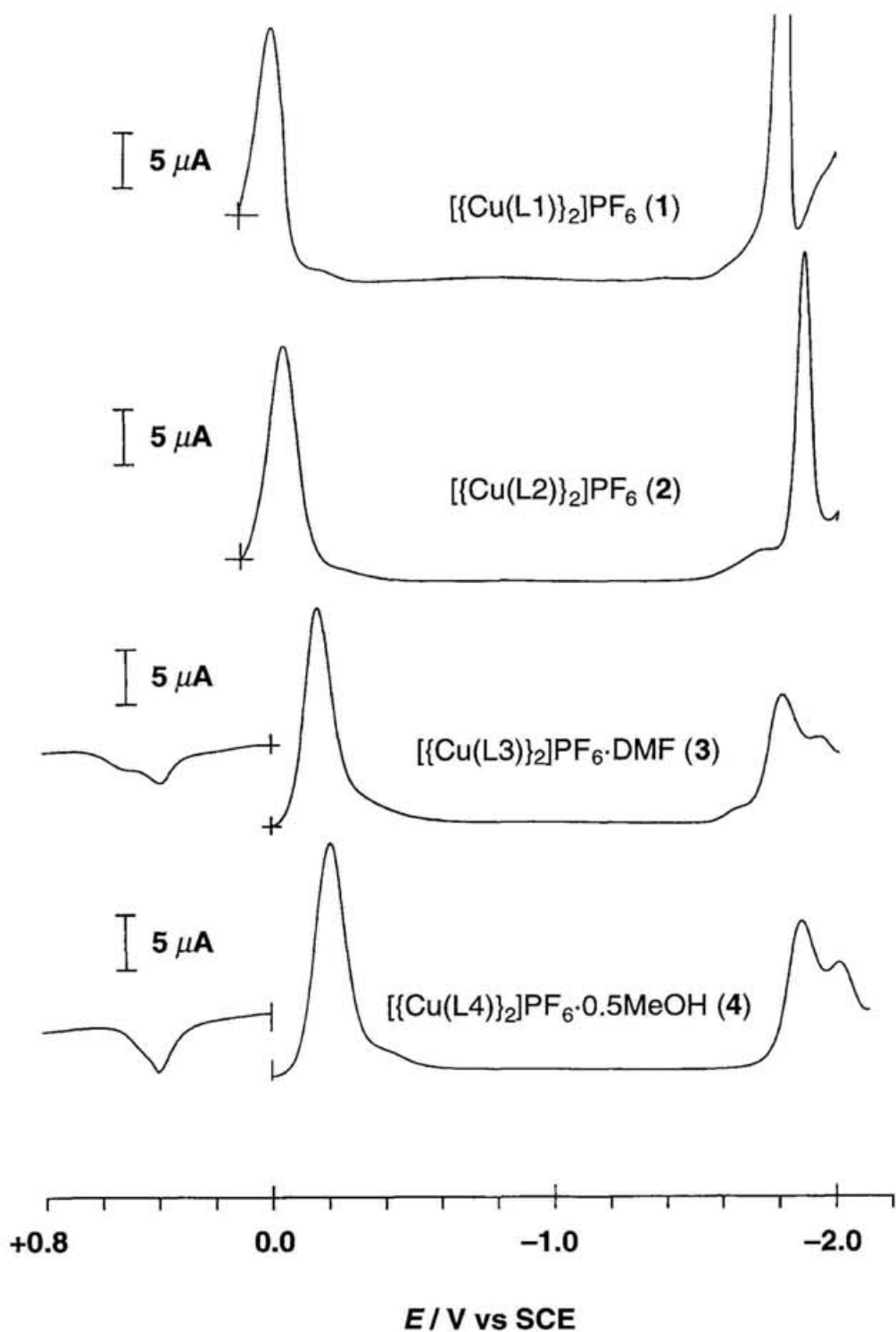
Figure 43. Differential pulse voltammograms of complexes **1–4** in DMF at scan rate 5 mV s^{-1} and modulation amplitude 50 mV.

2. 3. 5 EPR Spectra.

Variable-temperature X-band EPR spectra in CH_2Cl_2 were measured for complex **2**. Insolubility of complexes **1, 3**, and **4** in that solvent prevented EPR measurement. Therefore, the variable-temperature X-band EPR spectra for **1, 3**, and **4** were examined in DMF together with those of complex **2**. EPR parameters for **1–4** are given in Table 19.

The spectra of **2** in CH_2Cl_2 are given in Figure 44. At 298 K, the complex **2** shows an isotropic pattern with seven copper hyperfine lines ($A_{av} = 74.4 \times 10^{-4}$ cm^{-1}) centered at $g_{av} = 2.109$, consistent with the interaction of the unpaired electron with both copper centers ($I = 3/2$). The unpaired electron of **2** is delocalized on the EPR time scale (10^{-8}–10^{-4} s^{-1}) at room temperature. As lowering temperature, the low-field components of the seven-line pattern have coalesced in turn. In a frozen glass (143 K) of CH_2Cl_2, the complex **2** exhibits axial spectra with four-line copper hyperfine imposed on the $g_\parallel$ signal, which is due to localization of the unpaired electron at a single copper site. The copper hyperfine splitting ($A_\parallel$) on the $g_\parallel$ signal is found to be 137×10^{-4} cm^{-1}. At 106 K, the spectrum exhibits a single symmetrical line centered at $g_{av} = 2.086$. The origin for this broadening is unclear.

Several mixed-valence dicopper(II,I) complexes which show temperature-dependent seven-line EPR spectra have been reported so far. Gagné et al. reported such a complex, $[Cu_2(L^2)](ClO_4)$, in 1977,[44a] and Hendrickson's group reported four related complexes I, II, III, and V in 1983 (see Figure 40).[44d] At room temperature in solution, these complexes show seven-line copper hyperfine spectra. In the low-temperature glass medium, each complex shows the spectrum characteristic of the single unpaired electron localized on one copper center. These EPR-delocalized complexes in which the electron delocalization occurs via a bridging ligand show the average copper hyperfine splitting (A_{av}) of 37×10^{-4}–41.77×10^{-4} cm^{-1}, which is approximately one-half of the splitting usually found for mononuclear copper(II) complexes (72×10^{-4}–98×10^{-4}).[55] However, the A_{av} value of **2** is 74.4×10^{-4} cm^{-1} which is compared to those found for mononuclear copper(II) complexes. While Barr et al.[45b] reported that the room

$g_{av} = 2.109$

298 K

253 K

233 K

214 K

$g_{\|} = 2.264$

143 K

$g_{av} = 2.086$

106 K

2300   3300   4300

H / G

Figure 44. Variable-temperature X-band EPR spectra for complex **2** in CH$_2$Cl$_2$.

100

temperature solution EPR spectrum of the $[Cu_2(L^5)]^+$ (see Figure 2) displays an isotropic 7-line signal (9.46 GHz, CHCl$_3$, 300 K, g_{av} = 2.12, A_{av} = 75x10^{-4} cm^{-1}) which arises from direct electron transfer between the two copper centers. The similarity in A_{av} value between the complex 2 and Barr's complex suggests that the 7-line signal for 2 is attributable to the direct electron transfer between two copper centers.

So reported the simulation of temperature-dependent EPR spectra of Gagné's and Hendrickson's complexes,[62] and found that spectral changes of these complexes are very sensitive to the transition probability of the electron from one copper atom to the other. The transition probability makes the two low-field components of the seven hyperfine line coalesce. The coalescence observed for 2 seems to be ascribable to the decrease in the transition probability on lowering temperature. Hendrickson et al. also reported the variable-temperature EPR spectra for the three EPR-localized mixed-valence dicopper(II,I) complexes IV, VI, and VII (see Figure 40).[44d] These spectra illustrate the influence of the rate of molecular tumbling upon the appearance of the spectrum. With lowering temperature the molecular tumbling becomes slower so that two low-field components of the four-line pattern are broadened near 230 K and cannot be resolved. Therefore, it is hard to estimate the temperature at which the complex 2 changes from EPR-delocalized to EPR-localized state in solution based on hyperfine splitting pattern or A_{av} value.
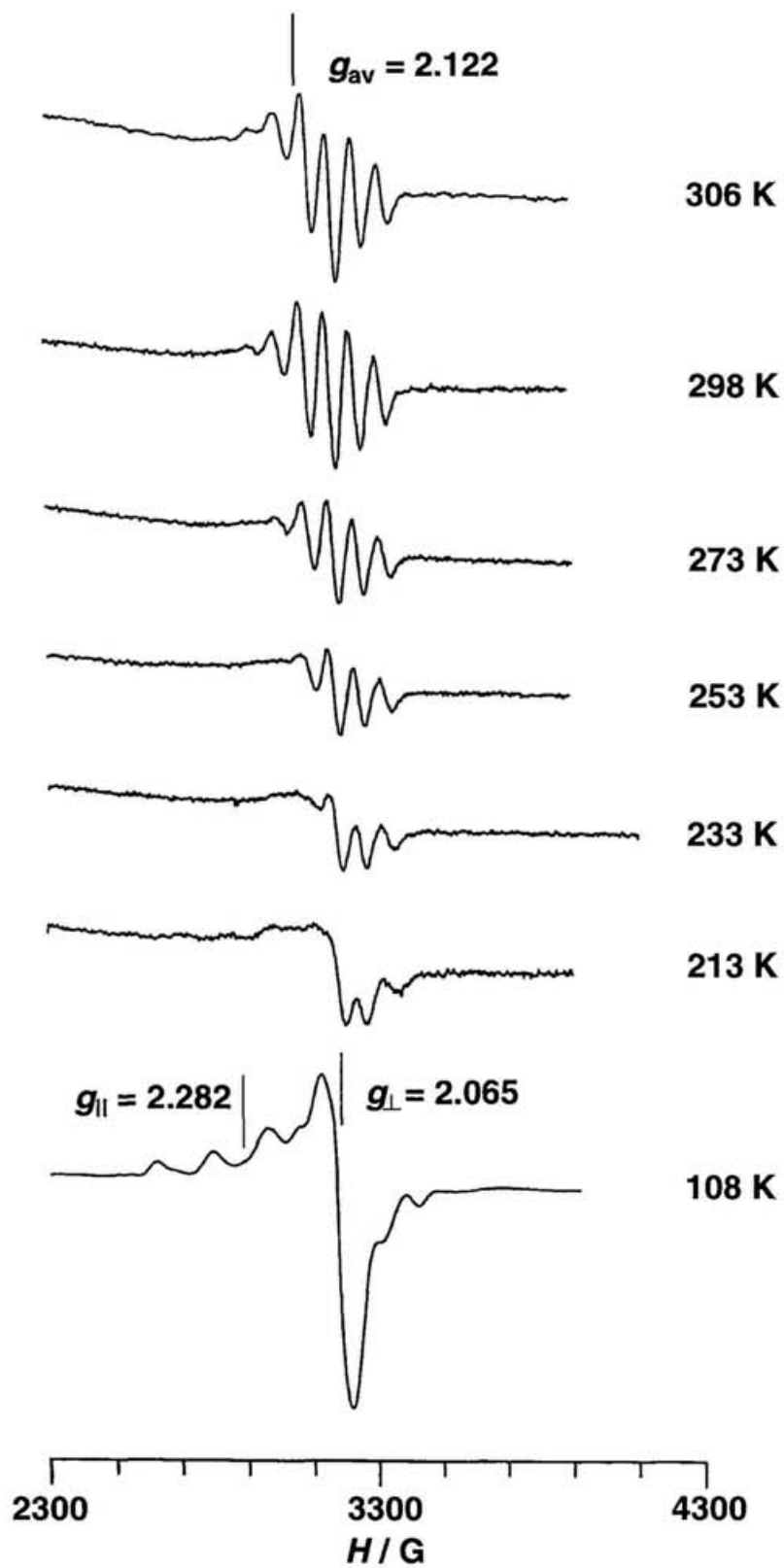
The spectra of 2 in DMF are summarized in Figure 45. At 302 K, the complex 2 displays a seven-line pattern (A_{av} = 72.9x10^{-4} cm^{-1}, g_{av} = 2.120) in which the most low-field component of the seven-line pattern is broadened. The basis for seven-hyperfine pattern is supported by the g_{av} value close to that observed for 2 in CH$_2$Cl$_2$ (g_{av} = 2.109). The seven-line hyperfine pattern indicates the interaction of the unpaired electron with both copper centers. So also reported that the transition probability which makes the two low-field components of the seven hyperfine line coalesce is dependent on the solvent.[62] Therefore the broadening for 2 are attributable to the nonequivalence of two copper ions caused by preferential ligation of weakly coordinating DMF molecules to either Cu(II) or Cu(I) ion. As lowering temperature, the low-field components
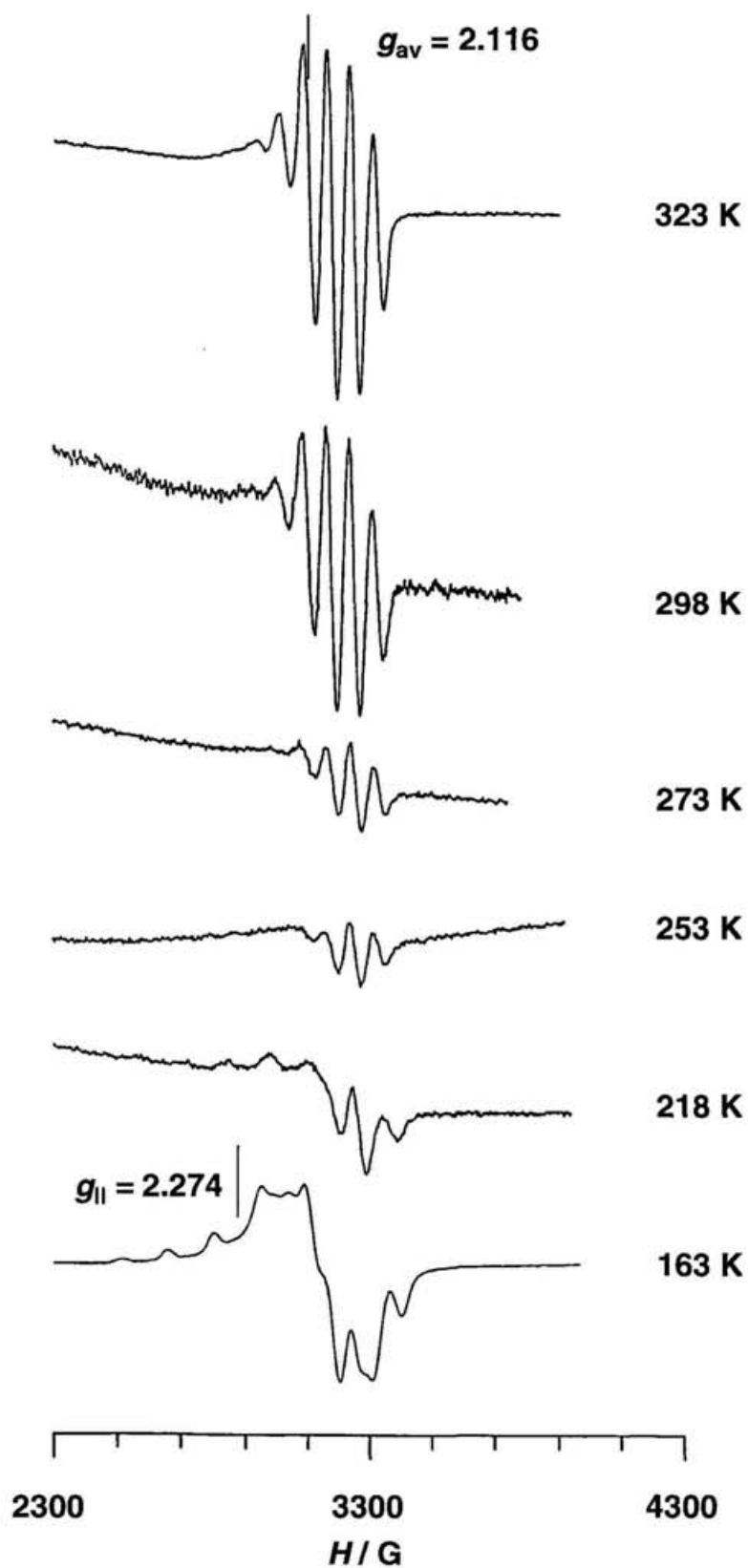
101
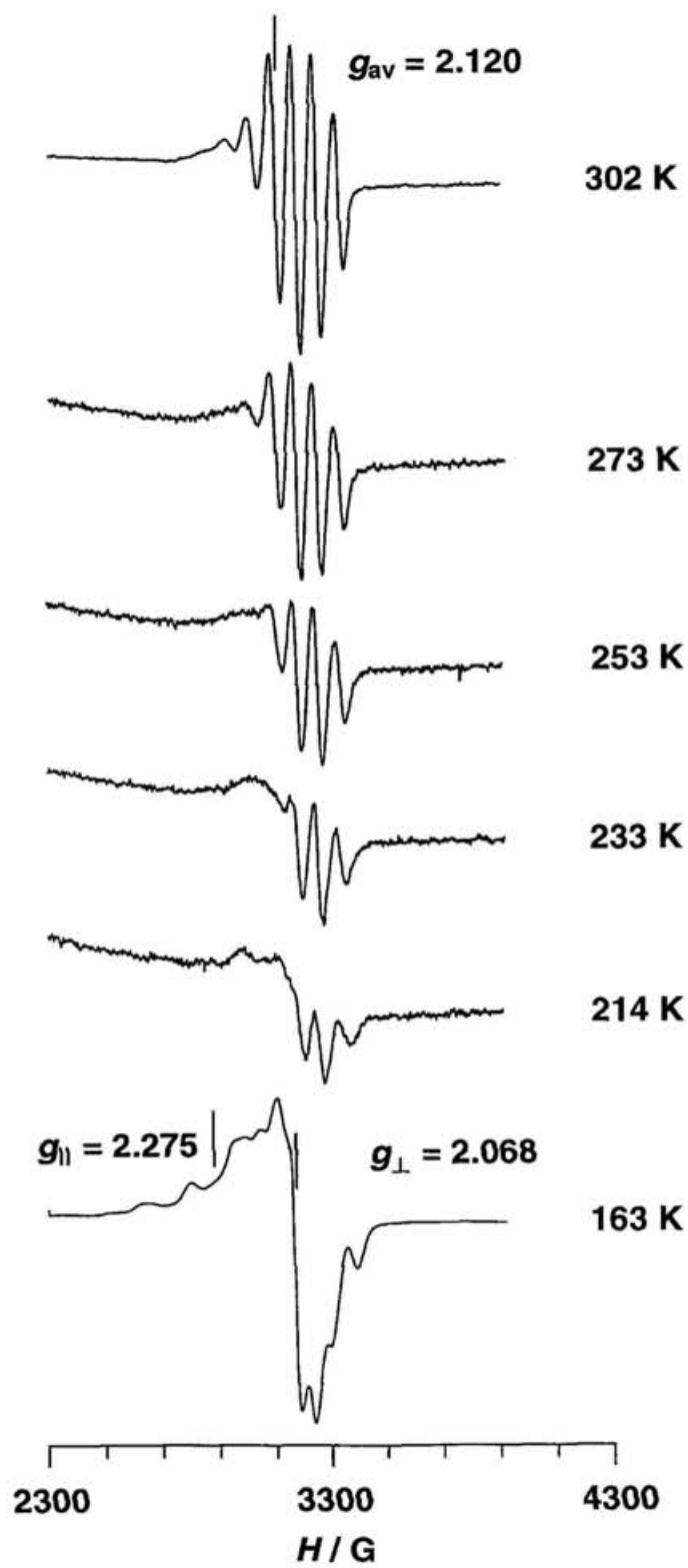
Figure 45. Variable-temperature X-band EPR spectra for complex **2** in DMF.

of the seven-line pattern have coalesced in turn. In a frozen glass (163 K) of DMF, the complex **2** exhibits axial spectra with four-line copper hyperfine imposed on the $g_\parallel$ signal, which suggests the localization of the unpaired electron on one copper site. The observed $A_\parallel$ and $g_\parallel$ values are 141×10^{-4} cm^{-1} and 2.275, respectively.
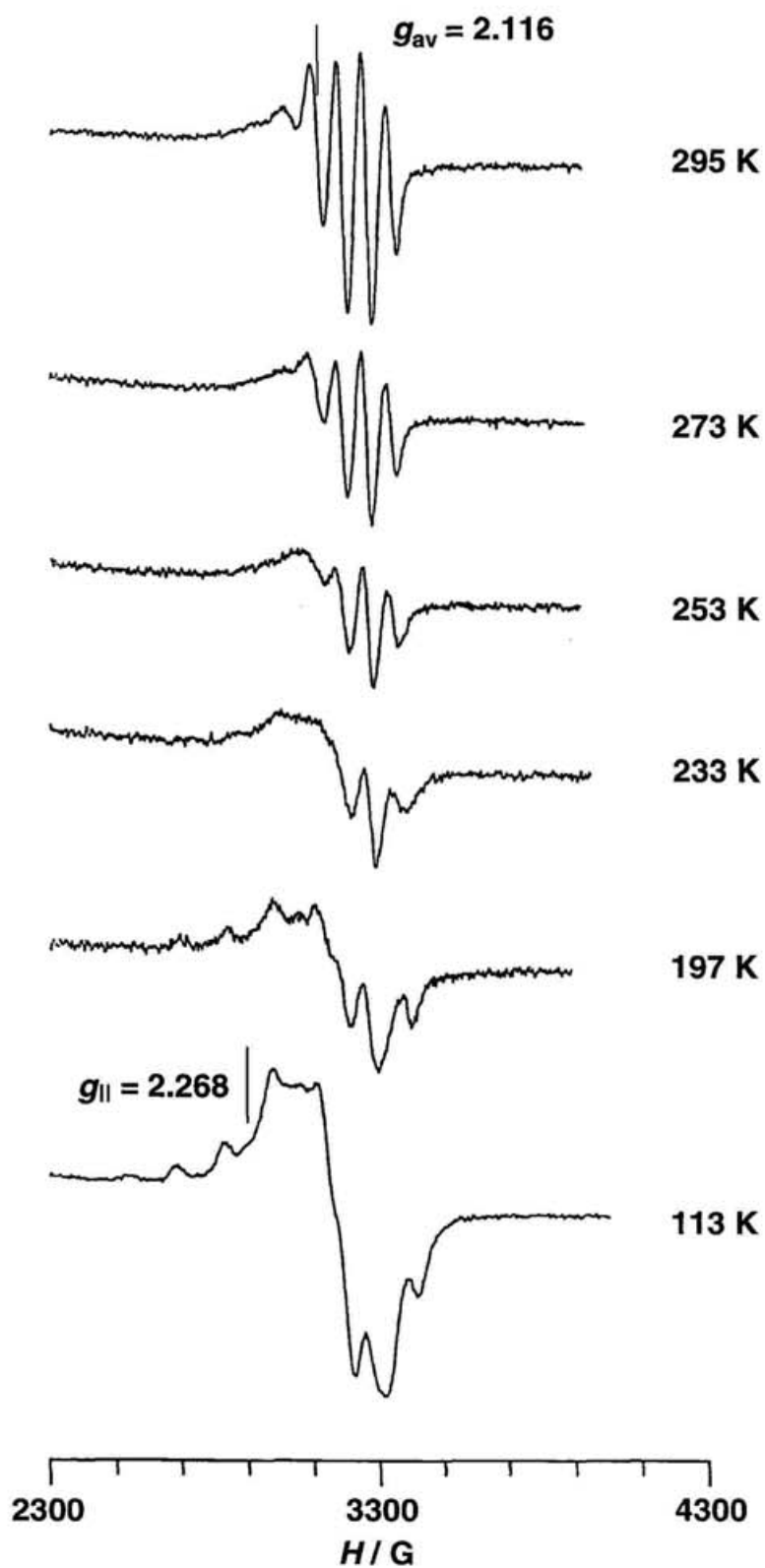
The variable-temperature EPR spectra for the complexes **1**, **3**, and **4** in DMF are summarized in Figures 46–48. Each complex shows the temperature-dependent EPR spectra similar to those observed for **2** in DMF. The DMF solution spectra of **1** (at 306 K), **3** (at 323 K), and **4** (at 295 K) show the seven-hyperfine lines ($A_{av} = 73.0 \times 10^{-4}$ cm^{-1}, $g_{av} = 2.122$ for **1**, $A_{av} = 70.2 \times 10^{-4}$ cm^{-1}, $g_{av} = 2.116$ for **3**, and $A_{av} = 72.3 \times 10^{-4}$ cm^{-1}, $g_{av} = 2.116$ for **4**) in which one or two low-field components of the seven-line pattern were broadened. The bases for seven-hyperfine pattern are supported by the g_{av} values close to that observed for **2** in CH$_2$Cl$_2$ ($g_{av} = 2.109$). These broadenings are attributable to the nonequivalence of two copper ions caused by preferential ligation of weakly coordinating DMF molecules to either Cu(II) or Cu(I) ion. These seven-line hyperfine patterns indicate the interaction of the unpaired electron with both copper centers. As lowering temperature, the low-field components of the hyperfine line have coalesced in turn. In a frozen glass of DMF, **1** (at 108 K), **3** (at 163 K), and **4** (at 113 K) each exhibits axial spectra with four-line copper hyperfine imposed on the $g_\parallel$ signal, which suggests the localization of the unpaired electron on one copper site. The $A_\parallel$(Cu) values observed for **1**, **3**, and **4** are 153×10^{-4} cm^{-1}, 134×10^{-4} cm^{-1}, and 134×10^{-4} cm^{-1}, respectively. From these temperature-dependent EPR spectra, all the complexes are classified into Class II type mixed-valence dicopper(II,I) complex.

Figure 46. Variable-temperature X-band EPR spectra for complex **1** in DMF.

$g_{av} = 2.116$

323 K

298 K

273 K

253 K

218 K

$g_{\parallel} = 2.274$

163 K

2300   3300   4300

H / G

Figure 47. Variable-temperature X-band EPR spectra for complex **3** in DMF.

105

$g_{av} = 2.116$

295 K

273 K

253 K

233 K

197 K

$g_{\parallel} = 2.268$

113 K

2300   3300   4300

H / G

Figure 48. Variable-temperature X-band EPR spectra for complex **4** in DMF.

106

Table 19. X-Band EPR Parameters for Complexes **1–4**

complex	medium	T / K	$g\perp$	g_{av}	$g_{\parallel}$	A_{av} / 10^{-4} cm^{-1}	$A_{\parallel}$ / 10^{-4} cm^{-1}
1	DMF	306		2.122		73.0	
		108	2.065		2.282		153
2	CH$_2$Cl$_2$	298		2.109		74.4	
		143			2.264		137
		106		2.086			
	DMF	302		2.120		72.9	
		163	2.068		2.275		141
3	DMF	323		2.116		70.2	
		163			2.274		134
4	DMF	295		2.116		72.3	
		113			2.268		134

2. 3. 6 XPS Spectra.

XPS spectra of complexes **1–4** were measured in the region 950–925 eV showing the primary Cu $2p_{3/2}$ photolines and associated satellite structure at 298 and 165 K. The spectra of **1–4** at 298 K are very similar each other and show no temperature dependence. Spectral data for **1–4** are given in Table 20. The spectra for **1–4** at 298 K are shown in Figure 49.

The spectra of **1–4** show high intensity Cu $2p_{3/2}$ peak in the region 932.64–933.62 eV and weak intensity Cu $2p_{3/2}$ peak in the region 935.10–936.34 eV, which are assigned to Cu(I) and Cu(II) oxidation state, respectively. Gagné et al. reported the XPS spectra of two mixed-valence dicopper(II,I) complexes, [Cu$_2$(L^2)](ClO$_4$) and [Cu$_2$(L^2)(CO)](ClO$_4$) (see Figure 40), which show two Cu $2p_{3/2}$ peaks of nearly equal intensity.[63] However, the intensity of the Cu $2p_{3/2}$ peak of Cu(II) oxidation state for **1–4** is very weak compared with that of Cu(I). As one possibility, this is thought to be due to reduction of higher oxidation state by X-ray photoelectron. The prolonged exposure (ca. 60 min) of the sample to X-

ray flux caused the appearance of Cu 2p3/2 peak characteristic of Cu(0), together with the decrease in the Cu 2p3/2 peak of Cu(II) oxidation state (see Figure 50). However, we monitored the spectral change of **1–4** and all spectra were recorded for 10 min in which no spectral change is observed. The origin of this has been left unsolved. For **1–4**, the appearance of the characteristic Cu(II) satellite structure around 945 eV also suggests that these complexes contain Cu(II) oxidation state. These results argue that these complexes are mixed-valence dicopper(II,I) complexes. However, the appearance of two sets of Cu 2p3/2 peaks near the binding energies of isolate Cu(II) and Cu(I) species suggests that these complexes do not have delocalized ground state as shown Figure 41 (c) in the XPS time scale (ca. 10^{-17} s).

Table 20. XPS Spectral Data for Complexes **1–4**

complex	T / K	binding energies, eV[a,b]	
		Cu 2p3/2	
1	298	935.10 (2.21)	932.64 (2.47)
	165	935.29 (2.16)	932.64 (2.22)
2	298	936.34 (1.80)	933.62 (2.04)
	165	936.15 (2.06)	933.48 (2.00)
3	298	936.07 (1.52)	933.49 (2.01)
	165	936.07 (2.07)	933.27 (2.09)
4	298	936.32 (1.90)	933.29 (1.81)
	165	935.64 (2.12)	933.19 (2.12)

[a] Full width half-maximum values (fwhm) for Cu 2p3/2 are given in parentheses. [b] These values were corrected vs C1s peak using a value of 284.34 eV for C1s peak.
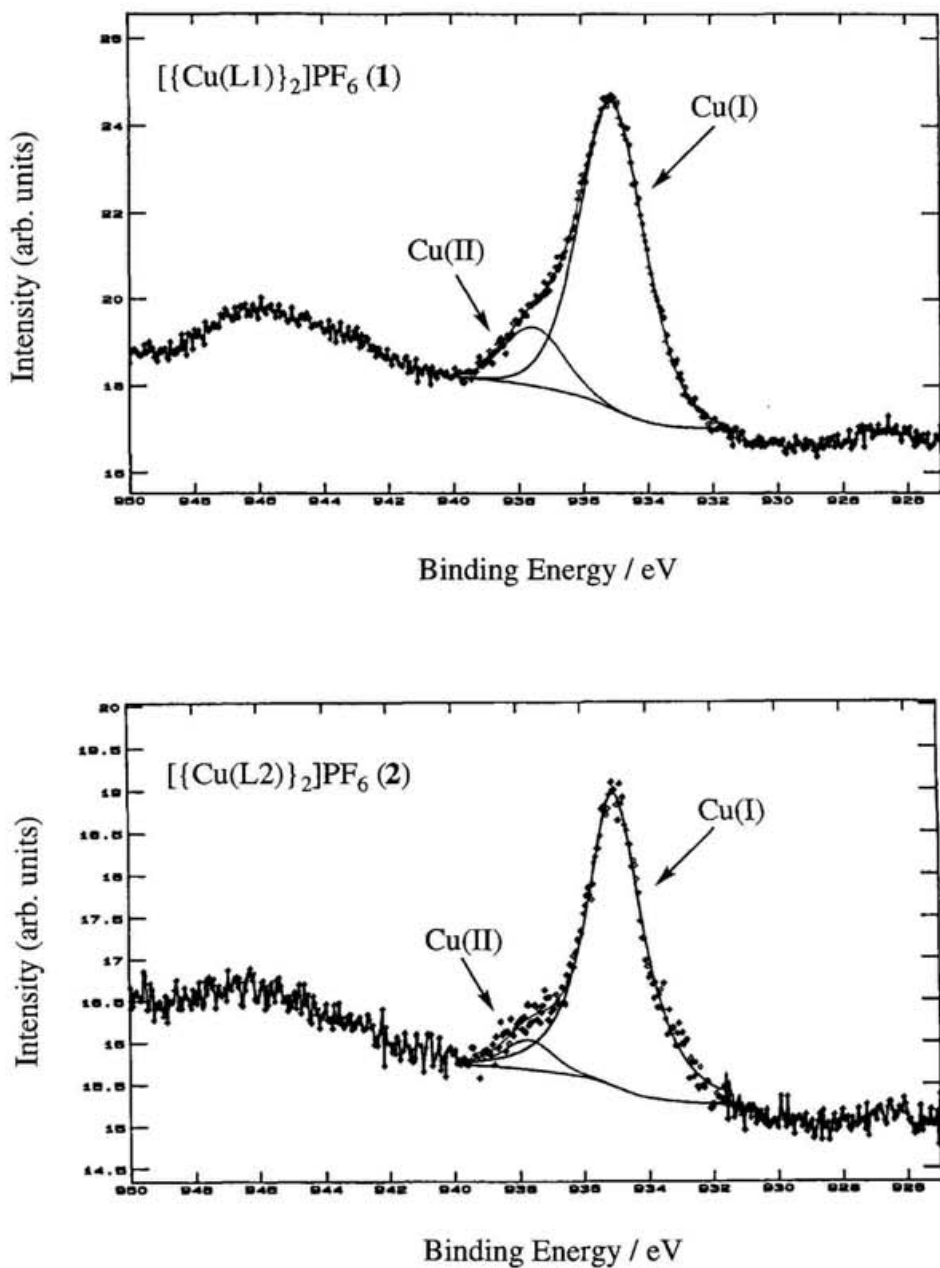
Figure 49. XPS spectra of complexes **1–4** in the region of 950–925 eV at 298 K showing the primary Cu 2p₃/₂ photolines and associated satellite structure. All spectra were recorded for ca. 10 min.
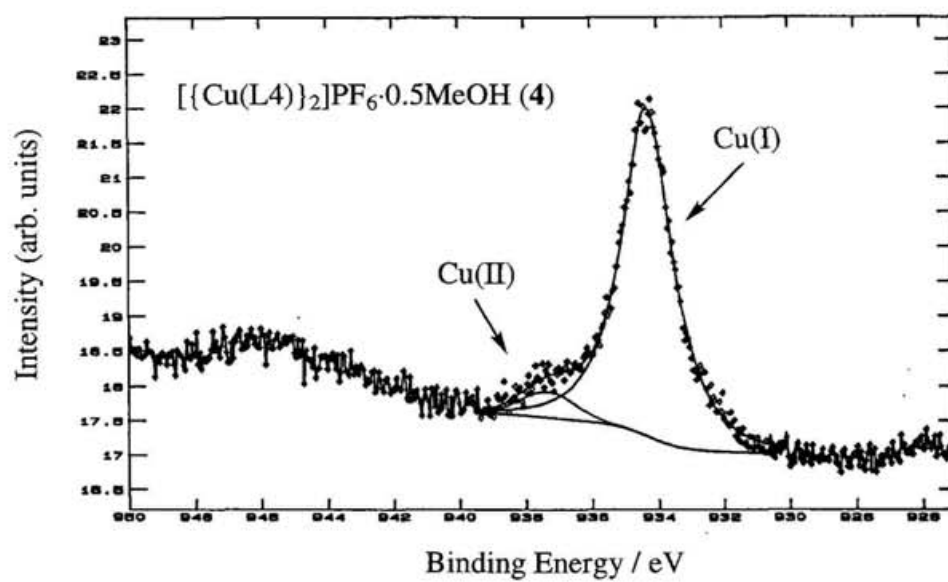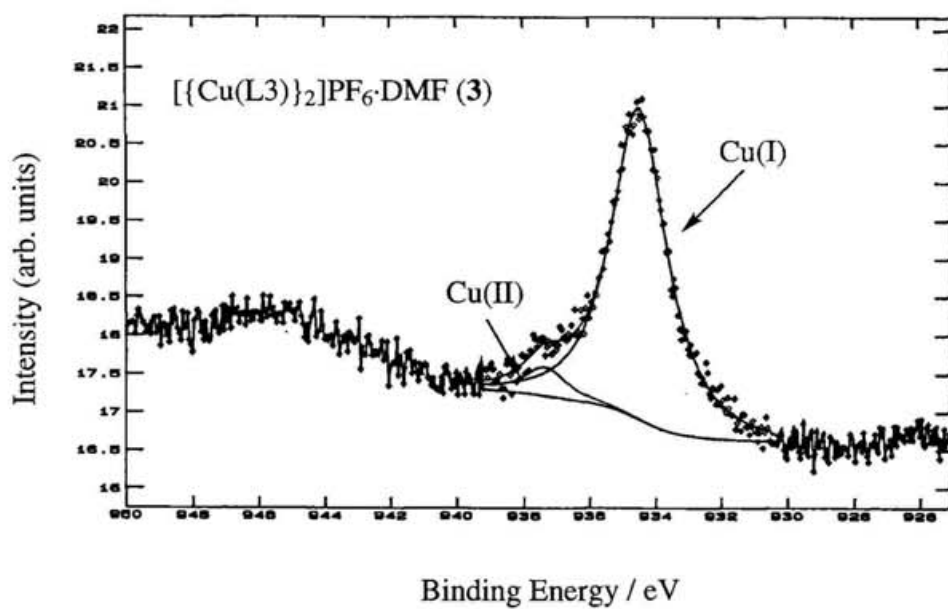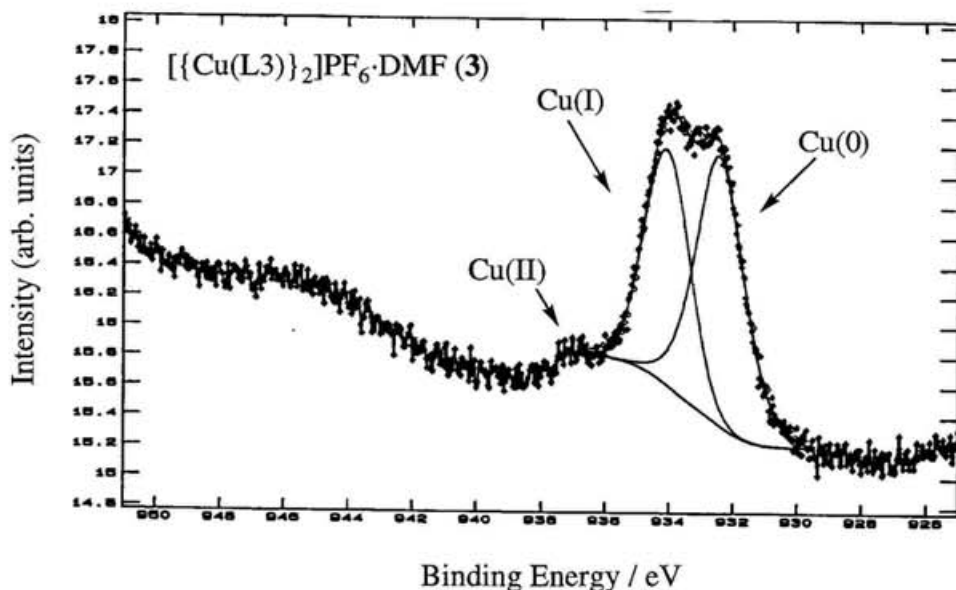
109

Figure 49. (Continued).

110

Figure 50. XPS spectrum of complex **3** in the region of 950–925 eV at 298 K showing the primary Cu $2p_{3/2}$ photolines and associated satellite structure. Spectrum was recorded for ca. 60 min.
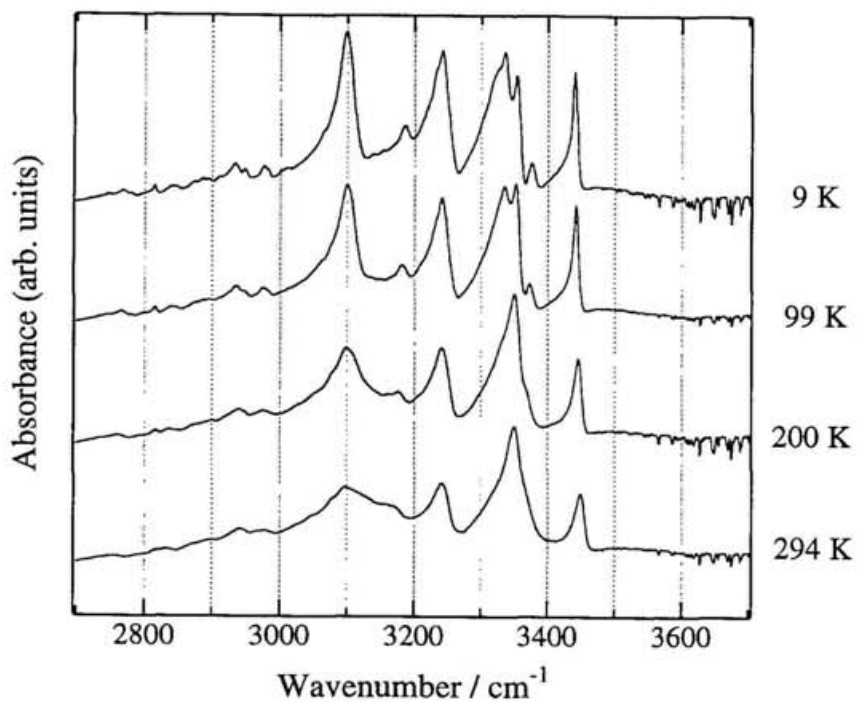
2. 3. 7 IR Spectra.

If the conversion from the delocalized state to the localized state occurs with a decrease in temperature, there is the possibility of proton transfer accompanying the localization of delocalized electron. In order to obtain the information on the vibrational states of the proton, the temperature dependences of the IR spectra for the complexes **3** and **4** were measured.

On lowering the temperature, the spectra for **3** in the region of 1630–1700 cm^{-1} show a little spectral change (Figure 51) and two new absorption bands appear at 3350 cm^{-1} and 3375 cm^{-1}, respectively (Figure 52). However, no noticeable change of the spectrum which is attributable to proton transfer was observed for **3**.

The spectra for **4** in the frequency regions of 1300–1700 cm^{-1} (Figure 53) and 2700–3700 cm^{-1} (Figure 54) are essentially unchanged with a decrease in the temperature. Thus, the results of the IR spectra suggest that the proton transfer would not occur in **4**.
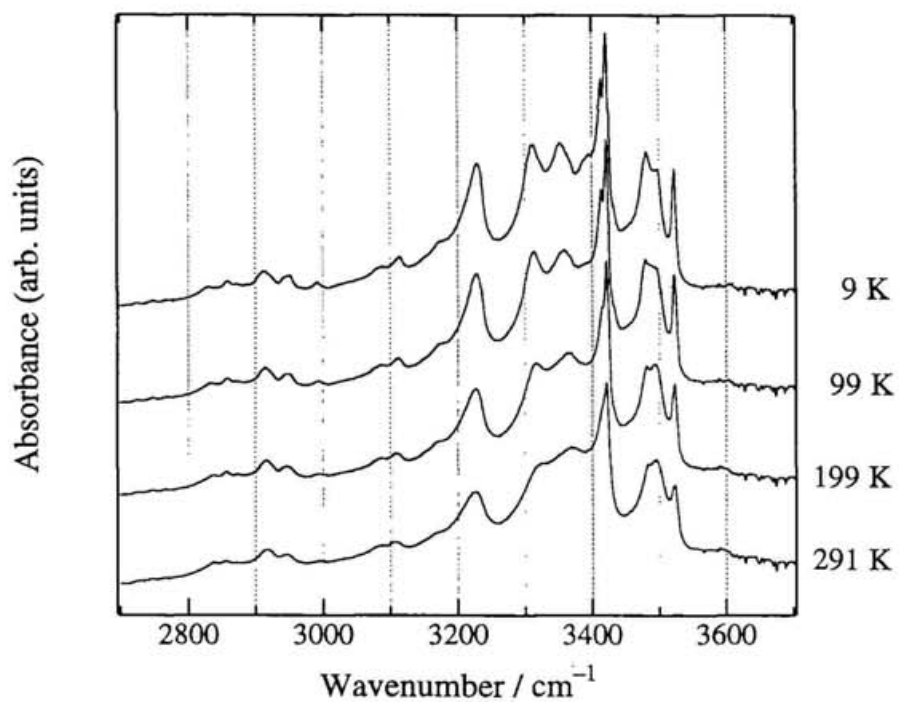
111
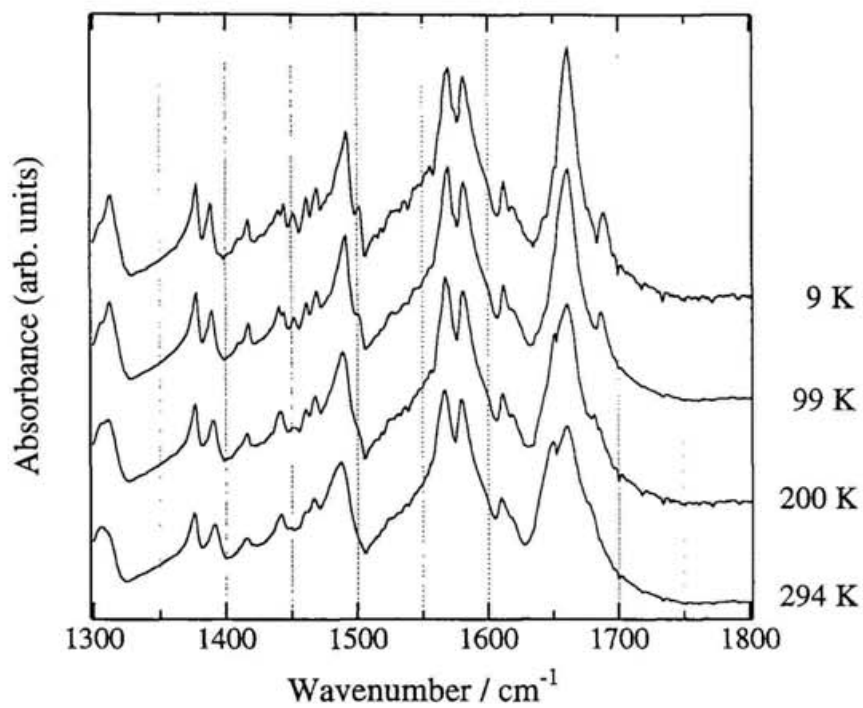
Figure 51. Temperature dependence of IR spectra for complex **3** in the region of 1300–1800 cm^{-1}.

Figure 52. Temperature dependence of IR spectra for complex **3** in the region of 2700–3700 cm^{-1}.

112
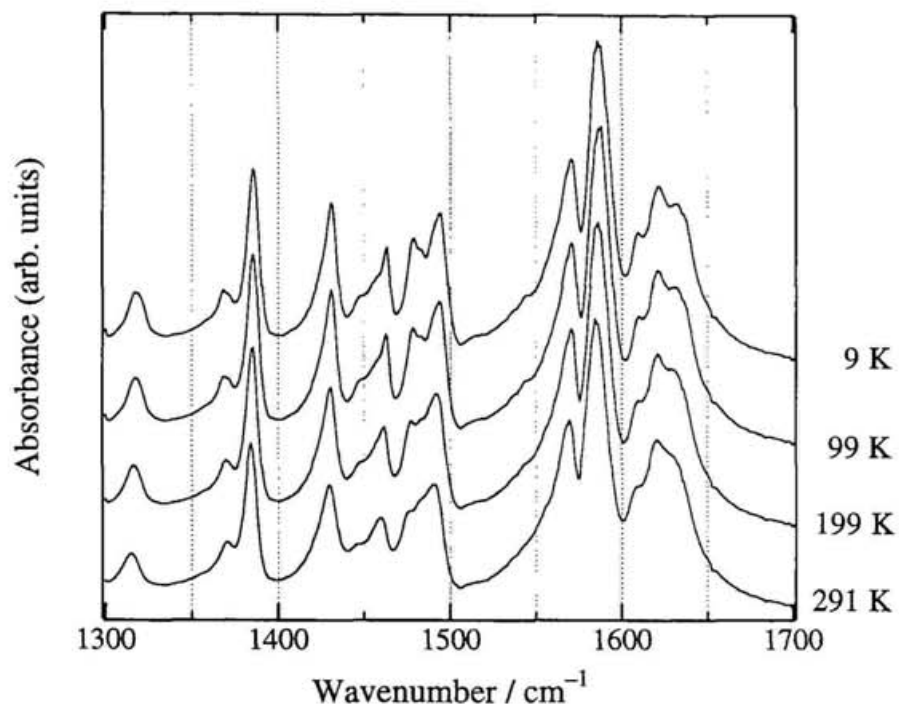
Figure 53. Temperature dependence of IR spectra for complex **4** in the region of 1300–1700 cm^{-1}.

Figure 54. Temperature dependence of IR spectra for complex **4** in the region of 2700–3700 cm^{-1}.

113

2. 4 Conclusion and Perspectives

The complexes **1–4** were successfully prepared from a mixture of $Cu(PF_6)_2$ and $[Cu(MeCN)_4]PF_6$ using the dinucleating tridentate ligands, HL1–HL4.

X-ray crystal structure analyses reveal that the complex cation of **1** and **3** are essentially planar, while that of **4** is non-planar due to the dimerization. The Cu–Cu distances of these complexes are ca. 2.40 Å, which is short enough to suggest the possibility of some overlap of metal orbitals. The complex cations of **3** are stacked in an infinite column with the alternated distances of 3.06 and 3.18 Å, respectively. The columns are further connected via intermolecular N–H⋯N type H-bonds. The dimer units of **4** form an infinite stack in the direction of the *a*-axis. ZINDO calculations of **1** and **3** using the geometry obtained from the crystal structure indicate that the SOMO of **1** and **3** is mainly composed of Cu $d_{x^2-y^2}$–Cu $d_{x^2-y^2}$ σ^* combination and the Wyberg bond indexes of Cu–Cu in **1** and **3** are 0.35, which suggests the presence of the copper–copper bond.

The complexes **1–4** exhibit a variety of magnetic properties in agreement with that these complexes are mixed-valence dicopper(II,I) complex. The complex **1** exhibits a Curie-like magnetic behavior. The complex **2** shows the one-dimensional Heisenberg magnetic behavior which suggests that the complex cations are aligned at equal spaces and presumably form the stacked column structure. The complex **3** exhibits very weak ferromagnetic interaction. Magnetic behavior of **4** reveals an intradimer antiferromagnetic interaction with a spin singlet ground state, which is consistent with the dimerization of the cations in the solid state.

Electronic spectra of **1–4** exhibit an absorption in the solid state (in the region of 734–754 nm) and in DMF solution (in the region of 790–854 nm, ε_{max} ca. 1200–2300 $M^{-1}cm^{-1}$), which is attributable to the IT (intervalence transfer) transition within the Cu_2^{3+} unit.

Conproportionation constants K_{con} of **3** and **4** have been evaluated roughly electrochemically, which are 1×10^{10} and 1×10^{11}, respectively. These values indicate the high stability of the mixed-valence dicopper(II,I) species.

114

Solution X-Band EPR spectra of complexes **1–4** show seven copper hyperfine lines, consistent with interaction of odd electron with both copper centers ($I = 3/2$). In frozen glass medium, all complexes exhibit axial spectra with four-line copper hyperfine imposed on the $g_{||}$ signal, which suggest that the unpaired electron is localized at a single copper site. From these results, all complexes are classified into Class II type mixed-valence dicopper(II,I) complex.

XPS spectra of all complexes show two Cu $2p_{3/2}$ peaks which are assigned to Cu(I) and Cu(II) oxidation state and the satellite structure characteristic of Cu(II). These results argue that all complexes are mixed-valence dicopper(II,I) complex and do not have delocalized ground state on the XPS time scale (ca. 10^{-17} s).

As described above, attempts to prepare the model complexes having the structural prerequisites for the HBCT system, namely the intermolecular H-bond, IT interaction, and the stacked structure of the complexes, were successful. However, the complexes **3** and **4** do not exhibit the PET phenomena. The author would like to discuss the problems that the PET phenomena have not been achieved and the perspective in this research.

From the recent X-ray and IR spectroscopic studies of molecular crystals having intra- and intermolecular H-bond, it has been revealed that the nature of proton in H-bond sensitively depends on the electron charge distribution in surrounding molecules.[4,11] It is considered that the effect of localization of delocalized electron on the amino proton in H-bond would be very small. Therefore, it is hard to expect the mobility of amino proton in N–H···N H-bond due to the very low acidity of amino proton in the complexes **3** and **4** unless the redox reaction at ligand moiety occurs. Taking into account the mobility of proton, it is necessary to introduce the proton donor site which has high acidity. As for the strength of H-bond, the strong H-bond is suited considering the mobility of proton in H-bond unless the redox reaction at ligand moiety occurs. The intermolecular N–H···N H-bonds in the complexes **3** and **4** are very weak because of the steric hindrance of the hydrogen atom in 3-position of the pyridine moiety. Besides intermolecular N–H···N H-bond, the

hydrogen donor sites of each amino group are participated in the N–H···F and N–H···O H-bonds with PF_6 anion and DMF molecule and these H-bonds complicate the IR spectrum. Therefore, it is difficult to assign which absorption band is N–H stretching vibration in N–H···N H-bond when the nature of proton is investigated by IR spectrum.

In order to overcome these difficulties, it is necessary to introduce the hydroxyl group as the proton donor site into the 2-(2'-pyridyl)-4(3H)-pyrimidinone skeleton as shown below. Another method to simplify the H-bond is introduction of counter anion which does not form H-bond with the complex.
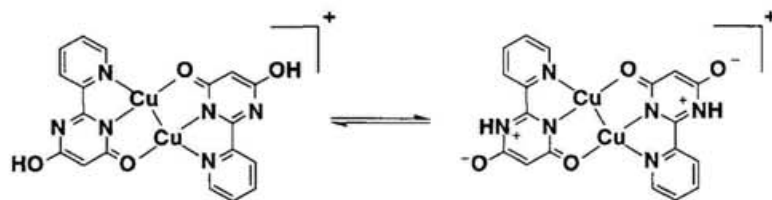
Inabe et al. pointed out from the structural and optical studies that the intermolecular CT interaction affects the difference in the intramolecular proton transfer behavior of the N-salicylideneaniline derivatives.[4] In this point of view, it is considered important to make the intermolecular interaction increase by replacing the coordinated oxygen atom with sulfur atom as shown in Figure 55. In such a case, the electron conduction through the Cu–S conducting path would be expected.
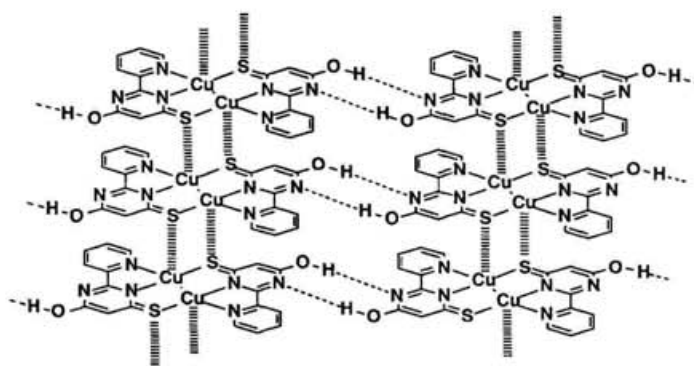

Figure 55. Model for H-bonded mixed-valence dicopper(II,I) complex.

So far the PET phenomena have been discussed from the viewpoint of the proton transfer, but the PET phenomena are not always necessarily the complete proton transfer phenomenon. In general the highly conducting compounds exhibit absorption band which are attributable to intermolecular transition in the IR region, and these absorption bands overlap with the absorption band of D–H stretching vibrations. In such a system, it is anticipated that the D–H stretching vibration couples with the conductive electron and such a compound exhibits characteristic conductive behavior depending upon the coupling between the D–H stretching vibration and the conductive electron.[14] Many of the highly electrical conductors have face-to-face stacks of donor or acceptor molecules, and it is reasonable to identify these stacks as the conducting path. The complexes **3** and **4** form an infinite stacked column structure. However, the high conductivity of these complexes can not be expected because the complexes do not exhibit such CT band in the IR region. A method to obtain highly conductive material is introduction of acceptor molecule such as $TCNQ^{-\cdot}$ anion as counter anion. Inoue et al. reported that a series of the composite compounds, $CuL_n(TCNQ)_2$ (L = 2,2'-bipyridine, 1,10-phenanthroline, di-2-pyridylamine; $n = 1, 2$), composed of copper complexes and TCNQ exhibit high powder conductivity amounting to 0.04–50 Scm^{-1} at 300 K through the conducting path of TCNQ column.[38] Several studies have been devoted to dicopper complex–TCNQ composite compounds having the magnetic exchange interaction of dicopper complex and the electric conductivity of TCNQ[39] To obtain such high conductivity, the TCNQ column must be partial ionic state. Saito et al. reported that the prerequisite to occur the partial electron transfer from donor to acceptor is $-0.02 \leq E_1(D) - E_1(A) \leq 0.34$ V, where $0.24 \leq E_1(D) \leq 0.53$ V and $-0.02 \leq E_1(A) \leq 0.65$ V.[64] The compound which satisfies such prerequisite has a high probability of being molecular metal. In the case that the complex cations of **3** and **4** as acceptor and $TCNQ^{-\cdot}$ anion as donor are used, the values of $E_1(D) - E_1(A)$ are 0.24 and 0.25 V, respectively and therefore the $TCNQ^{-\cdot}$ anion may be partially oxidize according to the following reaction.

$$[Cu_2(II,I)L_2]^+ + TCNQ^{-\cdot} \longrightarrow [Cu_2L_2]^{\delta+}\cdot TCNQ^{\delta-}$$

Because the TCNQ has proton acceptor sites, the construction of the H-bonded dicopper complex–TCNQ composite system is expected (Figure 56).
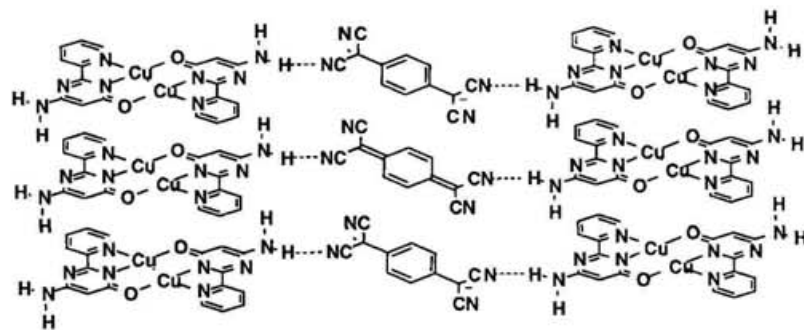
Figure 56. Model for H-bonded composite system composed of dicopper complex and TCNQ.

Potentially, in these compounds, conducting electrons and magnetic electron coexist.

Acknowledgment

References

1   (a) Huryn, D. M.; Okabe, M. *Chem. Rev.* **1992**, *92*, 1745–1768.
     (b) Schwalbe, C. H.; Lowis, D. R.; Richards, W. G. *J. Chem. Soc., Chem. Commun.* **1993**, 1199–1200.

2   (a) Whitesides, G. M.; Simanek, E. E.; Mathias, J. P.; Seto, C. T.; Chin, D. N.; Mammen, M.; Gordan, D. M. *Acc. Chem. Res.* **1995**, *28*, 37–44.
     (b) Braga, D.; Grepioni, F.; Biradha, K.; Pedireddi, V. R.; Desiraju, G. R. *J. Am. Chem. Soc.* **1995**, *117*, 3156–3166.

3   (a) Etter, M. C. *Acc. Chem. Res.* **1990**, *23*, 120–126.
     (b) Aakeröy, C. B.; Seddon, K. R. *Chem. Soc. Rev.* **1993**, *22*, 397–407.
     (c) MacDonald, J. C.; Whitesides, G. M. *Chem. Rew.* **1994**, *94*, 2383–2420.
     (d) Subramanian, S.; Zaworotko, M. J. *Coord. Chem. Rev.* **1994**, *137*, 357–401.

4   (a) Hoshino, N.; Inabe, T.; Mitani, T.; Maruyama, Y. *Bull. Chem. Soc. Jpn.* **1988**, *61*, 4207–4214.
     (b) Inabe, T.; Hoshino, N.; Mitani, T.; Maruyama, Y. *Bull. Chem. Soc. Jpn.* **1989**, *62*, 2245–2251.
     (c) Inabe, T.; Gautier-Luneau, I.; Hoshino, N.; Okaniwa, K.; Okamoto,H.; Mitani, T.; Nagashima, U.; Maruyama,Y. *Bull. Chem. Soc. Jpn.* **1991**, *64*, 801–810.
     (d) Inabe, T.; Hoshino-Miyajima, N.; Luneau, I.; Mitani, T.; Maruyama,Y. *Bull. Chem. Soc. Jpn.* **1994**, *67*, 612–621.
     (e) Inabe, T.; Hoshino-Miyajima, N.; Luneau, I.; Mitani, T.; Maruyama,Y. *Bull. Chem. Soc. Jpn.* **1994**, *67*, 622–632.

5   Reetz, M. T.; Höger, S.; Harms, K. *Angew. Chem. Int. Ed. Engl.* **1994**, *33*, 181–183.

6   (a) Hertel, E. *Ber. Dtsch. Chem. Ges.* **1924**, *57*, 1559–1561.
     (b) Hertel, E. *Liebigs Ann. Chem.* **1926**, *451*, 179–208.
     (c) Hertel, E.; Schneider, K. *Z. Phys. Chem. A* **1930**, *151*, 413–419.
     (d) Hertel, E.; Schneider, K. *Z. Phys. Chem. B* **1931**, *13*, 387–399.
     (e) Hertel, E.; Frank, H. *Z. Phys. Chem. B* **1934**, *27*, 460–466.

7   Kofler, A. *Z. Elektrochem.* **1944**, *50*, 200–207.

8   (a) Saito, G.; Matsunaga, Y. *Bull. Chem. Soc. Jpn.* **1971**, *44*, 3328–3335.

(b) Saito, G.; Matsunaga, Y. *Bull. Chem. Soc. Jpn.* **1972**, *45*, 2214–2215.

(c) Saito, G.; Matsunaga, Y. *Bull. Chem. Soc. Jpn.* **1973**, *46*, 714–718.

(f) Matsunaga, Y. *Bull. Chem. Soc. Jpn.* **1973**, *46*, 998–999.

(d) Saito, G.; Matsunaga, Y. *Bull. Chem. Soc. Jpn.* **1974**, *47*, 1020–1021.

(e) Saito, G.; Matsunaga, Y. *Bull. Chem. Soc. Jpn.* **1974**, *47*, 2873–2874.

9 Bernstein, J.; Regev, H.; Herbstein, F. H. *Acta Crystallogr., Sect. B* **1980**, *36B*, 1170–1175.

10 Tanaka, M.; Matsui, H.; Mizoguchi, J.; Kashino, S. *Bull. Chem. Soc. Jpn.* **1994**, *67*, 1572–1579.

11 (a) Mitani, T.; Saito, G.; Urayama, H. *Phys. Rev. Lett.* **1988**, *60*, 2299–2302.

(b) Mitani, T.; Saito, G. *Synth. Met.* **1988**, *27*, B499–B508.

12 Nakasuji, K.; Sugiura, K.; Kitagawa, T.; Toyoda, J.; Okamoto, H.; Okaniwa, K.; Mitani, T.; Yamamoto, H.; Murata, I.; Kawamoto, A.; Tanaka, J. *J. Am. Chem. Soc.* **1991**, *113*, 1862–1864.

13 (a) Mitani, T. *Mol. Cryst. Liq. Cryst.* **1989**, *171*, 343–355.

(b) Mitani, T. *Oyoubuturi* **1989**, *58*, 1014–1027 (in Japanese).

(c) Nakasuji, K. *Seisantogijyutsu* **1994**, *46*, 54–56 (in japanese).

14 Itoh, T. Ph. D. Thesis, The Graduate University for Advanced Studies, 1995.

(b) Kitagawa, H.; Mitani, T.; Itoh, T.; Toyoda, J.; Nakasuji, K. *Synth. Met.* **1995**, *71*, 1919–1920.

(c) Bandrauk, A. D.; Truong, K. D.; Jandl, S.; Ishii, K. *J. Phys. Chem.* **1985**, *89*, 434–442.

(d) Bandrauk, A. D.; Ishii, K.; Truong, K. D.; Aubin, M.; Hanson, A. W. *J. Phys. Chem.* **1985**, *89*, 1478–1485.

15 Hasegawa, M.; Daiyasu, K.; Yomosa, S. *J. Phy. Soc. Jpn.* **1970**, 28, 1304–1308.

16 Steenken, S. *Chem. Rev.* **1989**, *89*, 503–520.

17 *CRC handbook of nucleobase complexes*, Lusty, J. R., Ed.; CRC Press: Florida, 1990.

18 Metal–pteridines complexes characterized by X-ray analysis are as follows.

(a) Burgmayer, S. J. N.; Stiefel, E. I. *J. Am. Chem. Soc.* **1986**, *108*, 8310–8311.

(b) Burgmayer, S. J. N.; Stiefel, E. I. *Inorg. Chem.* **1988**, *27*, 4059–4065.

(c) Perkinson, J.; Brodie, S.; Yoon, K.; Mosny, K.; Carroll, P. J.; Morgan, T. V.; Burgmayer, S. J. N. *Inorg. Chem.* **1991**, *30*, 719–727.

(d) Kohzuma, T.; Masuda, H.; Yamauchi, O. *J. Am. Chem. Soc.* **1989**, *111*, 3431–3433.

(e) Odani, A.; Masuda, H.; Inukai, K.; Yamauchi, O. *J. Am. Chem. Soc.* **1992**, *114*, 6294–6300.

(f) Nasir, M. S.; Karlin, K. D.; Chen, Q.; Zubieta, J. *J. Am. Chem. Soc.* **1992**, *114*, 2264–2265.

19   Goodgame, M; Schmidt, M. A. *Inorg. Chim. Acta* **1979**, *36*, 151–154.

20   Jayaraman, A. *Rev. Mod. Phys.* **1983**, *55*, 65–108.

21   Piermarini, G. J.; Block, S.; Barnett, J. D.; Forman, R. A. *J. Appl. Phys.* **1975**, *46*, 2774–2780.

22   Perrin, D. D.; Armarego, W. L. F. *Purification of Laboratory Chemicals*; Pergamon Press: New York, 1988.

23   (a) For HLM (lumazine): Albert, A.; Brown, D. J.; Cheeseman, G. *J. Chem. Soc.* **1951**, 474–485.

(b) For HPR (pterin): Mowat, J. H.; Boothe, J. H.; Hutchings, B. L.; Stokstad, E. L. R.; Waller, C. W.; Angier, R. B.; Semb, J.; Cosulich, D. B.; SubbaRow, Y. *J. Am. Chem. Soc.* **1948**, *70*, 14–18.

24   Kubas, G. J. *Inorg. Synth.* **1990**, *28*, 68–70.

25   Melby, L. R.; Harder, R. J.; Hertler, W. R.; Mahler, R. E.; Benson, R. E.; Mochel, W. E. *J. Am. Chem. Soc.* **1962**, *84*, 3374–3387.

26   Cromer, D. T.; Waber, J. T. *International Tables for X-ray Crystallography*; Kynoch Press: Birmingham, England, 1974; Vol. IV, Table 2.2A.

27   Ibers, J. A.; Hamilton, W. C. *Acta Crystallogr.*, **1964**, *17*, 781.

28   Creagh, D. C.; McAuley, W. J. *International Tables for Crystallography*; Wilson, A. J. C., Ed.; Kluwer Academic Publishers, Boston, 1992; Vol. C, Table 4.2.6.8, pp 219–222.

29   Creagh, D. C.; Hubbell, J. H. *In International Tables for Crystallography*; Wilson, A. J. C., Ed.; Kluwer Academic Publishers, Boston, 1992; Vol. C, Table 4.2.4.3, pp 200–206.

30 (a) Beurskens, P. T.; Admiraal, G.; Beurskens, G.; Bosman, W. P.; Garcia-Granda, S.; Gould, R. O.; Smits, J. M. M.; Smykalla, C. PATTY. The DIRDIF program system, Technical Report of the Crystallography Laboratory, University of Nijmegen, The Netherlands, 1992.
(b) Fan, Hai-Fu. SAPI91. Structure Analysis Programs with Intelligent Control, Rigaku Corporation, Tokyo, Japan, 1991.
(c) Sheldrick, G.M. SHELXS86. In *Crystallographic Computing 3*; Sheldrick, G. M.; Kruger, C.; Goddard, R., Eds.; Oxford University Press,1985; pp. 175–189.

31 teXsan. Crystal Structure Analysis Package. Molecular Structure Corp., 1985 and 1992.

32 (a) Beurskens, P.T.; Admiraal, G.; Beurskens, G.; Bosman, W.P.;Garcia-Granda, S.; Gould, R.O.; Smits, J.M.M.; Smykalla, C. DIRDIF92. The DIRDIF program system, Technical Report of the Crystallography Laboratory, University of Nijmegen, The Netherlands, 1992.
(b) Beurskens, P.T.; Admiraal, G.; Beurskens, G.; Bosman, W.P.; de Gelder, R.; Israel, R.; Smits, J. M. M. DIRDIF94. The DIRDIF-94 program system, Technical Report of the Crystallography Laboratory, University of Nijmegen, The Netherlands, 1994.

33 The author used the criterion for the existence of the H-bonding proposed by Hamilton and Ibers.[34] The values for the atomic van der Waals' radii are taken from the tabulation of Bondi.[35]

34 Hamilton, W. C.; Ibers, J. A. *Hydrogen Bonding in Solids*; W. A. Benjamin: New York, 1968.

35 Bondi, A. *J. Phys. Chem.* **1964**, *68*, 441–451.

36 (a) Nakamoto, K.; Margoshes, M.; Rundle, R. E. *J. Am. Chem. Soc.* **1955**, *77*, 6480–6491.
(b) Novak, A. *Struct. Bonding (Berlin)* **1974**, *18*, 177–216.
(c) Lautié, A.; Froment, F.; Novak, A. *Spectrosc. Lett.* **1976**, *9*, 289–299.

37 (a) Hamann, S. D.; Linton, M. *Aust. J. Chem.* **1975**, *28*, 2567–2578.
(b) Hamann, S. D.; Linton, M. *Aust. J. Chem.* **1976**, *29*, 1641–1647.

38 (a) Inoue, M.; Inoue, M. B. *Inorg. Chem.* **1986**, *25*, 37–41.
(b) Inoue, M.; Inoue, M. B.; Seto.T.; Nakamura, D. *Mol. Cryst. Liq. Cryst.* **1982**, *86*, 139–146.

(c) Inoue, M. B.; Inoue, M.; Fernando,Q.; Nebesny, K. W. *J. Phys. Chem.* **1987**, *91*, 527–530.

39 (a) Lacroix, P.; Kahn, O.; Gleizes, A.; Valade, L.; Cassoux, P. *Nouv. J. Chem.* **1984**, *8*, 643–651.

(b) Lacroix, P.; Kahn, O.; Valade, L.; Cassoux, P.; Thompson, L. K. *Synth. Met.* **1990**, *39*, 81–90.

(c) Wang, W.; Jeng. J. *Synth. Met.* **1988**, *27* B205–210.

40 *Mixed Valency Systems: Applications in Chemistry, Physics and Biology*; Prassides, K., Ed.; NATO ASI Series C343; Kluwer: Dordrecht, The Netherlands, 1991.

41 (a) Solomon, E. I. In *Copper Proteins*; Spiro, T. G., Ed.; John Wiley & Sons: New York, 1981; Chapter 2.

(b) Urbach, F. L. In *Metal Ions in Biological Systems*, H., Ed.; Marcel Dekker: New York, 1981; Vol. 13, Chapter 3.

(c) Sykes, A. G. *Adv. Inorg. Chem.* **1991**, *36*, 377–408.

(d) Tsukihara, T.; Aoyama, H.; Yamashita, E.; Tomizaki, T.; Yamaguchi, H.; Shinzawa-Itoh, K.; Nakashima, R.; Yaono, R.; Yoshikawa, S. *Science* **1995**, *269*, 1069–1074.

(e) Iwata, S.; Ostermeier, C.; Ludwig, B.; Michel, H. *Nature* **1995**, *376*, 660–669.

(f) Ramirez, B. E.; Malmström, B. G.; Winkler, J. R.; Gray, H. B. *Proc. Natl. Acad. Sci. U. S. A.* **1995**, *92*, 11949–19951.

42 Hush, N. S. *Prog. Inorg. Chem.* **1967**, *8*, 391–444.

43 Robin, M. B.; Day, P. *Adv. Inorg. Chem. Radiochem.* **1967**, *10*, 247–422.

44 (a) Gagné, R. R.; Koval, C. A.; Smith, T. J. *J. Am. Chem. Soc.* **1977**, *99*, 8367–8368.

(b) Gagné, R. R.; Koval, C. A.; Smith, T. J.; Cimolino, M. C. *J. Am. Chem. Soc.* **1979**, *101*, 4571–4580.

(c) Gagné, R. R.; Henling, L. M.; Kistenmacher, T. J. *Inorg. Chem.* **1980**, *19*, 1226–1231.

(d) Long, R. C.; Hendrickson, D. N. *J. Am. Chem. Soc.* **1983**, *105*, 1513–1521.

(e) Sigwart, C.; Hemmerich, P.; Spence, J. T. *Inorg. Chem.* **1968**, *7*, 2545–2548.

(f) Gatteschi, D.; Mealli,C.; Sacconi, L. *Inorg. Chem.* **1976**, *15*, 2774–2778.

(g) Dancey, K. P.; Tasker, P. A.; Price, R.; Hatfield, W. Brower, D. C. *J. Chem. Soc., Chem. Commun.* **1980**, 1248–1250.

(h) Westmoreland, T. D.; Wilcox, D. E.; Baldwin, M. J.; Mims, W. B.; Solomon, E. I. *J. Am. Chem. Soc.* **1989**, *111*, 6106–6123.

45 (a) Harding, C.; McKee, V.; Nelson, J. *J. Am. Chem. Soc.* **1991**, *113*, 9684–9685.

(b) Barr, M. E.; Smith, P. H.; Antholine, W. E.; Spencer, B. *J. Chem. Soc., Chem. Commun.* **1993**, 1649–1652.

(c) Harding, C.; Nelson, J.; Symons, M. C. R.; Wyatt, J. *J. Chem. Soc., Chem. Commun.* **1994**, 2499–2500.

(d) Farrar, J. A.; McKee, V.; Al-Obaidi, A. H. R.; McGarvey, J. J.; Nelson, J.; Thomson, A. J. *Inorg. Chem.* **1995**, *34*, 1302–1303.

(f) Houser, R. P.; Young, V. G., Jr.; Tolman, W. B. *J. Am. Chem. Soc.* **1996**, *118*, 2101–2102.

46 Dunaj-Jurco, M.; Ondrejovic, G.; Melnik, M.; Garaj, J. *Coord. Chem. Rev.* **1988**, *83*, 1–28.

47 Kahn, O. *Molecular Magnetism*, VCH: New York, 1993.

48 Zerner, M. C. ZINDO Package, Quantum Theory Project, University of Florida, Gainesville, FL.

49 Pople, J. A.; Beveridge, D. L.; Dobosh, P. A. *J. Chem. Phys.* **1967**, *47*, 2026.

50 (a) Medwid, J. B.; Paul, R.; Baker, J. S.; Brockman, J. A.; Du, M. T.; Hallett, W. A.; Hanifin, J. W.; Hardy, R. A., Jr.; Tarrant, M. E.; Torley, L. W.; Wrenn, S. *J. Med. Chem.* **1990**, *33*, 1230–1241.

(b) Kirino, O.; Yoshida, R.; Sumida, S. *Agric. Biol. Chem.* **1977**, *41*, 1093–1094.

51 Brown, D. J.; Cowden, W. B.; Grigg, G. W.; Kavulak, D. *Aust. J. Chem.* **1980**, *33*, 2291–2298.

52 Herbstein, F. H. In *Perspectives in Structural Chemistry*, Dunitz, J. D.; Ibers, J. A. Eds.; John Wiley & Sons: New York, 1972; Vol. 4, pp 166–395.

53 Gagné, R. R.; Kreh, R. P.; Dodge J. A. *J. Am. Chem. Soc.* **1979**, *101*, 6917–6927.

54 Berry, M.; Clegg, W.; Garner, C. D.; Hillier, I. H. *Inorg. Chem.* **1982**, *21*, 1342–1345.

55 Nishida, Y.; Kida, S. *Bull. Chem. Soc. Jpn.* **1985**, *58*, 383–384.

56 Blake, A. J.; Gould, R. O.; Milne, P. E. Y.; Winpenny, R. E. P. *J. Chem. Soc., Chem. Commun.* **1992**, 522–524.

57 Estes, W. E.; Gavel, D. P.; Hatfield, W. E.; Hodgson, D. J. *Inorg. Chem.* **1978**, *17*, 1415–1421.

58 (a) Hay, P. J.; Thibeault, J. C.; Hoffmann, R. *J. Am. Chem. Soc.* **1975**, *97*, 4884–4899.

(b) Kahn, O. *Struct. Bonding (Berlin)* **1987**, *68*, 89–167.

59 Bleaney, B.; Bowers, K. D. *Proc. Roy. Soc. (London) Ser. A* **1952**, *214*, 451.

60 (a) Mandal, S. K; Nag, K. *J. Chem. Soc., DALTON TRANS.* **1983**, 2429–2434.

(b) Mandal, S. K; Adhikary, B.; Nag, K. *J. Chem. Soc., DALTON TRANS.* **1986**, 1175–1180.

61 Goodman, B. A.; Raynor, J. B. *Adv. Inorg. Chem. Radiochem.* **1970**, *13*, 135–362.

62 So, H. *Bull. Korean Chem. Soc.* **1987**, *8*, 111–114.

63 Gagné, R. R.; Allison, J. L.; Koval, C. A.; Mialki, W. S.; Smith, T. J.; Walton, R. A. *J. Am. Chem. Soc.* **1980**, *102*, 1905–1909.

64 Saito, G.; Ferraris, J. P. *Bull. Chem. Soc. Jpn.* **1980**, *53*, 2141–2145.

65 (a) Creutz, C. *Prog. Inorg. Chem.* **1983**, *30*, 1–73.

(b) Creutz, C. Kagaku, **1981**, *36*, 782–790 (in Japanese).

66 Callahan, R. W.; Brown, G. M.; Meyer, T. J. *Inorg. Chem.* **1975**, *14*, 1443–1453.